Institut für Thermische Strömungsmaschinen
Prof. Dr.-Ing. H.-J. Bauer, Ord.

Sensitivity Study and Improvement of a Film Cooling Configuration of a High-Pressure Turbine Blade

Master Thesis

by

Dipl. Juan Ignacio Giménez

Supervisor Rolls-Royce: **Dr. Knut Lehmann**
Supervisor KIT: **Prof. Dr.-Ing. Hans-Jörg Bauer**
Dogan Bicat, M.Sc.

September 2022

Karlsruher Institut für Technologie

Hereby, I declare truthfully that I have observed the current statutes of the Karlsruhe Institute of Technology (KIT) to ensure good scientific practice. This work is written independently, all resources are stated correctly, completely and everything that is taken both modified and unmodified from other sources is indicated.

Berlin, September 5, 2022

I thank the KIT and Prof. Dr.-Ing. H.-J. Bauer for giving me the opportunity to write my thesis in cooperation with Rolls-Royce Deutschland. I want to thank my supervisor Dogan Bicat, for his support and guidance despite the distance. Thanks to Dr.-Ing. Knut Lehmann, who tirelessly motivated me and pushed me to give my best along this journey. For the advice, the knowledge, for fueling my curiosity and all the shared moments that reminded me why I begun this adventure. To him, endless words of gratitude. To Dr. Jens Ortmanns, for giving me the opportunity to join Rolls-Royce Deutschland for this project and his continuous support. To my student colleagues, they understand better than no one what this path is about. For their love, their companion and their invaluable friendship, a gift that I will always carry with me. To all my friends, my KIT colleagues, my lovely girlfriend who stood by my side all this time with the sweetest tenderness. To my "old man" for his words of wisdom, his temperance and for sharing with me this exciting profession since I can remember. Thank you four your boundless love. To my sweet sister Juli, being always close to me and believing in me like no one else. En especial a mi mamá, quien fue mi norte en los más duros momentos. Gracias por tu amor inconmesurable, la constante enseñanza y por sobre todo, el ejemplo de semejante valentía.

Contents

List of Symbols

Symbol	Unit	Description
Latin symbols		
a	m/s	main flow velocity
c	m/s	speed of sound
c_p	J/(kg K)	specific heat capacity at constant pressure
c_v	J/(kg K)	specific heat capacity at constant volume
h	W/(m^2 K)	heat transfer coefficient
$\dot{m}$	kg/s	mass flow rate
p	Pa	pressure
$\dot{q}$	W/m^2	heat flux
u	m/s	mainstream velocity
A	m^2	area
C_D		discharge coefficient
DR		density ratio
I		momentum flux ratio
L	m	length
M		blowing ratio
R	J/(K mol)	universal gas constant
T	K	temperature
Greek symbols		
α	m^2/s	thermal diffusivity
λ	W/(m K)	thermal conductivity
γ		isentropic exponent
ν	m^2/s	kinematic viscosity
ρ	kg/m^3	density
η		efficiency
Ω_i		film cooling vortices
Similarity parameters		
Bi		Biot number
Ma		Mach number
Nu		Nusselt number
Pr		Prandtl number
Re		Reynolds number
Indices		
aw		adiabatic wall
f		film
h		hot gas

k	coolant
p	pressure side
real	real
rec	recovery
s	suction side
th	theoretical
w	wall

Abbreviations

AWT	Adiabatic Wall Temperature
BL	Baseline
CFD	Computational Fluid Dynamics
CHT	Conjugate Heat Transfer
FCE	Film Cooling Effectiveness
HPT	High Pressure Turbine
HTC	Heat Transfer Coefficient
ITS	Institute for Thermal Turbomachinery
KIT	Karlsruhe Institute of Technology
LE	Leading Edge
PS	Pressure Side
SS	Suction Side
TE	Trailing Edge
TET	Turbine Entry Temperature
TP	Triple Pass

List of Figures

List of Tables

1 Motivation

Much effort has been expended in the aerospace industry in order to achieve the highest quality standards required for nowadays technical and environmental necessities. This involves the increase of specific power and overall engine performance, together with the reduction of noise, specific fuel and heat to fuel consumption. Fundamentally, thermal efficiency and power output increase while increasing turbine rotor inlet temperatures. For this purpose, it is necessary to optimize engines with regard to the overall thermodynamic process. Advanced gas turbine engines operate at high temperatures to improve thermal efficiency and power output. As the turbine inlet temperature increases, the heat transferred to the turbine blades also increases.

The level and variation in the temperature within the blade material, which causes thermal stresses, must be restricted to achieve reasonable durability goals. The operating temperatures for aircraft engines are far above the permissible metal temperatures, therefore it is necessary to cool the blades internally and externally. The blades are cooled by extracted air from the compressor of the engine and, since this extraction incurs in a reduction of thermal efficiency, it is necessary to understand and optimize the cooling techniques, operating conditions, and turbine blade geometry. Increasing demands confront the cooling systems of turbine blades. High temperature material development, such as thermal barrier coating (TBC) or highly sophisticated cooling schemes, are a necessary challenge to overcome, in order to ensure high-performance gas turbines for the upcoming years. The suggested designs hereby are to achieve an optimum cooling by a minimum use of cooling air and minimum aerodynamic losses which are an unwanted consequence of film cooling injection.

Cooling techniques in advanced gas turbine engines can be distinguished between internal and external cooling. In convection cooling or internal cooling, the secondary flow extracts the heat flux through the blade walls and transports it away via channels inside the turbine blade. A vast amount of studies for different types of geometry arrangements have been carried out and applied, in order to increase heat flux transfer. These geometries include rib turbulators, pin fins, dimpled surfaces, surfaces with arrays of protrusions, swirl chambers, and rough surfaces. For external cooling, film cooling technology made possible the nowadays achievements in high efficiency gas turbine engines.

The art and science of film cooling concerns the bleeding of internal cooling air through the external walls to form a protective layer between the hot gases and the component external surfaces. The application of effective film-cooling techniques provides a reliable defense for hot gas path surfaces against the high heat fluxes, serving to directly reduce the incident convective heat flux on the surface. Several investigations have been made regarding the major effects of cooling holes arrangements, turbulence, interaction between flows and vorticity production in order to improve film cooling technology.

To address the main challenges of designing an optimal film cooling configuration, it is necessary to understand the behaviour of the main gas flow and the coolant flow. For this purpose, CFD calculations are carried out to visualise and understand the complex physical phenomena under study. However, numerical models should be validated with experimental data as this path leads not only to the understanding of the physical phenomena involved in the experiment, but also provides correct guidance on how the different variables under study can lead to engineering improvement. A test rig at the Institute for Thermal Turbomachinery (ITS) at the Karlsruhe Institute of Technology (KIT) is used to validate the related CFD set-up. In this work, a sensitivity study of different conventional film cooling configurations is introduced. This involves the study and modification of different geometrical variables in specific regions of the blade. Also, the complex vortex structures generated due to the interaction of the main hot gas with the coolant, that enhances heat flux transfer through the blade, is analysed. The most promising configurations in terms of blade temperature reduction, will be considered as possible candidates for blade manufacturing

2 Basics

This chapter provides an introduction to the main theoretical concepts involved in this thesis. Firstly, the transonic nature of high pressure turbine blades (HPT) along with the most relevant flow structures in blade passages are explained. Then, the basics of convective and film cooling concepts are presented. Followed by this, convective and film cooling technology methods with its most relevant geometrical arrangements and physical parameters in modern turbine blade design are introduced. Lastly, the scientific methods for quantifying the film cooling effectiveness and enhancement of heat flux transfer reduction are explained.

2.1 Aerodynamics of HPT Blades

Due to the continuous efforts to improve the efficiency of the engines, the thrust-to-weight ratio, turbine inlet temperature, and total pressure ratio are reaching increasingly higher levels, forcing HPT to operate in a hostile environment, which makes it more challenging to study and design HPT blades and cooling arrangements. In this section, the concepts and basics regarding the transonic flow in high pressure turbines are introduced. Furthermore, the most important flow structures on blade passages and its influence on heat flux transfer are presented.

2.1.1 Transonic HPT Blades

Modern high pressure turbines operate at a transonic flow regime. The reduction in the number of turbine stages, with the aim of minimising the weight, complexity and cooling requirements in aircraft engines, leads to highly aerodynamically loaded turbine blades. These turbine blades have inflow Mach numbers in the subsonic range and outflow Mach numbers in the supersonic or subsonic range. The Mach number can be defined as

$$Ma = \frac{a}{c} \qquad \text{with} \qquad c = \sqrt{\gamma R_i T} \tag{2.1}$$

where a is the main flow velocity, c is the speed of sound at the given conditions of the gas, γ is the specific heat ratio of a gas at constant pressure to heat at constant volume, R_i is specific gas constant and T is the static temperature.

In Figure 2.1a, a cut section of a turbine blade passage indicating the inflow and outflow Mach numbers with total pressure p_t and total temperature T_t at the inlet, is depicted. The sonic condition is reached at the throat, with p^* and Ma^* as the critical pressure and Mach number. The transonic flow regime lies between $0.8 < Ma < 1.3$ and the outflow can be either subsonic or supersonic.

In Figure 2.1b, the complex structures of compression shocks and expansion pockets on the suction side (**SS**) surface are depicted. The shock **A**, originated from the trailing edge (**TE**) wakes of the neighbouring profile, strikes the boundary layer on the SS surface. As a result of the shock wave-boundary layer interaction (**SW-BLI**), a detachment bubble **C** is formed. The

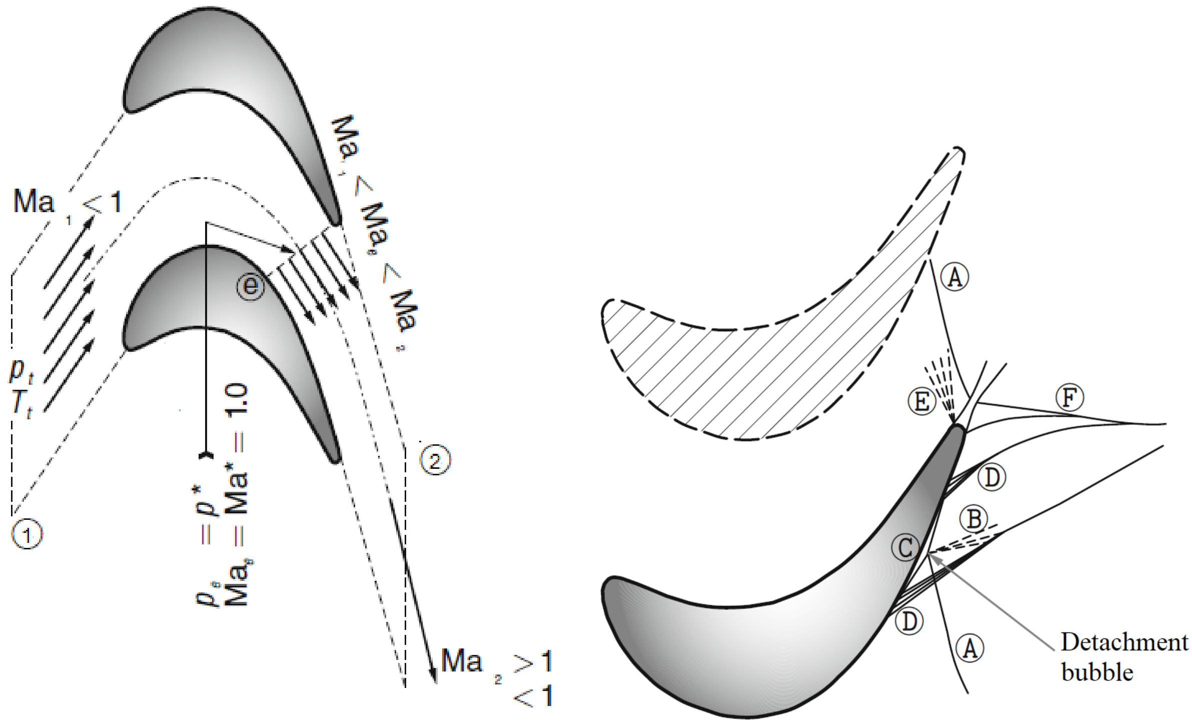

(a) Turbine blade passage with sonic condition at throat.

(b) Typical mechanical flow features.

Figure 2.1: Mechanical flow features in turbine blade passage, adapted from Bräunling (2015).

.

impact is reflected as an expansion fan **B**, leading to a further acceleration of the flow which causes the detached boundary layer to reattach. The detachment bubble generates a concave flow deflection on both beginning and end sides causing compression shocks **D**. In the TE region the flow rounds the pressure side (**PS**) forming expansion fans **E**. Due to a constriction of the profile, both **A** and **F** shock waves occur.

The interaction between shock waves and boundary layer has a great impact on wall pressure, wall shear stress and heat transfer. Generally boundary layer separation will inevitable lead to total pressure loss, so it is necessary to avoid the interaction as much as possible. Laminar boundary layer is more likely to detach compared to turbulent boundary layer (Bräunling (2015)).

This complex flow phenomena causes the Mach number distribution along the blade passage to vary drastically. Proper design of turbine blades should avoid high SW-BLI in order to reduce aerodynamic losses. At the same time, film cooling hole arrangements on the suction side surface should not be placed close to the line of shock wave interaction in order to remain the coolant structure undisturbed as possible over the blade surface and avoid diminishing the film cooling efficiency (Bernardini et al. (2016)).

Various geometric forms, such as blade's bending, blade tip clearance, film cooling holes or changes of upper and lower end walls are critical for turbine design because of the complex structures and mechanical features on blade passages (Zou et al. (2018)).

2.1.2 Secondary Flow Structures in Blade Passages

Due to the complex secondary flow between adjacent blades, “hot spots” can occur along the turbine airfoils, limiting a move to even higher temperatures (Aunapu et al. (2000)).

Several models for secondary flows were used along the decades to describe the vortex structures involved in turbine blade passages. Hawthorne (1955) presented a model based on the appearance of a component of vorticity in the direction of the flow. Klein (1966) introduced the model of the cascade passage vortex. Further studies by Sharma and Butler (1987), Goldstein and Spores (1988) and Wang et al. (1997) provided a more detailed overview of the secondary flow structures. In Figure 2.2 the typical secondary structures in turbine blade passages are depicted, which will be explained in the following subsection.

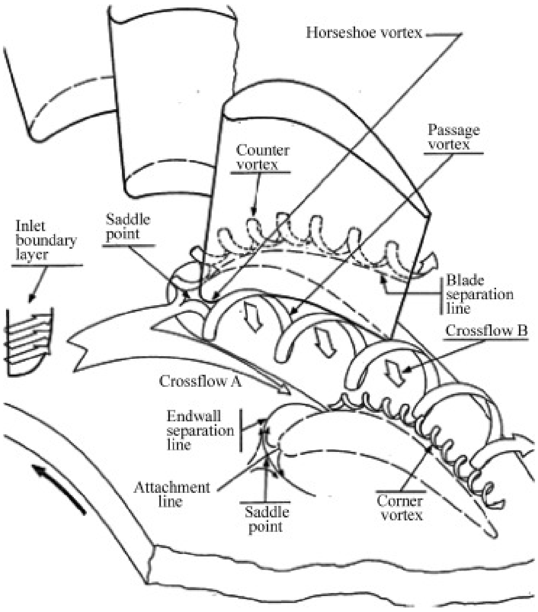

(a) Typical secondary flows in turbine blade passage (Öngören (1981)).

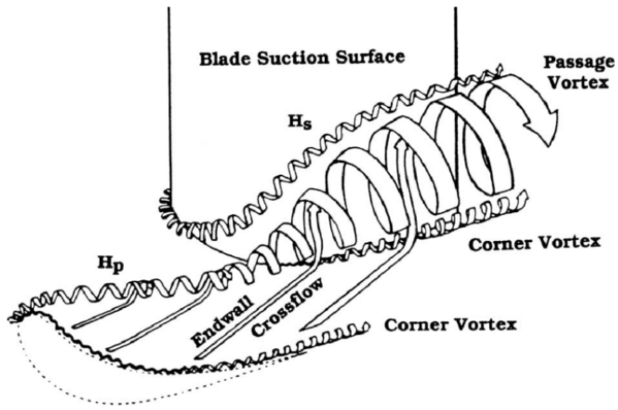

(b) Vortex structures on SS surface (Moon and Koh (2000)).

Figure 2.2: Secondary flow structures in turbine blade passages.

Horseshoe Vortex at the Leading Edge

In the stagnation line of the leading edge, the static pressure is equal to the total pressure. The radial pressure gradient at the leading edge would lead to the generation of a vortex, which is called horseshoe vortex, as depicted in Figure 2.2a. Usually the horseshoe vortex is confined in the region which is thinner than the boundary layer (Zou et al. (2018)). The saddle point can be seen as merge of the adverse flow caused by the horseshoe vortex and the incoming flow near the end wall. Usually, the saddle point is near the place where the incident angle of the flow is zero (Moon and Koh (2000)). A study suggest that the exact location of the saddle point and horseshoe vortex center are dependent on the radius of curvature of the leading edge and the boundary layer thickness of the incoming flow (Huoxing (2012)).

Formation of Passage Vortex

As depicted in Figure 2.2b, the suction side leg horseshoe vortex ($H_{\mathbf{S}}$) wraps around the suction surface of the blade while the pressure side leg horseshoe vortex ($H_{\mathbf{P}}$) migrates across the passage, due to the pressure gradient from pressure to suction side. It combines with the end wall cross flow to form the passage vortex and reaches the suction side of the neighboring airfoil. The pressure side leg horseshoe vortex is larger and stronger than the suction side leg, giving the predominant rotation effect of the passage vortex (Wang et al. (1997)). The passage vortex can merge with the horseshoe vortex of the adjacent blade or they may remain distinct (Goldstein and Spores (1988)). Indifferently, they lift up off the end wall and increase in size. The passage vortex entrains the main flow and end wall boundary layer growing in size, impinges on the suction side wall and rolls up the blade surface as it moves downstream, as shown in Figure 2.2b. The radial pressure gradient in the boundary layer of the suction side surface causes development of the passage vortex towards the middle blade span (Goldstein et al. (1994)).

This vortex structure is of great importance since it disturbs the film cooling air on the surface of the blade, thus resulting in a triangular shaped hot spot (Goldstein et al. (1994)). Secondary flows are also of interest from an aerodynamics standpoint, since one of the highest aerodynamic losses in an engine may occur in the end wall region (Wang et al. (1997)).

2.2 Turbine Blade Heat Transfer and Cooling Concepts

The operating temperatures to increase the overall efficiency of the engine are far above the permissible metal temperature. High metal temperatures lead to higher thermal stresses, thus causing ultimate failure of the component. This requires improved temperature capability materials, the need for internal and external cooling, together with the use of thermal barrier coatings (TBC). In order to deepen the fundamental concepts of major interest within this thesis, the basics of convective (internal) cooling and film cooling are introduced within this section.

2.2.1 Convective Cooling

The typical temperature profiles of a convectively cooled wall with uncooled and cooled outer surfaces are depicted in Figure 2.3, where λ is the thermal conductivity, T_{H} the total temperature of the hot gas (HG) on the outer wall and T_{K} the total temperature on the coolant side.

With these parameters, according to Fourier's equation, the heat flux through the wall $\dot{q_w}$ can be written as

$$\vec{q_w} = -\lambda \frac{\partial T}{\partial y}\bigg|_{w}. \tag{2.2}$$

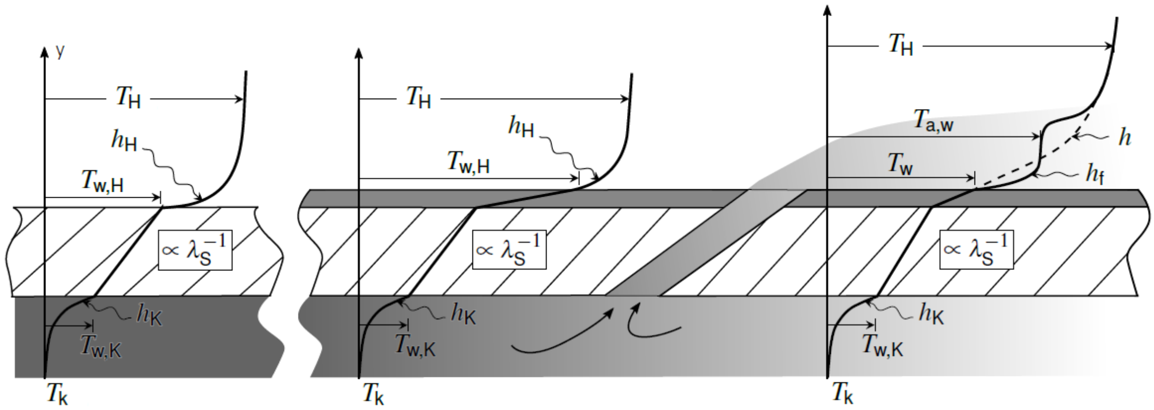

Figure 2.3: Convective, TBC and film cooling heat transfer concepts, adapted from Elfner et al. (2019).

The driving temperatures for the conduction across the metal surface are the wall temperatures $T_{\mathrm{w,H}}$ and $T_{\mathrm{w,K}}$ on both hot gas and coolant side.

According to Newton's law, the convective heat flux can be written as

$$\dot{q_w} = h_{\mathrm{H}}(T_{\mathrm{H}} - T_w), \tag{2.3}$$

where h_{H} is the heat transfer coefficient on the hot gas side. Convective cooling acts as a heat sink for the heat flux through the blade walls. The convective heat flux on the coolant side can be defined as

$$\dot{q_w} = h_{\mathrm{K}}(T_{w,\mathrm{K}} - T_{\mathrm{K}}) \tag{2.4}$$

with h_{K} as the coolant air heat transfer coefficient and $T_{w,\mathrm{K}}$ as the local wall temperature on the coolant side. With these quantities defined, the heat flux through the wall can be written as

$$\dot{q_w} = k(T_{\mathrm{H}} - T_{\mathrm{K}}) \qquad \text{with} \qquad \frac{1}{k} = \frac{1}{h_{\mathrm{H}}} + \frac{1}{h_{\mathrm{K}}} + \frac{s}{\lambda_{\mathrm{w}}} \tag{2.5}$$

with k as the overall heat transfer coefficient, which depends on both hot gas and coolant heat transfer coefficient, wall thermal conductivity and geometry and s as the wall length. The heat transfer coefficient depends on the state of the boundary layer (BL), making it dependent on the Reynolds number, Mach number, the surface roughness, geometry, turbulence intensity and pressure gradients among others. The Reynolds number is the ratio of the inertial forces to the viscous forces within a fluid with u as the main flow velocity, L the characteristic dimension and ν the kinematic viscosity. Other relevant parameters to quantify the heat transfer are the Nusselt Nu, the Prandtl Pr and Biot Bi numbers.

$$Re = \frac{uL}{\nu} \quad (2.6) \qquad Nu = \frac{hl}{\lambda_{\mathrm{f}}} \quad (2.7) \qquad Pr = \frac{\nu}{\alpha} \quad (2.8) \qquad Bi = \frac{hL}{\lambda_{\mathrm{s}}} \quad (2.9)$$

The Prandtl number assesses the relation between momentum transport and thermal transport capacity of a fluid with α as the thermal diffusivity. The Nusselt number is the ratio of convective to conductive heat transfer at a boundary in a fluid with h as the heat transfer coefficient and λ_{f} as the thermal conductivity of the fluid. Due to the high energy mainstream flow, high Nu are likely to be found on the outer surface requiring to enhance the local Nusselt number on the coolant side surface. The Biot number gives an index of the thermal resistances inside a body and outside of it, with λ_{s} as the thermal conductivity of the solid. This ratio determines the speed of convection to conduction heat transfer.

2.2.2 Film Cooling

Film cooling relies on the introduction of a fluid at a temperature below the hot gas, creating a thin film over the surface. This layer protects the blade surface from the high heat fluxes near and downstream of hole outlet. In Figure 2.3 the adiabatic wall temperature $T_{a,w}$ and film heat transfer coefficient h_{f} are depicted. The heat transfer coefficient on the hot gas side wall h_{H} without film cooling will be further referred as h_0. The heat flux without film cooling $\dot{q}_0$ can be written as it follows

$$\dot{q}_0 = h_0(T_{\mathrm{H}} - T_{w,\mathrm{H}}) \tag{2.10}$$

with $T_{w,\mathrm{H}}$ as the local wall temperature on the hot gas side without film cooling. When introducing the coolant with temperature T_{K} to the surface, the mass flux mixes with the mainstream hot gas of temperature T_H. The wall heat flux with coolant injection can be defined as

$$\dot{q}_w = h_f(T_{\mathrm{a,w}} - T_w). \tag{2.11}$$

It is difficult to determine the film temperature and heat transfer coefficient when the coolant mixes with the hot gas. Therefore, it is useful to describe the wall heat flux with film cooling injection as

$$\dot{q}_w = h(T_{\mathrm{H}} - T_w) \tag{2.12}$$

The main goal of the coolant injection is to achieve a lower wall heat flux compared to the uncooled case. For this reason, the ratio between the heat flux with film cooling ($\dot{q}_w$) to without film cooling ($\dot{q}_0$) is introduced as

$$\frac{\dot{q}_w}{\dot{q}_0} = \frac{h(T_{\mathrm{H}} - T_w)}{h_0(T_{\mathrm{H}} - T_{w,\mathrm{H}})} \tag{2.13}$$

In order to obtain any final benefit from introducing a coolant over the heated surface, the heat load ratio should be lower than 1 (Han et al. (2013)). Film cooling is a complex concept which depends primarily on the coolant to mainstream pressure ratio (p_{K}/p_t) (also known as film pressure), temperature ratio $(T_{\mathrm{K}}/T_{\mathrm{H}})$ the film cooling hole location, type of configuration and distribution along the surface. The most important parameters for quantifying the interaction between the film cooling jets and the mainstream gas are the blowing ratio M, the momentum flux ratio I, the density ratio DR and the discharge coefficient C_{D}

$$M = \frac{\rho_{\mathrm{K}} u_{\mathrm{K}}}{\rho_{\mathrm{H}} u_{\mathrm{H}}}, \qquad I = \frac{\rho_{\mathrm{K}} u_{\mathrm{K}}^2}{\rho_{\mathrm{H}} u_{\mathrm{H}}^2}, \qquad DR = \frac{\rho_{\mathrm{K}}}{\rho_{\mathrm{H}}} \qquad \text{and} \qquad C_D = \frac{\dot{m}_{\mathrm{real}}}{\dot{m}_{\mathrm{ideal}}}. \tag{2.14}$$

With ρ_{H} and ρ_{K} the hot gas and coolant density, u_{H} and u_{K} the hot gas and coolant bulk velocity, $\dot{m}_{\mathrm{real}}$ and $\dot{m}_{\mathrm{ideal}}$ the real and the ideal mass flow rates through a film cooling hole.

The ideal mass flow rate through the film cooling holes is determined analogous to a pipe flow. Hence, it can be written as

$$\dot{m}_{\mathrm{ideal}} = \frac{A p_{t,\mathrm{in}}}{\sqrt{R T_{t,\mathrm{in}}}} \sqrt{\frac{2\gamma}{\gamma - 1}\left(\left(\frac{p_{\mathrm{out}}}{p_{t,\mathrm{in}}}\right)^{\frac{2}{\gamma}} - \left(\frac{p_{\mathrm{out}}}{p_{t,\mathrm{in}}}\right)^{\frac{\gamma+1}{\gamma}}\right)} \tag{2.15}$$

with A as the cross sectional area of the hole, $p_{t,\mathrm{in}}$ the total pressure at the inlet of the hole, $T_{t,\mathrm{in}}$ the total temperature at hole inlet and p_{out} is the hole outlet static pressure.

The blowing ratio M is the jet mass flow to hot gas mass flux ratio. The film cooling performance and jet detachment have a direct relation with the blowing ratio (Han et al. (2013)). Momentum flux ratio I is the parameter used to quantify the deflection of the jets along concave and convex surfaces. The discharge coefficient C_{D} relates how much mass flow is being introduced upon the ideal mass flow. Hence, it is suitable for analysing the losses generated by coolant injection.

2.3 Internal Cooling Methods

In Figure 2.4 modern internal turbine blade cooling concepts are shown. This includes jet impingement cooling, rib turbulators and pin-fin with holes and dimples as internal cooling concepts. Besides jet impingement, three dimensional structures protrude from the surface promoting wake shedding that increases turbulence, hence heat transfer augmentation. Different secondary flow structures originate from these internal arrangements, thus accounting for different pressure drops and heat transfer enhancement (Han (2004)).

Pin-Fin and Dimple Arrays

A schematic overview of different pin-fin arrays is depicted in Figure 2.4b. The most relevant parameters for pin-fin arrays are shape, height, streamwise and spanwise spacing and Reynolds number. They can be commonly found in combination with holes and dimples.

For this type of internal configuration, a horseshoe vortex originates upstream of the base of the pin and wraps around the pin, causing more flow disturbances and enhancing heat transfer. However, such complicated flow structures account for high pressure losses in the blade passage. Different secondary flow structures originate from both pin-fin and holes and dimples,

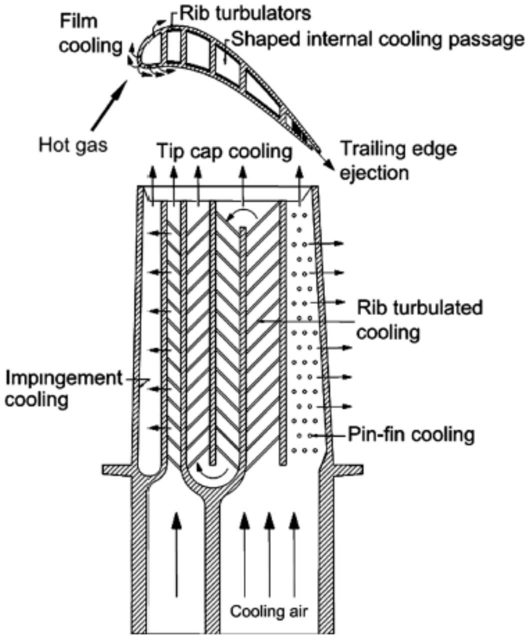

(a) Modern turbine blade cooling concepts.

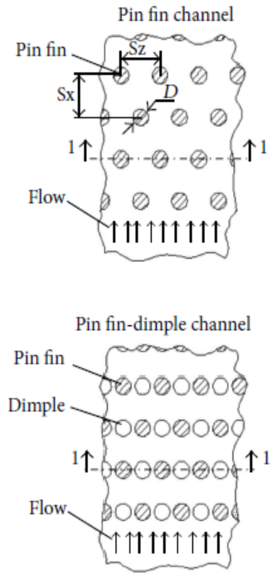

(b) Pin-fin and pin-fin dimple channel configurations.

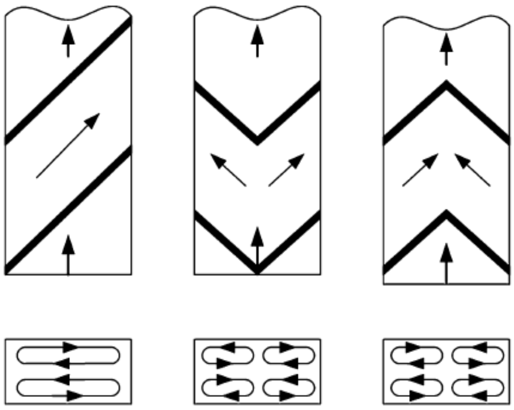

(c) Conceptual secondary flow vortices induced by inclined ribs.

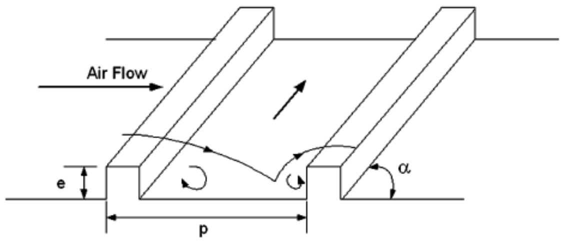

(d) Schematic of flow separation from ribs and secondary flow between angle ribs.

Figure 2.4: Schematic internal cooling methods from Han (2004).

thus accounting for different pressure drops and heat transfer enhancement (Krishnaswamy and Salyan (1994)).

Rib Turbulators

In advanced gas turbine blades, rib turbulators are often cast on two opposite walls of internal coolant passages to augment heat transfer. These ribs protrude into the flow, acting to trip the flow, mix it and also generate vortices and three dimensional velocity gradients, as shown in Figure 2.4d.

Rib turbulators are frequently designed as rectangular cross sectional bars mounted along the surface, in an angle with the bulk flow direction (Figure 2.4c). The heat transfer coefficients can be further enhanced by casting the ribs with an angle to the coolant flow, which causes a rib-induced secondary flow moving in the rib angle direction (Siw (2007)). By varying each of these geometric parameters, it is possible to optimize the cooling scheme in such a way to avoid hot and cold spots along the blade surface. The internal coolant passages are mostly modeled as short, square or rectangular channels with various aspect ratios. The heat transfer augmentation in rectangular coolant passages with rib turbulators primarily depends upon the rib's geometry, such as rib size, shape, distribution, flow attack-angle, and the flow Reynolds number (Han (2004)). Rib turbulators disturb only the near-wall flow for heat transfer enhancement. Therefore, the pressure drop penalty caused by rib turbulators is affordable for the blade internal cooling designs.

Impingement Cooling

Jet impingement cooling is known by its potential to increase local heat transfer coefficient but, the arrangement of this flow structure weakens the structural integrity of the blade. Therefore, impingement cooling is only used in in locations with high thermal loads. The region for this kind of arrangement is the leading edge region (Han et al. (2013)). Basically, holes are drilled with an angle in the inner channels creating the passages for the cold jets that hit the internal surface of the blade, thus extracting the heat load from the mainstream flow over the outer surface (Figure 2.4a).

Both pin-fin dimples and jet impingement internal cooling arrays are out of the scope of this thesis.

2.4 Film Cooling Technology

Film cooling technology is one of the major technologies allowing gas turbines to operate at higher inlet temperatures. It consist in the introduction of a secondary fluid (coolant or injected fluid) at one or more discrete locations along a surface exposed to a high temperature environment to protect that surface not only in the immediate region of injection but also in the downstream region (Goldstein et al. (1971).

The application of effective film cooling techniques provides a good protection for hot gas path surfaces against the high wall heat fluxes, serving to directly reduce the incident convective heat flux on the surface (Bunker (2005)). For this reason, considerable amount of research has been done over the past decades. These studies involve the major effects of interactions with the mainstream flow, turbulence and vorticity production, inlet hole flow conditions, outlet hole shaping, orientation, spacing, hole to length diameter ratio, effects of mainstream turbulence intensity, external surface curvature, among others (Han et al. (2013)). Many of the before mentioned parameters will be studied along this thesis

2.4.1 Effect of Film Hole Geometry

In this subsection, some of the geometrical film cooling parameters analysed along this thesis, are explained.

Compound Angle

The compound angle injection can be identified by two angles as shown in Figure 2.5. The inclination angle α is defined as the angle between the injection vector and its projection on x–z plane, whereas the streamwise angle β is defined as the angle between the streamwise direction and the projection of the injection vector on x–z plane (Ahn et al. (2003)).

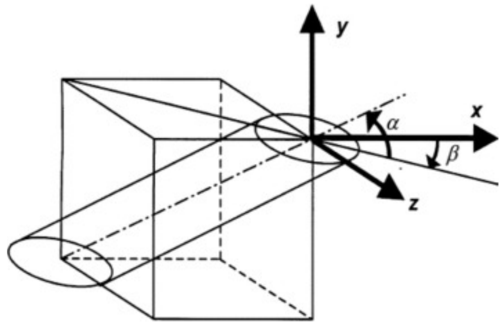

Figure 2.5: Description of compound angle (Bashir et al. (2017)).

.

Baldauf et al. (2001) investigated the effect of inclination angle for cylindrical holes. Lower angles resulted in better film coverage. Martinez-Bota and Yuen (2005) also investigated the effect of inclination angle for three different values for a simple cylindrical hole using liquid crystal technique. A larger α assisted in coolant jet penetration into the mainstream that resulted in jet lift-off, even for lower blowing ratios. Reducing the inclination angle provided greater effectiveness and $\alpha = 30°$ was concluded as the most optimum of the three analysed configurations.

Ekkad et al. (1997) focused their study on the effect of compound angles for cylindrical holes. Transient liquid crystal technique was employed with two density ratios. It was reported that compound angles provided a better effectiveness compared to simple angled holes. Ligrani and Lee (1996) also used compound angle geometry with $\alpha = 24°$, $\beta = 24°$. Higher effectiveness was explained by a reduction in axial momentum and improvement in lateral momentum due to angle β. This resulted in a better film coverage and delayed jet lift-off.

To explain jet behavior, Aga (2011) used particle image velocimetry for compound angle holes with $\alpha = 25°$ for two different β angles at different blowing ratios (1.0 and 2.0) and density ratios (1.0 and 1.5). Compound angles have vertical vorticity and lateral vorticity. For lower β and higher higher blowing ratios, the vertical component of vorticity is dominant which causes lift-off. For larger β, the asymmetric vorticity allows for better lateral coverage, which was found aligned more towards the compound angle for higher M. A graphic description of improved lateral coverage for angle shaped holes is depicted in the first row of Figure 2.6,

Outlet Hole Shape

Among the variety of film cooling hole arrays, four kinds of hole configurations are depicted in Figure 2.6. These are: cylindrical holes, laterally-diffused (fan-shape) holes, forward-diffused (laid-back) holes, and laterally- and forward-diffused (laid-back fan-shape) holes. The fan-shape angle and the laid-back angle are referred as γ and δ respectively.

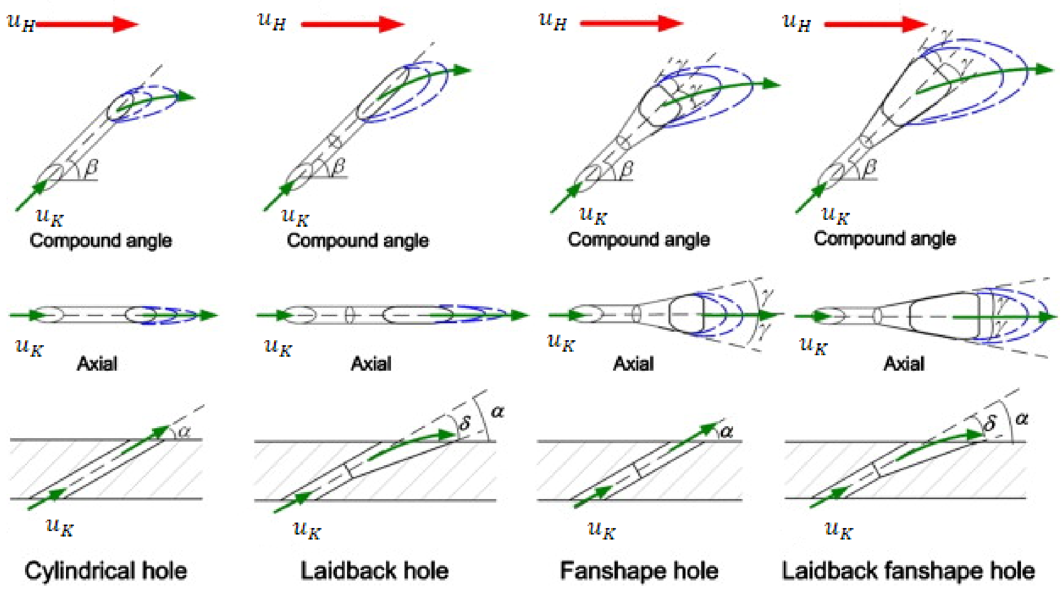

Figure 2.6: Combination of angle shaped holes, adapted from Gao et al. (1997).

.

Shaped holes consist of round throat sections with an expanded outlet zone on the hot gas surface that is uniform and symmetrical. Most shaped holes used in practice have outlet shape as a diffuser with divergence angles between 10 and 15 degrees on each lateral side as well as on the side into the surface (laid-back fan-shape hole) (Bunker (2005)).

The aim for shaped film holes is to enlarge the exit area in the surface plane of the injection jet by a factor of 2–3 compared to that of the cylindrical hole. This can correspond to an equivalent diffusion of the jet itself, subject to the flow conditions. The jet diffusion could lead to an improved cooling effectiveness and turbine efficiency, by lowering blowing ratios and aerodynamic mixing losses, and increasing the lateral coolant coverage (Bunker (2005)).

Hole Spacing

Increasing the spanwise hole separation for a single row of holes can cause a reduction in film cooling effectiveness. This is because the amount of coolant available per unit area is decreased. However, it is argued that for high enough pitch wise separation to hole diameter ratio, each jet behaves independently. For lower ratios, jet coalescence changes the behavior of film and how it interacts with the mainstream, causing a non-linear reduction in effectiveness due to variation in spacing (Bashir et al. (2017)).

2.4.2 Secondary Flow structures in Film Cooling Jets

Complex vortex structures originate from the interaction of film cooling jets and the mainstream hot gas. A schematic overview of the main flow structures is depicted in Figure 2.7. The emerging jet with bulk velocity u_K gets stricken and deflected towards the surface by the mainstream flow with bulk velocity u_H, originating the horseshoe vortex Ω_3. The resulting vortex wraps around the jet structure, creating a typical shape of a two leg horseshoe vortex. As a result, the pressure gradient is positive in front of the jet and negative in the direction of the wall, which causes the separation of the boundary layer. In contrast to the horseshoe vortex on a circular cylinder, the curling up of the boundary layer on a jet emerging from the wall occurs in a weaker form (Dückershoff et al. (2017)). The rolling up effect is countered by an extra frictional force in the shear layer between the emerging jet and the boundary layer's congestion line at the jet. The resulting structure forms the horseshoe vortex Ω_1, which rotates in opposite direction of Ω_3. This vortex supports the hot mainstream gas to penetrate below the film cooling jet structure enhancing heat transfer near coolant injection and hence, increasing heat flux towards the blade metal. The kidney vortex Ω_2 arises due to the deflection of the flow which causes a suction side and pressure side at both bottom and top of the jet. The momentum forces in the free shear layer of the jet are not sufficient to allow the flow to follow the jet trajectory. The pressure forces cause a downward movement of the flow at the edge of the jet and, for continuity reasons, an upward movement in the jet core. Two vortices are created, which are symmetrical and counter-rotating in the case of discharge in the direction of the adjacent main flow. The free shear layer of the emerging jet is additionally subjected to frictional forces due to the interaction with the hot gas, which support the deflection of the jet and the formation of the kidney vortex. This is known to be the most predominant secondary flow structure on film cooling jets and can also be originated due to upstream flow separations known as jetting effect.

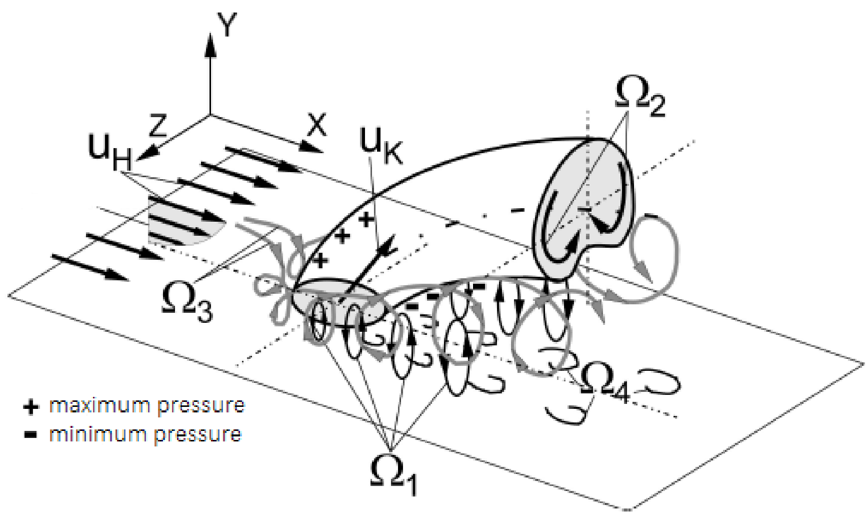

Figure 2.7: Film cooling jet flow structures, adapted from Dückershoff et al. (2017).

Jetting Effect

The coolant air is driven by the pressure difference over the hole. Because of the compound angle, a separation bubble is formed on the downstream side of the hole inlet, due to the large deflection of the coolant, when entering the hole. Position and size of such flow separation depend on the inflow conditions and can appear on either side of the hole (Baldauf and Scheurlen (1996)).

With increasing coolant velocity, an optimum is reached, where no separation occurs on either side of the hole. Further increasing the cooling air velocity leads to a separation on the upstream wall in the hole. It decreases the effective flow area, leading to the jetting effect, with an asymmetric cross sectional velocity profile and a reduced discharge coefficient. Due to the deflection of the flow along the convex surface, centrifugal forces are generated in the fluid reaching its maximum on top of the bubble. Thus originating two counter rotating vortices named as kidney vortices, that dominate the coolant flow.

2.5 Adiabatic Wall Temperature & HTC Calculations

Adiabatic wall temperature and heat transfer coefficient calculations are required in order to comprehend and improve modern cooling configurations. Two methods have been used to determine the heat load reduction to surfaces with film cooling: superposition approach and adiabatic wall effectiveness approach. Both methods are conceptually equivalent.

For the adiabatic wall effectiveness approach, used for the purposes of this work, the adiabatic wall effectiveness and the heat transfer coefficients are determined from separate experiments.

Goldstein and Eriksen (1974) conducted heat transfer coefficient and adiabatic wall temperature calculations on thin heated airfoils measuring the temperature with thermocouples placed underneath the foil surface. Electrical power is fed to the thin airfoils acting as a heating source. The heated surface is exposed to the flow and when achieving the steady state, the temperatures downgrade and the local heat transfer coefficients are calculated as

$$HTC = \frac{\dot{q}_w}{T_w - T_{aw}} \tag{2.16}$$

The local heat flux through the wall is a balance between the generated heat flux and the local loss heat flux. T_w is the local steady-state wall temperature and T_{aw} is the adiabatic wall temperature measured when the airflow is on but no current is fed to the airfoils. Leiss (1995) and Han et. al (1993) also used this technique for scientific purposes for HTC measurements.

The heat transfer coefficient can be also written as

$$HTC = \frac{\dot{q}_{gen} - \dot{q}_{loss}}{T_w - T_{aw}} \tag{2.17}$$

with $\dot{q}_{gen}$ as the surface generated heat flux from current measurement and $\dot{q}_{loss}$ as the local heat loss as a function of the local wall temperature.

In general terms, the HTC can be defined as

$$HTC = \frac{\Delta \dot{q}}{\Delta T}. \tag{2.18}$$

The same surface can be used for film effectiveness measurements in film cooling configurations. The heat transfer coefficients are determined for mainstream and coolant air at the same temperature whilst the test surface is heated. The adiabatic wall temperature is equal to the wall temperature when both the mainstream and coolant flows are on and the surface is unheated. The film effectiveness measurements are made with the similar test section, with the mainstream at ambient temperature, coolant heated, and the surface unheated. The local wall temperature is now the adiabatic wall temperature, as the surface is unheated and well insulated.

The film cooling efficiency can be written as

$$FCE = \frac{T_H - T_{aw}}{T_H - T_K} \tag{2.19}$$

with T_{aw} as the adiabatic wall temperature with film cooling. The film cooling efficiency increases with lower values of adiabatic wall temperatures. Hence, reducing the heat load ratio. As depicted in the previous subsection in equation 2.13, it is important to notice that the wall heat flux ratio depends on the heat transfer coefficient cooled to uncooled ratio. It is known that introducing a secondary flow over the blade surfaces generates a distortion on the heat transfer coefficient distribution (Goldstein et al. (1971)). This ratio should also decrease when injecting coolant and at the same time enhance the FCE, making this a challenging step in correct film cooling design.

2.6 Sensitivity Analysis

Sensitivity analysis can be defined as the study of how the uncertainty in the output of a mathematical model or system can be divided and allocated to different sources of uncertainty in its inputs. There is a critical balance between the way an analyst explores the input assumptions and the extent of the resulting inference. Alizadeh et al. (2014) conducted a sensitivity analysis for the simulation of a cooled turbine blade, to predict accurately blade temperature distribution. A conjugate heat transfer procedure, which uses a one-dimensional coolant network code for the cooling passage simulation, was used. The coupled technique has been used for the internal side (1-D simulation) due to its low time consuming, while for the external side the conjugate procedure was utilized. This methodology was validated using experimental data.

Computational resources are a big constrain for sensitivity analyses, since complex geometries can take several hours of time to converge and a large number of try outs are necessary to sample the data and find the trend for the variables under study. Another issue can be the correlation between inputs. As carried out through this thesis, it is assumed the independence between the model inputs but, sometimes, this is not the case and a strong correlation can lie between the different inputs. The method used in this work is the "one-factor-at-the time" (OFAT). It involves the modification of one input variable, keeping the rest at their baseline (nominal values). Afterwards, this variable is returned to its nominal value and then proceeding with the same methodology for each of the other inputs.

3 Test Rig and Numerical Models

In this chapter, the configuration of the experimental test rig together with its subsequent baseline numerical model and boundary conditions is presented. This test rig is used for validation of CFD model. Furthermore, numerical models for FCE and HTC calculations are introduced. Finally, mesh settings and generation process are described.

3.1 Test Rig Set Up

A cut section of the KIT test rig constructed by Elfner et al. (2019) is depicted in Figure 3.1. The main hot gas enters through a pipe and then is conducted through a two passage blade cascade. Since the test rig is stationary, the inlet is equipped with a flow conditioner that modifies the flow angle and the radial mass flow distribution. This grid sets the relative reference frame for the rotor blade under study. The blade passage consists of one centered shrouded blade and suction side and pressure side shaped walls as the pitch wise neighbouring blades surfaces. In order to conduct thermography measurements, the rig is equipped with three optical window accesses o_{w1}, o_{w2} and o_{w3} to capture blade images. Suction side and pressure side tailboards were designed to adjust for correct pressure distribution along the passage.

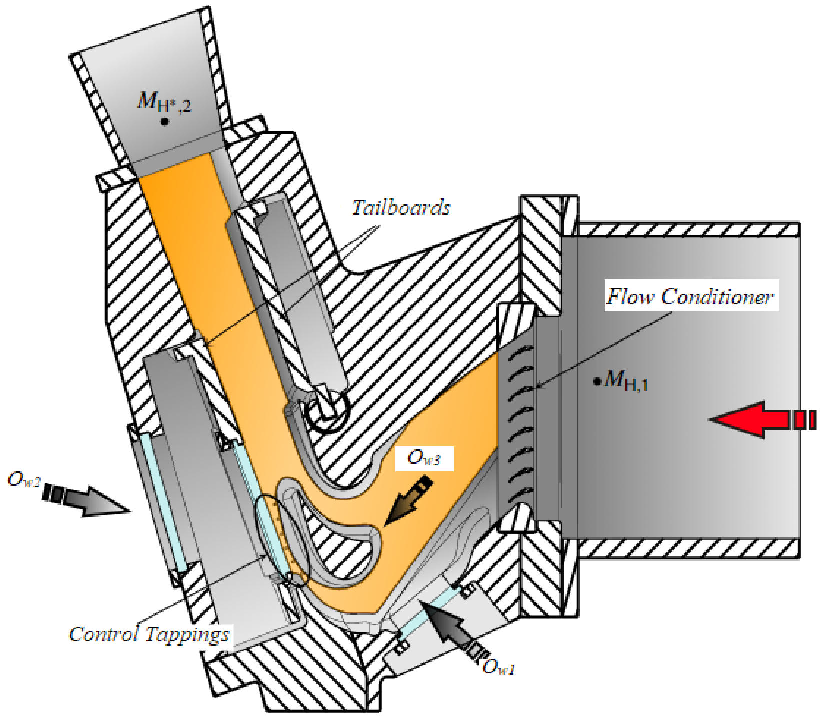

Figure 3.1: Cut section of test rig, modified from Elfner et al. (2019).

3.2 Baseline Cooling Design

In Figure 3.2, an overview of the baseline cooling configuration model is depicted. All holes of each row are enumerated going from hub to tip, starting from "1". A schematic representation of the flow direction through the core channels is depicted in Figure 3.2a. The internal passages are named after LE channel, first triple-passage (TP1), second triple-passage (TP2) and third triple-passage (TP3). Both LE and triple-passage channels are fed by the same root inlet. In the LE channel and in the TP1, the flow goes from hub to tip, whereas in the TP2 it flows from tip to hub. Finally, in the TP3 the flow goes from hub to tip, exiting the TE tip outlet. In Figure 3.2c, a blade cut section with film cooling holes and channels configuration is represented. In the LE channel, three film cooling rows are drilled. Thus, these rows are referred as the LE SS Rear row, LE SS Front row and LE PS row. LE SS Front and LE PS rows contain angled cylindrical holes whereas on the LE SS Rear row, simple angled fan-shape holes are set. On the mid chord of the pressure side surface, axial fanshaped holes are drilled into the TP2 and cylindrical TE holes are connected to the TP3.

In Figure 3.2b, the experimental cooling blade concept with all its features is given. From the test rig, experimental data for CFD validation is extracted. Mass flow rate measurements are conducted downstream of the u-bend connection between LE channel and TP1 and at the TE outlet (M_{C21} and M_{C22} in Figure 3.2b). Pressure measurements are conducted upstream of the u-bend merge of the LE channel and TP1 and upstream of the outlet of TP3, exactly at all core tip outlets as shown in Figure 3.2a. The experimental blade contains steps at all three outlets where pressure measurements are conducted. Due to strong flow separations leading to instabilities in the CFD model, these outlet steps are not considered in the numerical model. This fully concept depicted in Figure 3.2, will be further referred as the baseline model (BL). All the geometrical modifications presented throughout this work are based on this model.

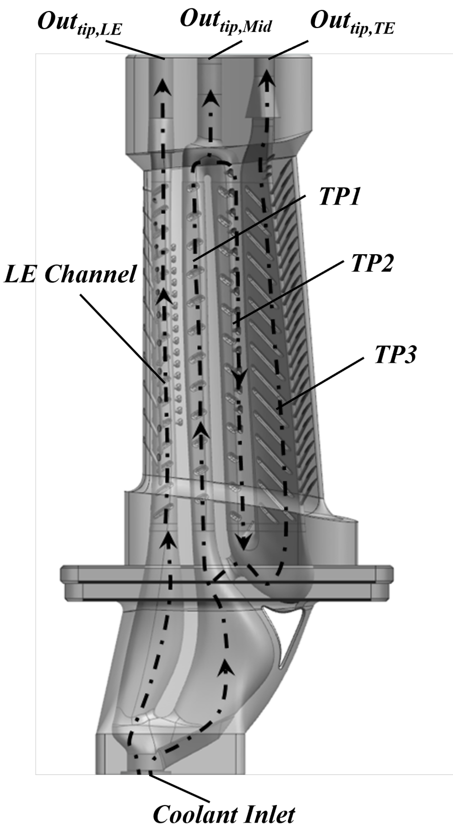

(a) CAD PS view of cooled blade.

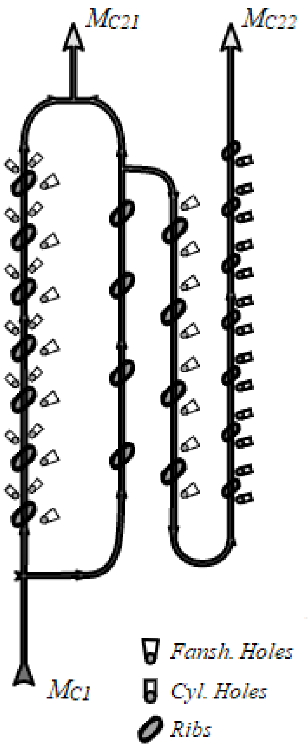

(b) Conventional cooling blade concept.

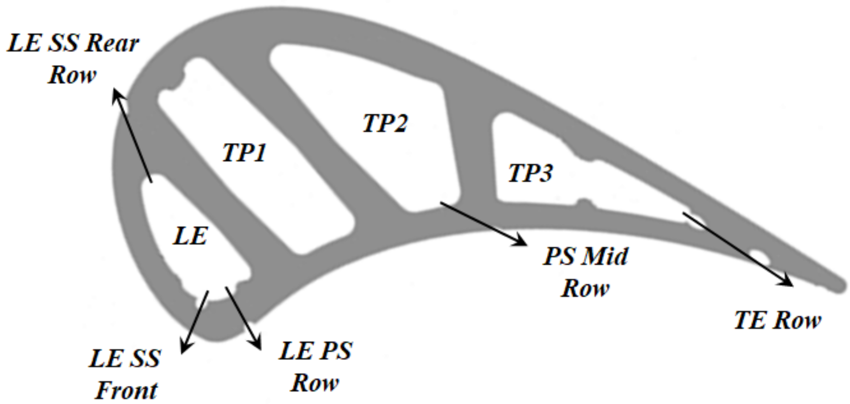

(c) CAD blade cut section at 50% spanwise.

Figure 3.2: Overview of conventional cooling configuration.

3.3 Numerical Models

The numerical models conducted in this thesis are based on previous studies done by Stichling (2018). Due to mesh size resolution, this thesis will not take into account the inlet flow grid for any given simulation model. Also, due to strong flow separations leading to instabilities in former works, the outlet diffuser and the geometry steps at the outlet tips of the core are not considered. A k-ω-SST Turbulence Model was conducted throughout this work.

In this thesis, three different numerical models were used to accurately predict blade temperature, film cooling efficiency and heat transfer coefficient distributions. A conjugate heat-transfer model (CHT) is used to predict metal temperature, coupling both conduction and convective heat transfer, by the use of interfaces between fluid and solid domains. Film cooling effectiveness and heat transfer coefficients, are calculated without the presence of any solid, hence they replicate the heat transfer interaction between both fluids. All numerical models presented in this work, were conducted using Ansys CFX 19.2 and Ansys CFD-Post for the post-processing stage. Only when compared to the experimental data, both results were post-processed in a modified in-house version of ParaView. Hereafter, the details of each model are presented.

3.3.1 CHT Model

In Figure 3.3 the CHT model of the experimental set up of the cascade with conventional blade cooling configuration is depicted. It includes the section downstream of the flow conditioner, with a total pressure profile $p_{t,\mathrm{H1}}$ with velocity directions exported from a fully featured model at the inlet (H1). The mainstream flow is driven by the pressure difference between the total pressure at the inlet and the static pressure at the outlet p_{H2} of the cascade. The static pressure at the outlet H_2 is averaged using radial equilibrium with reference position at minimum radius. The model includes the windows o_{w1} and o_{w2}. Window o_{w3} and the cavities behind the SS and PS tailboard were not modelled since their influence was tested negligible (Stichling (2018)). At the root inlet a fixed mass flow rate $\dot{m}_{\mathrm{Root}}$ with static temperature T_{Root} and medium turbulent intensity (5%) was defined. The air flows from the core root feeding the film cooling rows and exiting the dust holes on each outlet at the tip of the blade $Out_{\mathrm{tip,LE}}$, $Out_{\mathrm{tip,Mid}}$ and $Out_{\mathrm{tip,TE}}$ respectively. On each tip outlet holes, a constant mas flow rate $\dot{m}_{\mathrm{out,LE}}$, $\dot{m}_{\mathrm{out,Mid}}$ and $\dot{m}_{out,TE}$ were also applied and the cascade walls were defined to a constant temperature T_{W}. In order to estimate correctly the wall temperatures of the blade, a CHT analysis shall be conducted to couple the fluid and solid heat transfer through the blade metal. Thus, the model constitutes both fluid and solid domains. For this, the interfaces between all fluids and solids are defined with a no slip and smooth wall boundary condition with conservative interface heat flux and 1:1 mesh connectivity. These interfaces are depicted with green arrows in Figure 3.3. All the solid surfaces not interacting with any type of fluid are either insulated or set to ambient temperature together with a heat transfer coefficient. Radiation is not considered in this work,

The set of boundary conditions applied to the baseline case is depicted in Table 3.1. In former works, the wall temperatures were estimated using inlet and outlet total temperatures by calculating the overall heat loss. However, this involves many assumptions that led to unreliable

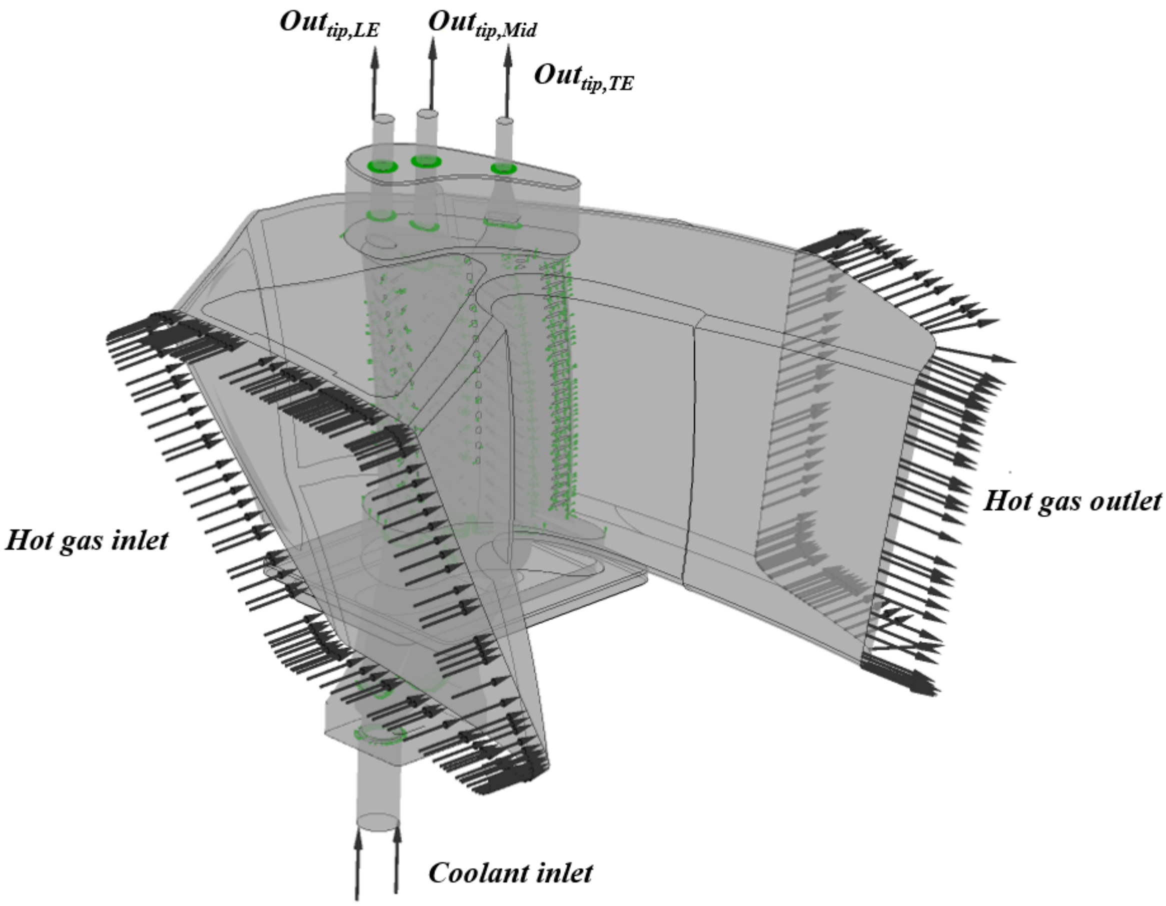

Figure 3.3: Isometric view of the baseline CHT model.

results. This boundary condition will not be further analysed and remains as given. As depicted in Figure 3.2b, the exit mass flow at $Out_{\mathrm{tip,LE}}$ and $Out_{\mathrm{tip,Mid}}$ is determined by the common exit pipe M_{C21} while pressure measurements are being conducted upstream where both exits are still separated. The CHT model finishes where this measurements were taken. In former works, an equal mass flow split between both LE and Mid tip outlets was defined. In order to achieve a realistic split between the channels, a study of the boundary conditions compared to the experimental data was conducted. As already mentioned, in the experimental test rig, the outlet tips were designed with steps downstream of the pressure measurement position. This steps led to instabilities due to possible flow re circulations generating back flow close to the boundary outlet, which is defined with a constant mass flow rate normal to the surface in the opposite direction. At the same time, in the experimental rig the connection between both LE and Mid exits is done by the use of large flanges, making it impossible to model in the CAD geometry. This will be further discussed in the subsequent chapters.

3.3.2 Adiabatic Wall Model

As introduced in Section 2.5, adiabatic wall temperature calculations help understand and predict proper interaction of the film cooling jets and the main hot gas stream over the blade sur-

Table 3.1: Set of boundary conditions for CHT baseline model

Boundary	Parameter	Variable	Value
Cascade Inlet	Total Pressure	$p_{\mathrm{t,H1}}$	125 600 Pa
	Total Temperature	$T_{\mathrm{t,H1}}$	570 K
Cascade Outlet	Average Static Pressure	p_{H2}	89 500 Pa
Root Inlet	Mass Flow Rate	$\dot{m}_{Root}$	2.00x10^{-2}kg/s
	Static Temperature	T_{Root}	306 K
LE Tip Outlet	Mass Flow Rate	$\dot{m}_{out,LE}$	1.99x10^{-3}kg/s
Mid Tip Outlet	Mass Flow Rate	$\dot{m}_{out,Mid}$	9.67x10^{-4}kg/s
TE Tip Outlet	Mass Flow Rate	$\dot{m}_{out,TE}$	1.79x10^{-3}kg/s
Cascade Walls	Temperature	T_W	543 K

face. These calculations were conducted on two cases to create the difference plots between an uncooled and cooled case and thus, obtain the film cooling efficiency over the blade surface.

To isolate the interaction of the coolant flow with the mainstream hot gas over the blade surface, the blade walls are insulated. For the uncooled case, only the blade surfaces are set to adiabatic. For the cooled case, both blade and core surfaces are insulated. It is not necessary to conduct the CHT case since only the flows interaction is under study. Hence, the CFD model contains both fluid domains, eliminating the solids from the CHT model. Any other boundary conditions defined in the BL case remain as previously shown. The difference between the two cases is defined as

$$\Delta FCE = \frac{T_{\mathrm{H}} - T_{aw,x,i}}{T_{\mathrm{H}} - T_{\mathrm{K}}} - \frac{T_{\mathrm{H}} - T_{aw,x,o}}{T_{\mathrm{H}} - T_{\mathrm{K}}} = \frac{T_{aw,x,o} - T_{aw,x,i}}{T_{\mathrm{H}} - T_{\mathrm{K}}} \tag{3.1}$$

with $T_{aw,x,i}$ as the local adiabatic wall temperature of the cooled geometries, $T_{aw,x,o}$ the local adiabatic wall temperature of the uncooled case, T_{K} is the coolant total temperature at the root inlet and T_{H} is the hot gas total temperature at the inlet. With this definition, it is easy to see that lower $T_{aw,x,i}$ are desired in the pursue of film cooling efficiency enhancement. For the sensitivity analysis throughout this thesis, film cooling effectiveness difference plots will be used to point out the different benefits, gains and loss by introducing a coolant over the surface. For simplicity reasons, the variable ΔFCE will be further referred as simply film cooling efficiency (FCE).

3.3.3 Isothermal Wall Model

Typical turbomachinery flows too complex to be predicted alone with the aforementioned definition. Therefore, it is of crucial importance to run heat transfer coefficient calculations to understand the nature of both aerodynamics and heat transfer enhancement. Throughout this work in specific cases, together with film cooling efficiency plots, heat transfer coefficient plots will be used to make a comparative study and detect the local spots in which heat transfer is being enhanced or reduced. Naturally, HTC calculation involves the interaction between both flows and also depicts convective cooling effects. FCE plots allow to capture the injected coolant and hot gas interaction by eliminating any convective cooling effect. HTC plots will also help detect the specific regions in which heat transfer is being enhanced by the presence of secondary flow structures, as shown in Subsection 2.4.2. Thereby, both plots together create a more complete picture in heat transfer prediction.

To create these plots, two cases are conducted to then calculate the difference between them. In these models, the blade walls are set to a constant temperature. This temperature is defined as the average temperature of the blade surface from the CHT model and, for each case, subtracting and adding a defined temperature difference ΔT subsequently. Finally, the heat transfer coefficient is calculated from the heat flux and temperature difference between each case. The blade temperature for both models can be defined as

$$T_{\text{Blade,1}} = \overline{T}_{\text{Blade}} + \Delta T \tag{3.2}$$

$$T_{\text{Blade,2}} = \overline{T}_{\text{Blade}} - \Delta T \tag{3.3}$$

with $T_{\text{Blade,1}}$ and $T_{\text{Blade,2}}$ as the blade temperatures of each conducted case. The general equation for heat flux transfer through the blade surface is

$$\dot{q}_{\text{Blade}} = h(T_{\text{Blade}} - T_{\text{H}}) \tag{3.4}$$

with h as the blade heat transfer coefficient. For each case, the blade temperature is replaced by $T_{\text{Blade,1}}$ and $T_{\text{Blade,2}}$. The heat flux difference between these two models can be written as

$$\dot{q}_{\text{Blade,1}} - \dot{q}_{\text{Blade,2}} = h(T_{\text{Blade,1}} - T_{\text{Blade,2}}) \tag{3.5}$$

Solving for h, the HTC can be finally defined as

$$HTC = \frac{\dot{q}_{\text{Blade,1}} - \dot{q}_{\text{Blade,2}}}{T_{\text{Blade,1}} - T_{\text{Blade,2}}} = \frac{\Delta \dot{q}_{\text{Blade,1-2}}}{\Delta T_{\text{Blade,1-2}}} \tag{3.6}$$

The rest of the boundary conditions mentioned in Table 3.1 remain the same.

3.4 Mesh Generation

All meshes used within this work were generated with the hybrid mesher CENTAUR Software v14.5. This mesh generator produces high quality hybrid grids consisting of a mixture of prisms, tetrahedra and pyramids. In the boundary layer region, triangles are used as a starting point to create layers of prismatic elements in the near-wall regions. The structured nature of the prisms in the normal direction to the surface exploits the advantages of traditional structured grid approaches and also, this prismatic grid offers good orthogonality and clustering capabilities. On wall surfaces, hexahedral elements are generated by quadrilaterals (structured or unstructured). This quadrilateral faces are then grown to create layers of hexahedra and finally match the surrounding prisms and tetrahedra utilizing pyramidal transitional elements when necessary. Tetrahedral elements cover the rest of the geometry, which are blend into the prismatic grid. Tetrahedral elements are formed in one of two ways, isotropic tetrahedra or destructured prisms or hexahedra. The first one consist of only isotropically shaped tetrahedral elements with no special boundary clustering and the last one is formed by dividing the hexahedra, prisms and pyramids of a typical hybrid mesh into tetrahedral elements. Both fluid and solid domains are defined within two different zones, to then create the respective interfaces in the solver (more details can be found in CentaurSoft (2022)).

A very fine mesh to fully resolve the viscous sub-layer is required to accurately predict heat transfer. This demands an approximately unity y^+ value on all surfaces. The first cell height was adjusted in order to reach appropiate y^+ on the entire geometry. A further refinement was conducted in regions where high gradients in flow variables are expected to happen by introducing local sources in both curves and surfaces. At the same time, mesh CAD clustering was defined equal to 1 in these regions throughout the sources, to assure a smooth transition between the geometries for the used length scale. The CHT baseline model depicted in Figure 3.3, contains a total amount of 162 million cells, varying from each cooled configuration throughout this work around 6 to 15 million cells additionally. A cut section of the blade at 50% of blade height with a close-up A-A of a PS Mid row hole, is shown in Figure 3.4 to illustrate the high resolution of the mesh geometry around regions of interest.

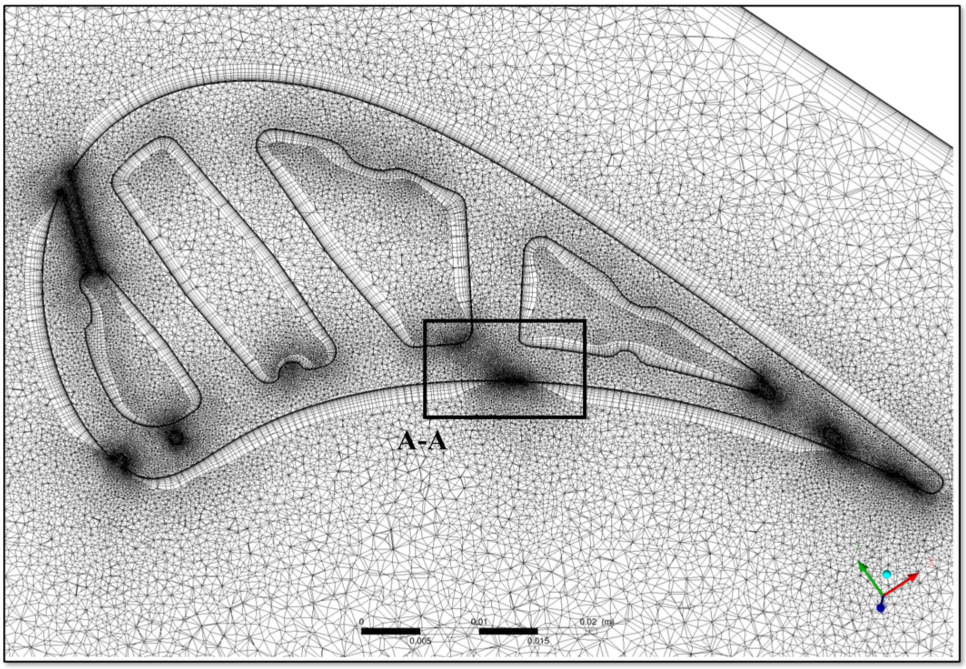

(a) Cut section of blade mesh

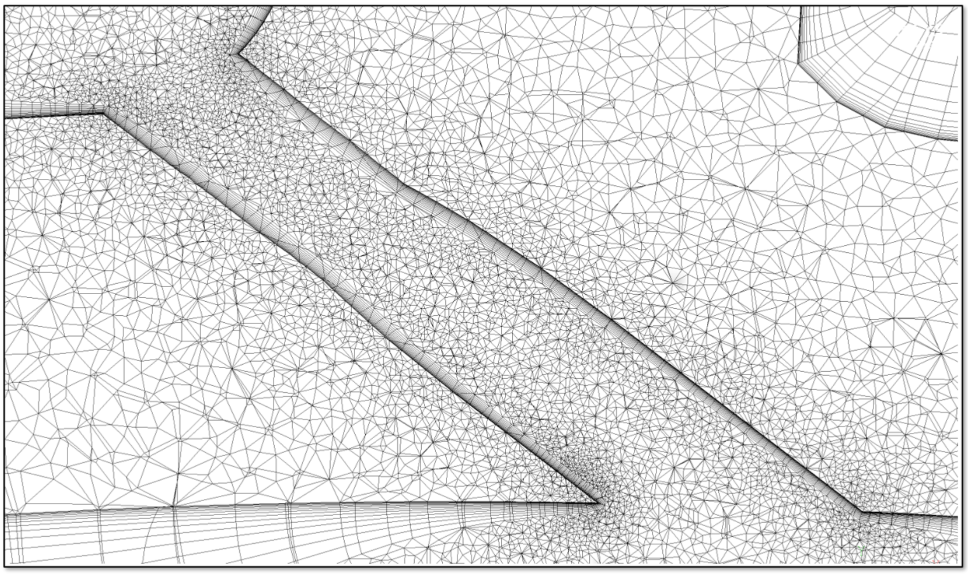

(b) Close-up A-A of mesh around PS Mid hole

Figure 3.4: Illustration of mesh quality resolution

4 Results and Sensitivity Analysis

In this chapter, all the results of the baseline model detailed in Chapter 3 and each subsequent geometry modification of the film cooling arrays are introduced and discussed. Firstly, a comparative study for the agreement of the baseline model and the experimental set-up is presented. A sensitivity study of different geometrical configurations is investigated, in order to determine the most relevant constructive and physical aspects of each cooling design. All the geometrical modifications in this work were done using Siemens NX CAD tool. The results achieved in this study, will be used as the basis for the definition of a possible manufacturable blade.

4.1 Cascade Modeling

In this section, a comparison between the thermodynamic variables of the CFD baseline model and experiment is presented. In Table 4.1 both CFD and experimental data sets are listed, noting mainly the variables at the core boundaries.

Table 4.1: Comparison between CFD baseline model and experimental results

Parameter	Experiment	CFD Baseline	Absolut Difference	Relative Difference*
$\dot{m}_{H1}$	1.17 kg/s	1.14 kg/s	-0.03 kg/s	-2.6%
$\dot{m}_{Root}$	0.02 kg/s	0.019 kg/s	$-1\text{x}10^{-3}$ kg/s	-5.2%
$p_{t,Root}$	141 167 Pa	141 162 Pa	-4 Pa	-0.8%
$T_{LE,Out}$	355 K	347 K	-8 K	-16.9%
$p_{t,LE,Out}$	134 953 Pa	134 796 K	-157 Pa	-2.6%
$T_{Mid,Out}$	349 K	342 K	-7 K	-16.9%
$p_{t,Mid,Out}$	132 262 Pa	132 039 Pa	-223 Pa	-2.6%
$T_{TE,Out}$	398 K	386 K	-12 K	-13.2%
$p_{t,TE,Out}$	124 588 Pa	124 908 Pa	320 Pa	1.9%
$\dot{m}_{C21}$	$3.17\text{x}10^{-3}$ kg/s	$2.97\text{x}10^{-3}$ kg/s	$-3\text{x}10^{-4}$ kg/s	-6.32%
$\dot{m}_{C22}$	$1.98\text{x}10^{-3}$ kg/s	$1.79\text{x}10^{-3}$ kg/s	$-1.8\text{x}10^{-4}$ kg/s	-9.3%

The relative difference for temperature and pressure variables, is the ratio of the absolute difference to the delta between the EXP and the corresponding root inlet value (root temperature or pressure). Therefore, ensuring comparable ranges between the two set-ups. To ensure a realistic mass flow split between the LE and TP1 channel, a study of the core boundary conditions was conducted. Measurement data was used, as a starting point, to define values of static pressure at core tip outlets as boundary conditions. With this attempt, a different proportion of mass flows between the channels was obtained, compared to former works. An iterative process was undertaken by modifying the boundary conditions magnitude, to achieve realistic mass flow rates at

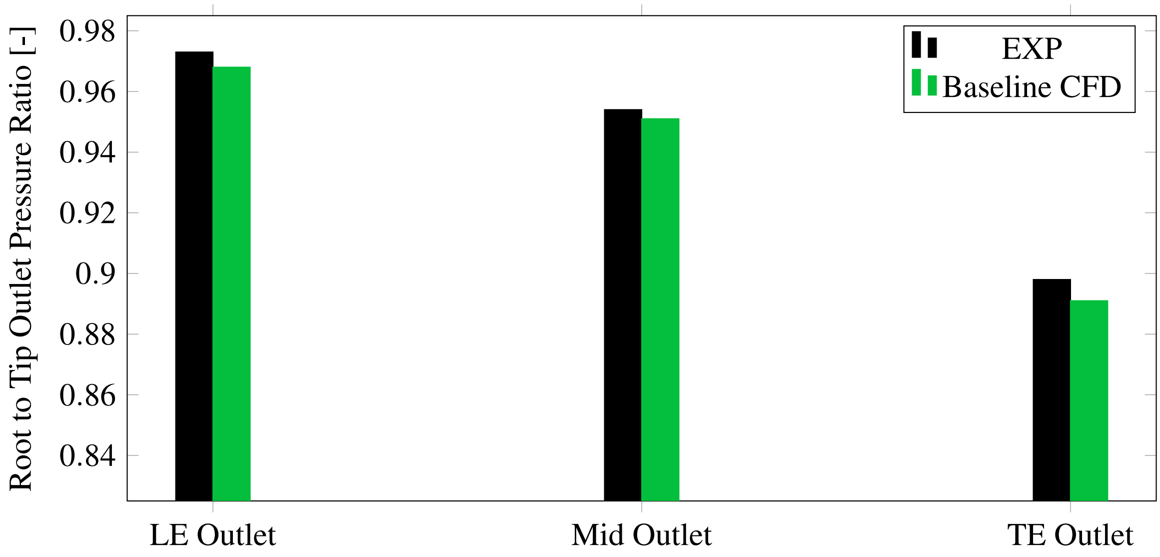

Figure 4.1: Core root to tip outlets pressure ratios

all core outlets. At the same time, it was ensured comparable temperature and pressure values. As already mentioned in Chapter 3, the baseline model does not contain the steps at the tip outlets as in the experimental set-up, since it led to deviations due to a possible re circulation zone, close to the boundary. These steps are located upstream of the pressure measurement points and they should account for an additional pressure loss, thus resulting in different pressure values at both root inlet and core outlets for the given inlet mass flow rate. Also, the model ends where these measurements were conducted while the real set-up merges the LE and TP1 channel using flanges for the connection. This connection defines the mass flow split upstream of the core while both channels are still separated. These two deviations have a considerable impact in the results of the model, since as shown in Table 4.1, it is visibly difficult to achieve similar thermodynamic variables and at the same time, equal experimental mass flow rates. From Table 4.1, it can be concluded that CFD coolant flow is heating less compared to the experiment. A remarkable difference between the two models is that the experimental blade contains insulation coating. Hence, more heat flux goes into the coolant, increasing the experimental outlet temperatures. In order to replicate realistic engine operations, it should be taken into account that at the root inlet, the compressor stage defines the pressure and not the mass flow rate. Therefore, it was decided to follow within an iterative process, similar root to tip outlets pressure ratios, since these pressure rates dominate the driven flow inside the core. In Figure 4.1 the core pressure ratios of the final baseline model are depicted, showing a good agreement between both set-ups.

A further attempt by adding the mass flow defect depicted in Table 4.1 was intended. For the LE and TP1 channel, the same proportion relative to the total mass flow inlet M_{C1} was kept, adding the remainder compared to the experiment. For the TE outlet, the entire mass flow defect compared to the experiment was added. Bigger deviations were found for an equal total mass flow rate through the core as in the experiment. This supports the idea, that even though a realistic mass flow split between the channels was obtained, the proportion may be wrong.

An under predicted heat flux by the solver used for this thesis, could also explain the lower temperature values at core outletsrd . It was also intended to have similar core pressure ratios compared to the experiment, since it was desired for the sensitivity analysis, that film cooling rows sitting on each channel worked at comparable experimental core pressure ratios.

4.2 Comparative Study of CFD and Experimental Results for Conventional Cooling Validation

Throughout this section, a comparative study between the CFD baseline model and the experimental results, is discussed in terms of total cooling efficiency (TCE). Furthermore, FCE and HTC plots are used to predict the interaction of the coolant and the mainstream hot gas. The influence of secondary flows in both turbine blade passage and film cooling jets, play a dominating role in the behaviour of the flow and the resulting surface temperatures. In this section, no further details about secondary passage flows will be given, focusing mainly on film cooling jets structures. Also, internal cooling effects are depicted, explaining the flow phenomena involved that appear in both experiment and CFD.

4.2.1 Overall Blade TCE Agreement

From Figure 4.2 to Figure 4.4, total cooling efficiency plots over the blade surface from both CFD model and experimental set-up, are depicted.

The total cooling effectiveness of the baseline case over the blade surface can be defined as

$$TCE_{\mathrm{Bl}} = \frac{T_{\mathrm{H1}} - T_{w,x}}{T_{\mathrm{H1}} - T_{\mathrm{C1}}} \tag{4.1}$$

with T_{H1} as the hot gas total temperature at the cascade inlet, T_{C1} as the coolant total temperature at root inlet and $T_{w,x}$ as the local blade wall temperature. The yellow surfaces depicted in Figures 4.2b,d and e, indicate the areas where no experimental data is available. This areas include half of the PS surface including the TE region, holes 10 and 11 from the LE PS Row and a small radial section on the SS wall. In overall, internal cooling effects are more prominent in the CFD, relative to the experiment. Specially, at the hub region, showing a remarkable difference in TCE values. This can be due to a wrong mass flow split through the channels obtained from the modeling of the cascade, with a possibly higher LE channel mass flow rate enhancing convective cooling. Also, a low cascade wall temperature defined in the model could affect such deviation. This boundary condition was not further analysed.

The LE PS row shows a good agreement between CFD (Figure 4.2a) and experiment (Figure 4.2b). From hole one to seven, it can be noted the cold spot pattern above each hole outlet. These cold spots are located downstream of the rib turbulator on the LE channel. The induced rib vortex is enhancing heat transfer downstream of the protruded surface, that promotes wake shedding, increasing turbulence and thus augmenting the TCE. A similar TCE distribution due to external cooling can be seen on both models. Downstream of hole injection, the efficiency decreases as the jets flow downstream towards the TE. For a higher LE mass flow rate, efficiency values immediately downstream of hole injection are higher in the CFD model compared to the experiment, because of a possibly higher bleeding rate. Also, a comparable deflection of the injected coolant can be seen on both models, showing a stronger inclination towards the hub on the numerical model from mid to 70% blade spanwise. Hole number 3 has a stronger deflection towards the tip, compared to the experiment. This could be due to the imported boundary condition into the cascade inlet, from the fully featured CHT model containing the flow grid. A projection from a cut section containing the thermodynamic and kinematic flow variables, downstream of the recirculation zone of the flow conditioner, was defined at the cascade inlet of the CHT baseline model. Running a fully featured model could have an impact in the behaviour of the passage flow, thus explaining the discrepancy between the set-ups.

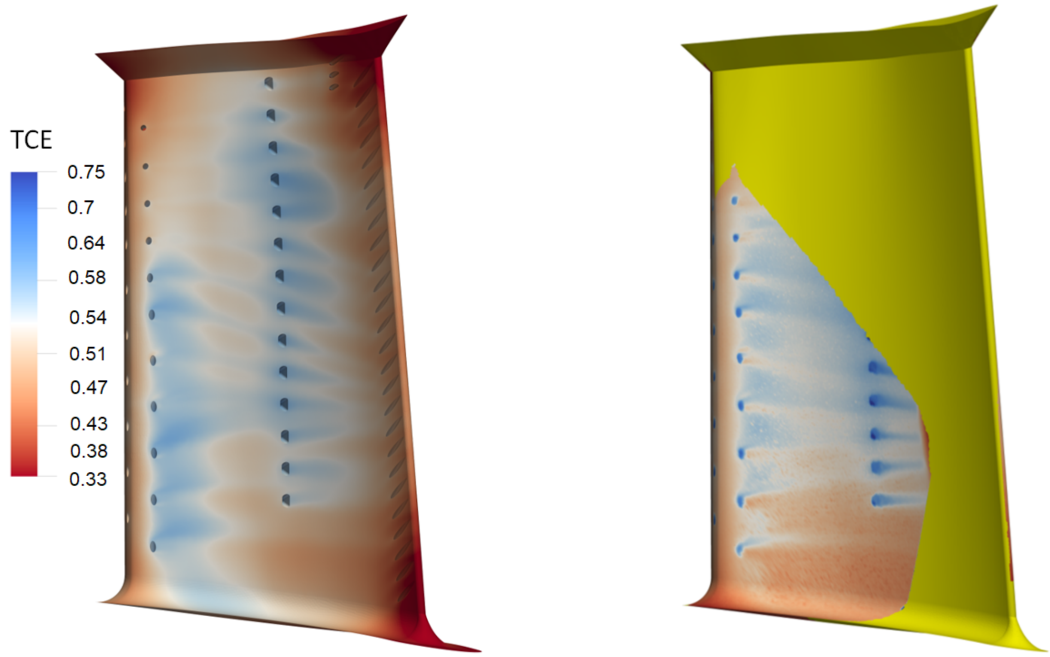

(a) PS view of CFD TCE

(b) PS view of TCE experiment

Figure 4.2: Comparative views of PS surface for TCE validation between CFD and experiment

Between the LE PS and PS Mid rows, it can be noted that in the experiment (Figure 4.2b) hot spots are less prominent compared to the numerical set-up (Figure 4.2a). Again, this leads to the assumption of a wrong mass flow split, with apparently a lower mass flow rate through the TP1 channel on the CFD compared to the experiment. Also, for a different deflection of the jet emerging from the third hole of the LE PS, the coolant spreads differently over the PS surface. Therefore, noting a more circular hot spot in the CFD compared to the experiment . On Figure 4.2b, only the first five PS Mid row holes are depicted, showing enhanced efficiency downstream of the holes. For this row, a higher efficiency at hole injection and immediately downstream can be noted on the experimental blade, compared to the CFD. Also, a different orientation of the jets for the first three holes can be noted compared to the CFD model. For a higher mass flow rate through the TP1 channel in the experiment compared to the CFD, also a higher mass flow rate is flowing through the TP2. This could account for a higher bleeding rate through the PS Mid row in the experiment compared to the numerical model, hence showing higher TCE values.

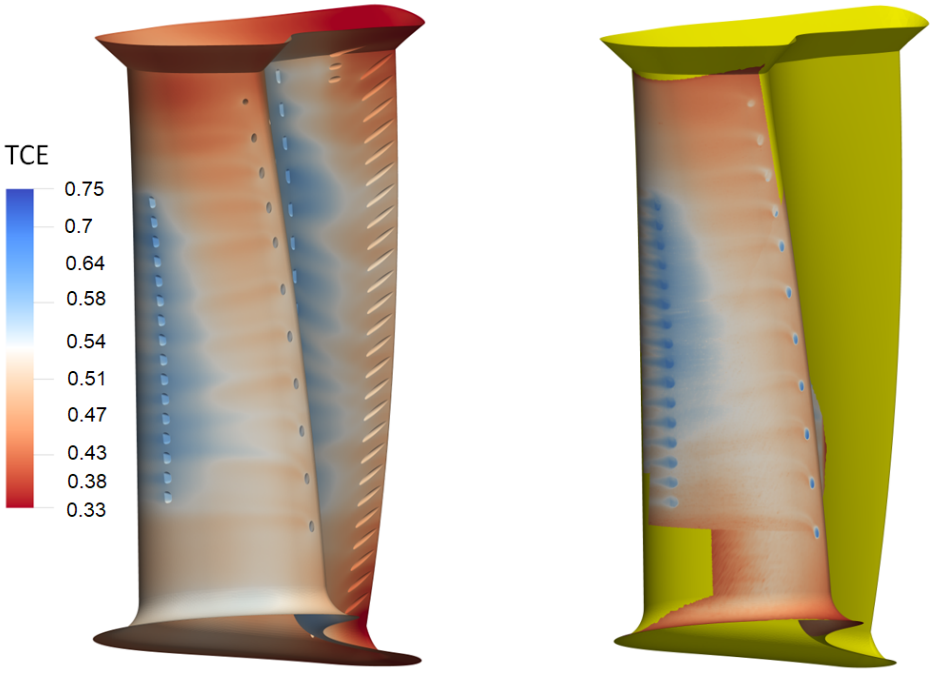

(a) SS frontal view of CFD TCE

(b) SS frontal view of experiment TCE

Figure 4.3: Comparative views of SS surface for TCE validation between CFD and experiment

The LE SS front row shows a good agreement between both models, with a similar jet deflection of the jets (Figure 4.3a and b). The deflection is more prominent in the CFD. From hole 7 to 11, an arguably higher efficiency can be observed in the experiment, compared to the numerical model. It could be due to the jets detaching at hole inlet or immediately downstream of hole injection and then, reattaching further downstream, deflected by the acceleration of the mainstream hot gas along the suction side surface. This suggests that the stagnation line may be lying closer to the suction side surface in the CFD. In this situation, the momentum flux of the jets is higher compared to the mainstream momentum flux, due to the low external velocity along the line. Thus, jets detach at hole outlet and then reattach further downstream. Downstream of the LE, the jets meet the LE SS rear row. Upstream of the following row, a cold spot can be observed. This is due to the combined effect of the upstream injected coolant reaching the LE SS rear row and convective cooling through the axial fanshaped holes.

For the LE SS rear row, a considerably higher efficiency can be observed in Figure 4.4b compared to Figure 4.4a, downstream and upstream of hole injection. From holes nine to twelve, the numerical model shows lower efficiency values compared to the experiment. This row shares

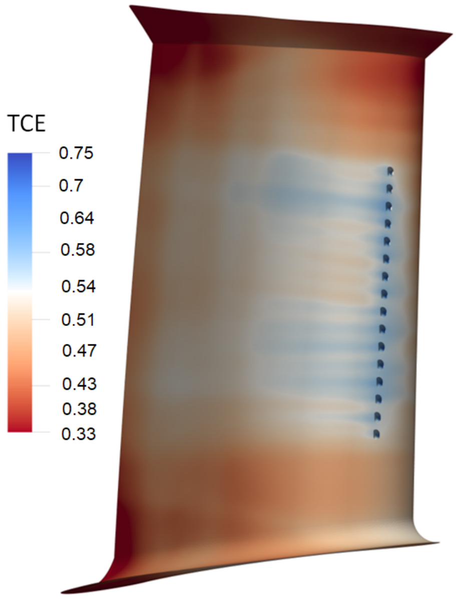

(a) PS view of CFD TCE

(b) PS view of TCE experiment

Figure 4.4: Comparative views of SS rear surface for TCE validation between CFD and experiment

the LE channel with the LE PS and LE SS row and, compared to the experiment, it seems that a higher mass flow rate should be distributed within this row in the CFD. Since the LE channel mass flow seems to be higher in the CFD compared to the experiment, the difference in pressure ratios depicted in Figure 4.1, could account for a wrong core equalisation, thus possibly different bleeding rates between the two models. The circular cold spot downstream of the injection row close to the tip on the experimental set-up, may be due to the laminar-turbulent transition. The CFD is not able to reproduce this behaviour since no transition model was implemented (Stichling (2018)).

4.2.2 CFD Prediction

This subsection will introduce an overview of the results obtained from both adiabatic and isothermal blade models, used to accurately predict the coolant and hot gas interaction. These models should correlate to the results shown in the previous subsection, used to validate the CFD with the experiment. Hence, no further details about PS Mid and TE rows will be given, since no optical access was available at these regions.

PS Surface

Due to manufacturing constrains, not all holes sitting in both LE PS and SS row share the same dimensions. This is due to the limited access for the drilling tool (Direct Laser Deposition for the experimental test rig), being constrained by the shroud. Thereby, holes sitting closer to the tip of the blade, contain a steeper angle, compared to the holes close to the hub region.

In Figure 4.5 FCE and HTC plots from the baseline CFD model, are shown. These plots are used to visualize separately the film cooling efficiency (Figure 4.5a) and external cooling (Figure 4.5b). For visual purposes, on HTC plots, holes were plotted in black to help identify them since the heat transfer coefficient calculation was conducted only over the blade surface. The HTC plots of the uncooled blade can be found in the appendix (Figure A.8), to compare the regions in which heat transfer is being enhanced or reduced.

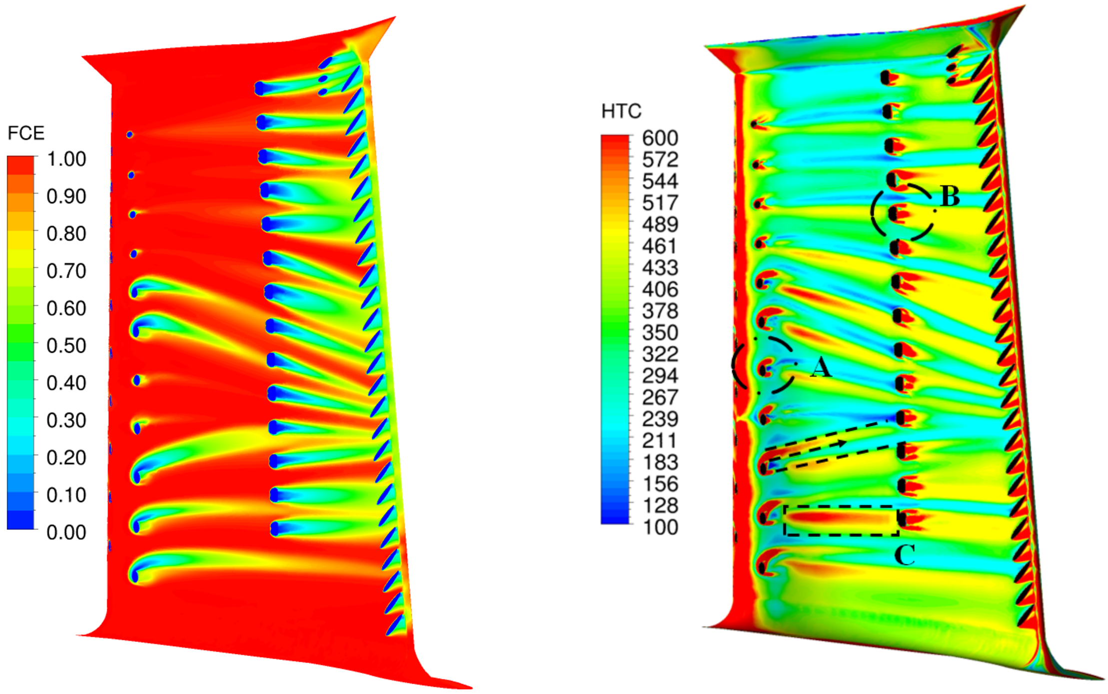

(a) PS view of FCE plot

(b) PS view of HTC plot

Figure 4.5: PS view of FCE and HTC contours

In Figure 4.5a, the LE PS, PS mid and TE row jets are depicted. For the LE PS row, holes one to 3 show enhanced efficiency at hole injection and reduced values as the jets develop downstream over the blade surface. For holes 4 and 5, the jets seem to detach and strongly penetrate into the hot gas, since intermediate to low efficiency values at hole injection and a short path away from the hole outlet, are shown. Holes six and seven illustrate a similar efficiency distribution compared to the first three holes. Compared to Figure 4.2a, it could be claimed that the adiabatic wall model used for recreating the FCE plots, is predicting reasonably well the interaction of the coolant with both flows. In Figure 4.5b, the arrow aligned with the center-line of high FCE values for hole 3 in Figure 4.5a and the black-dashed lines, serve as guides to depict the orientation and path of the jet. The lowest HTC zone in the direction of the arrow, can be observed. This low HTC streak then reaches the bottom part of the PS Mid hole 4, forming together both jets a low HTC region up to the TE row. Below the upper dashed line and above of hole outlet, high HTC values are obtained, due to the shear stresses and eddies caused by the mixing between the flows. This effect can also be noted in region **C**, downstream of hole two. The heat transfer coefficient ratio between the cooled and uncooled in this region, is bigger to one (see Figure A.8). Therefore, increasing wall heat flux. A typical HTC distribution for cylindrical and fanshaped holes can be observed at **A** and **B** with a high and low HTC pattern. The minimum value can be observed immediately downstream of hole injection in **A**. This low HTC spot is produced by the action of the coolant, creating a stagnation region underneath the jet. For the fan shape hole (**B**), the regions of enhanced HTC can be seen above, immediately downstream and below of hole outlet. For the PS Mid row, the distribution varies downstream of hole injection, when no upcoming coolant from the LE PS row is reaching the emerging jets. For hole number one in PS Mid, considerably high HTC values can be observed at both upstream and downstream regions of the hole. Upstream of the hole, no coolant is covering this area but the upper part of the hole. Thus, it can be noted above of hole injection, the low HTC streak that continues downstream, towards the TE. Even though downstream of hole one in PS Mid the efficiency is considerably good (Figure 4.5a), relatively high values can be observed due to easier hot gas penetration. This is an undesired result, since the heat flux reduction is dependent on both FCE enhancement and HTC ratio reduction (see Equation 2.13)

In Figure 4.6, a cut section through the LE PS row with velocity contours and tangential projection of velocity vectors, is shown. It contains the entire length of holes 3, 4 and 5 and the outlet and inlet conditions of holes 2 and 6 respectively. The bulk velocity u_K is depicted in black arrows for holes 3, 4 and 5. In hole number 5, a local datum axis z-r is shown in dotted-light blue arrows. Holes number 3 and 6 are sitting directly over a rib but in different position relative to the rib, hole 4 is in between ribs and a rib turbulator is located right downstream at the inlet of holes number 2 and 5. This last two having different spacing towards the rib.

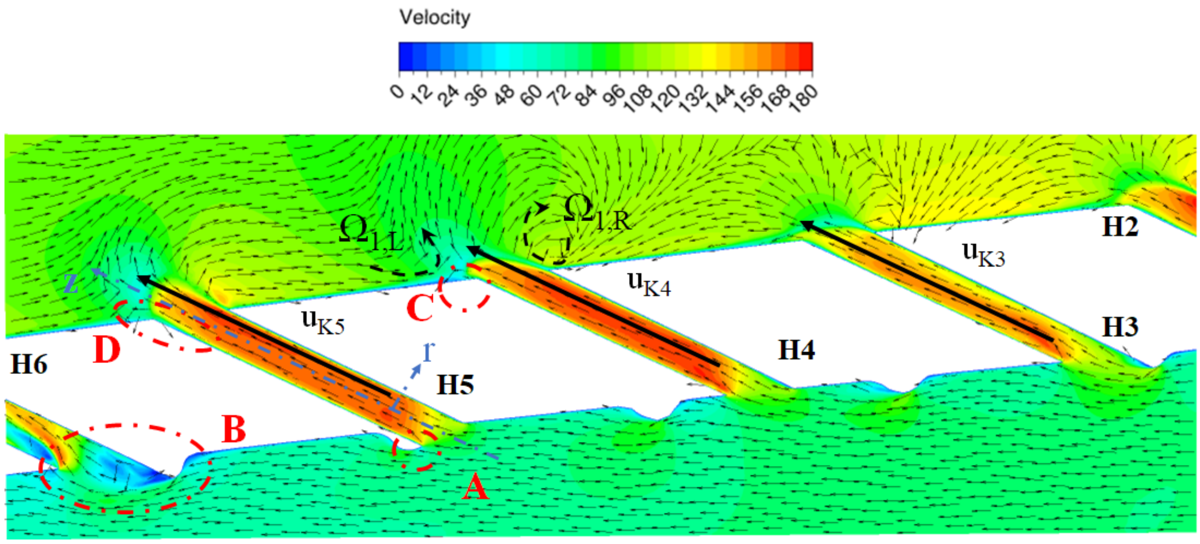

Figure 4.6: Cut section of holes 2 to 6 for LE PS row

.

It can be seen at the inlet of hole 3, that the film finds itself in the separated recirculation region behind the rib turbulator. This recirculation zone is dependant on the flow conditions and rib turbulator geometry. The height of the rib is almost half of the hole diameter. Therefore, the separation region downstream of a rib turbulator, will not entirely cover the film hole inlet. This recirculation zone contains the lowest static pressure value near the wall, due to the high flow acceleration and total pressure loss caused by the rib. This results in an aligned bulk velocity u_{K3} with its local center axis z. In Figure 4.7b, discharge coefficient values for the LE PS row, are given. The effect of a rib sitting right upfront of hole entry, is reducing the discharge coefficient as it can be seen from the sudden drop in the graph from hole 2 to hole 3. The jet emerging from hole 3 is attached at hole outlet (Figure 4.6) and immediately downstream, showing high efficiency values at the breakout position with the blade surface and intermediate values as the jets develops further downstream over the blade surface (Figure 4.5a).

For hole 4, the bulk velocity u_{K4} is slightly shifted towards the upper wall of the hole in the radial direction r from its central axis z. Since the hole is sitting in between ribs, there is no recirculation zone affecting the inlet conditions and thus, there is no reduction in local static pressure as compared to hole 3. Therefore, hole number 4 is accounting for bigger losses (Figure 4.7b) and a shifted bulk velocity towards the upper wall, with a higher magnitude compared to hole 3. This can also be observed in Figure 4.7a, showing a clear increment in the blowing rate from hole 3 to 4. It should be stated, that only the first 3 holes share the very same inclination angle. From holes 4 to 11, the inclination angle progressively increases, until reaching an almost normal angle to external surface at hole 11 (89°). From hole 4 to 6, the angle increases around 2° to 5° subsequently. A steeper angle increases the vertical momentum of the jet, in the orthogonal direction the blade surface, and reduces its forward momentum towards the blade tip, supporting jet detachment. Both inlet flow condition and geometrical parameters, assist the jet to detach and as a result, low effectiveness values are observed over the blade for hole 4 (Figure 4.5a). The jet barely attaches in the lower section of the hole outlet (**C** in Figure 4.6) and . Also, the counter rotating vortex pair Ω_1 is supporting the detachment from the blade, transporting the hot gas underneath the jet and enhancing mixing with the coolant, hence reducing the film cooling efficiency.

The bulk velocity at hole 5 u_{K5} is even more shifted towards the upper wall, compared to u_{K4}. This is due to the rib located immediately downstream of hole inlet, which is blocking the flow through the core and generating a stagnation point (**A** in Figure 4.6). Thus, increasing both C_{D} and M for hole 5. Film cooling efficiency values over the blade surface for hole 5 are similar to those for hole number 4 (Figure 4.5a). Due to the shifting of the bulk velocity along its radius and a bigger inclination angle, the jet detaches upstream of hole outlet and even lower efficiency values in the lower section of hole outlet (**D** in Figure 4.6) are shown, compared to hole number 4.

For hole number 6, the same behaviour as explained for hole number 3 occurs. The difference between these two, is that hole number 6 is sitting over the rib but slightly upstream of the center line of the protruded surface. Hole number 3 sits slightly downstream. Also, hole number six has a bigger inclination angle. This is leading to a clear jetting effect (**B**) in Figure 4.6, generating a detachment bubble immediately downstream of hole inlet. Again, the same trend can be observed for both C_{D} and M in Figure 4.7 as for hole 6, showing the lowest discharge coefficient value obtained for the LE PS row. As illustrated in Figure 4.5a, the jet stays attached immediately downstream of hole injection and develops further downstream until reaching the PS Mid row.

Leading Edge Suction Side Front Row

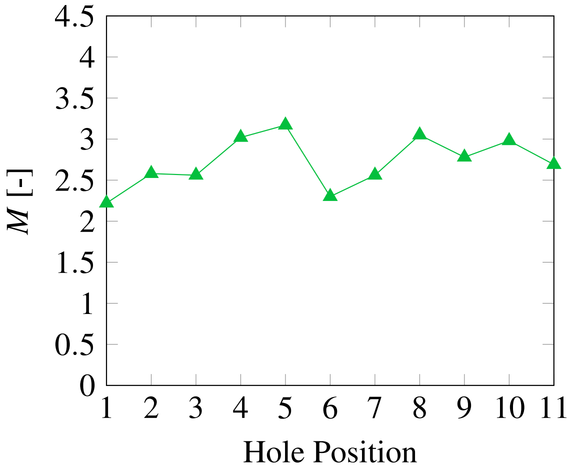

(a) Blowing Ratio

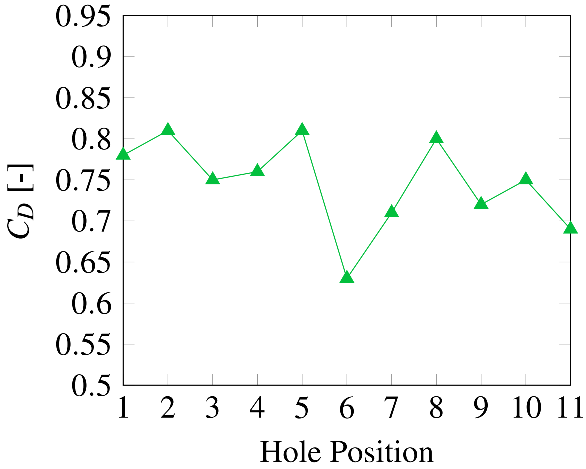

(b) Discharge Coefficient

Figure 4.7: LE PS row Blowing Ratio and Discharge Coefficient for BL

Low efficiency values can be observed in Figure 4.8a for the LE SS front row. Due to the high momentum flux ratio as depicted in Figure 4.9, jets detach at hole outlet and as the hot gas accelerates along the SS surface, jets deflect and reattach further downstream. High HTC values can be observed above and below of each hole in Figure 4.8b, due to coolant penetration into the hot gas, supported by the counter rotating vortex pair Ω_1 and enhancing the mixing between both flows. Also, high HTC values due to the very thin boundary layer over the LE region, are depicted. As illustrated in Figure 4.10b, the stagnation line is shifted towards the SS surface as suspected. The total pressure is equal to the static pressure at the stagnation line and this results in very low velocities for the mainstream hot gas. Thus, the jets lift off in the direction of the compound angle and deflect once the hot gas accelerates, consuming the coolant and explaining the low efficiency values over SS surface. Holes 1 to 5 sit closer to the LE region and holes 6 to 11 progressively increase their distance towards the TE along the SS surface.

It can be observed that while holes 7 to 10 reduce their momentum flux ratio, attachment downstream of hole outlet is improved. Also, the momentum flux ratio reduces as the mass flow rate reduces from hub to tip, progressively increasing for the last 3 holes of the row (Figure 4.9). On Figure 4.8b, the high HTC streaks above and below of each hole, almost cover the the entire path from the LE SS to the LE SS rear row.

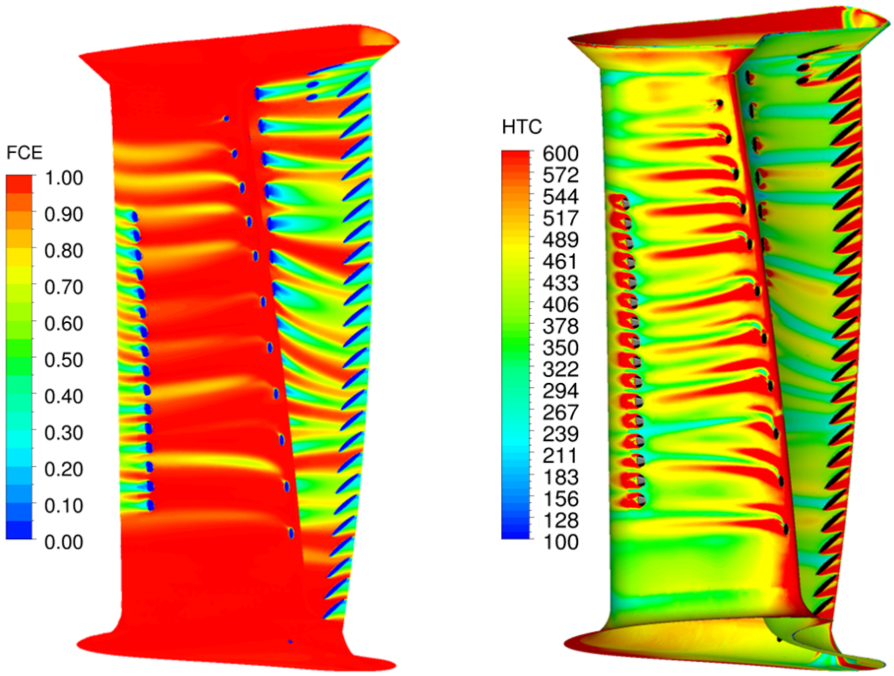

(a) SS front view of CFD FCE plot (b) SS front view of CFD HTC plot

Figure 4.8: SS front view of FCE and HTC contours

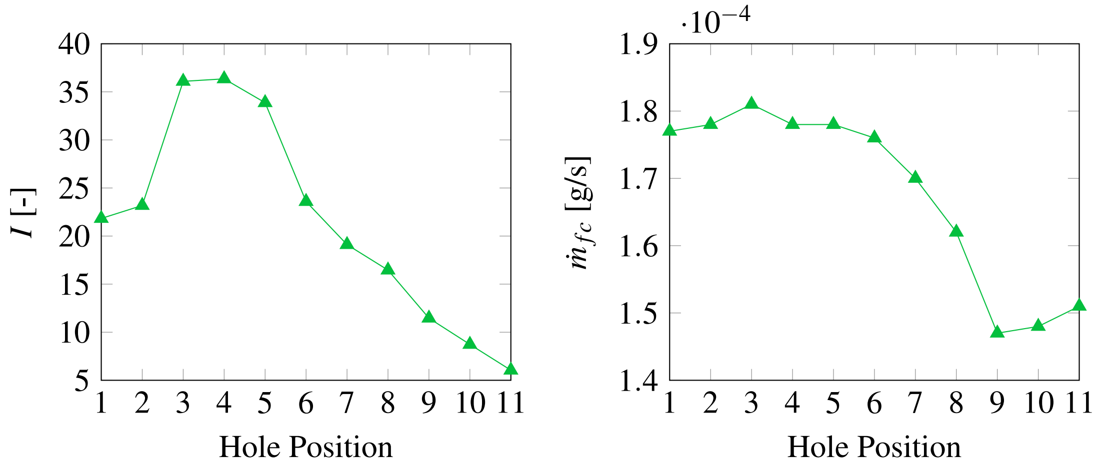

(a) Momentum Flux Ratio (b) Mass Flow Rate

Figure 4.9: Momentum flux ratio and mass flow rates for LE SS front row

Leading Edge Suction Rear Row

In Figure 4.11a and b, FCE and HTC plots for the suction side, are depicted. In Figure 4.11b, high HTC values can be observed at both hub and tip, due to the passage vortex transporting the flow from both sides towards the midpsan section. This can be seen on the low HTC streaks close to both hub and tip (separation line), as the flow migrates towards the SS surface due to the entrainment of boundary layer fluid by the PS leg horseshoe vortex. This correlates with the

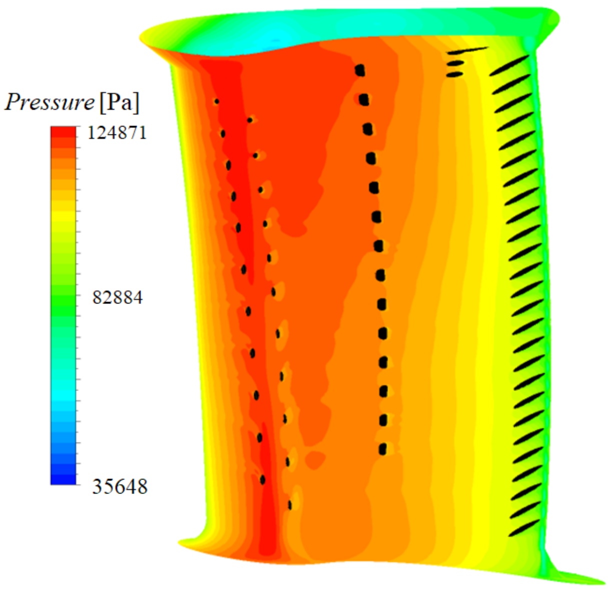

(a) PS view of pressure contours over the blade

(b) PS view of flow streamlines over the blade surface

Figure 4.10: Overview of pressure distribution and flow streamlines over blade surface

low TCE values depicted in Figure 4.4a and b. The low HTC line going straight from hub to tip in the spanwise direction, is due to the shock wave-boundary layer interaction, as the normal shock wave strikes upon the SS surface. At midpsan section, going from the LE towards the TE, relatively high HTC values are depicted, since the coolant is being carried away towards the hub and tip, as the passage vortex travels along the blade passage. In Figure 4.11a, very low effectiveness values can be observed in between jets, immediately downstream of hole injection, due to the spanwise separation. Jets meet further downstream as they spread in the spanwise direction, merging with each other and thickening the boundary layer. This results in both intermediate FCE and HTC values.

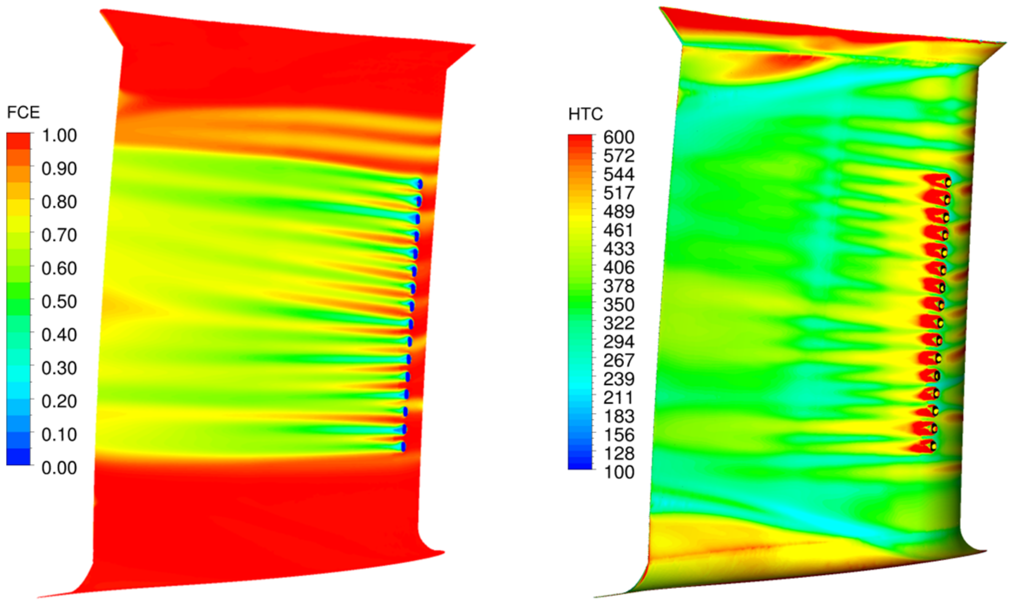

(a) SS rear view of FCE contours (b) SS rear view of HTC contours

Figure 4.11: Overview of SS rear film cooling efficiency and HTC

4.2.3 Conclusion

In this subsection, a comparative study between the numerical and the experimental test data on the baseline cooling design, was conducted in terms of TCE. Additionally, FCE and HTC plots were analysed to predict the interaction between both fluids. It can be concluded that both adiabatic and isothermal wall model, predicted well the overall cooling effects and heat transfer enhancement. The approach in following similar root to tip outlet pressure ratios may be a mistaken one, since apparently a higher LE channel mass flow rate was obtained in the numerical model compared to the test rig. Thus, explaining the deviations depicted between them. Including the steps at all three outlets and the subsequent connection downstream of the LE and TP1 channel is a must, since a different approach was undertaken throughout this thesis compared to former works, showing similar discrepancies.

Moreover, it was shown that the effects of the rib turbulators position relative to hole inlet, seem to have a notable effect downstream of hole injection for the LE PS row, in terms of FCE. Additionally, blowing rates for the LE PS row are too high, since most of the jets from this row detach at hole outlet and describe low efficiency values downstream over the PS surface. Lastly, a shifted stagnation line towards the SS surface is affecting the performance of the jets over the surface. This situation can also lead to a different bleeding rate through the holes. A stagnation line sitting closer to the LE region, will reduce the outlet hole pressure and for a similar inlet pressure, a difference in mass flow rates between the shared rows in the LE channel, could be expected. To prove this theory, a CFD model with different inlet angles should be conducted in order to obtain a different position of the stagnation line.

4.3 Sensitivity Analysis

A sensitivity analysis towards different geometrical cooling arrangements, is analysed throughout this section. In order to obtain a relative trend of the different parameters influencing the film cooling efficiency, several cases are suggested for the same variable under study. These cases will be then discussed and all the variables depicted, except noticed, will be referred relative to the cooling configuration baseline case. These parameters will be depicted as

$$X_{\mathrm{rel}} = \frac{X_i}{X_{\mathrm{Bl}}}, \tag{4.2}$$

where X_i is the parameter for the case i and X_{Bl} is the parameter of the baseline case. These are some of the parameters mentioned in Equation 2.14. For the sensitivity analysis, FCE and temperature difference ΔT plots, are used. This temperature difference is defined as

$$\Delta T = T_{\mathrm{w,x,Bl}} - T_{\mathrm{w,x,i}} \tag{4.3}$$

with $T_{\mathrm{w,x,Bl}}$ as the local wall temperature of the baseline case and $T_{\mathrm{w,x,i}}$ the local wall temperature of the case i. For positive values, the local temperature from the case i is lower compared to the baseline case. For negative values, the temperature from the baseline case is lower compared to the case i. For all the temperature difference contours depicted in this section, the baseline geometry was used to have a direct reference on the consequences of each geometrical variation.

In this section, the inlet root boundary condition is modified to a fixed total pressure boundary condition. It was observed in different geometrical configurations, with the same feed mass flow rate, that the total pressure at the inlet fluctuated around 500Pa. Therefore, the root inlet total pressure was fixed with the value from the baseline case. The rest of the boundary conditions remain as shown in Table 3.1.

4.3.1 Leading Edge Channel: Influence of Rib Turbulators Position

Following the results depicted in Subsection 4.2.2, a sensitivity study towards the relative position between rib turbulators and hole inlet for the LE channel, was conducted. Three cases were suggested, in which ribs were placed upstream of hole inlet, at 3 different positions.

A progressive displacement of the ribs towards the hole inlet was performed as depicted in Figure 4.12a-c. The inclination angle is only depicted for visual purposes. This study was done in order to generate a recirculation zone, that could account for a decrease in the blowing rates for the LE PS row. This could lead to an improvement in FCE over the PS surface, by reducing jet detachment. In Figure 4.13, a comparison between all three cases in terms of FCE, is given.

For case number one (CI), the ribs were placed ~ 1.2mm upstream of hole inlet, case number two (CII) at 0.6mm and for case number three (CIII) the ribs were place right at hole inlet. The LE channel contains a total amount of 15 ribs inclined 45° relative to the direction of the flow, with a height of ~ 1mm. For this study, 2 ribs were removed to ensure each hole having only

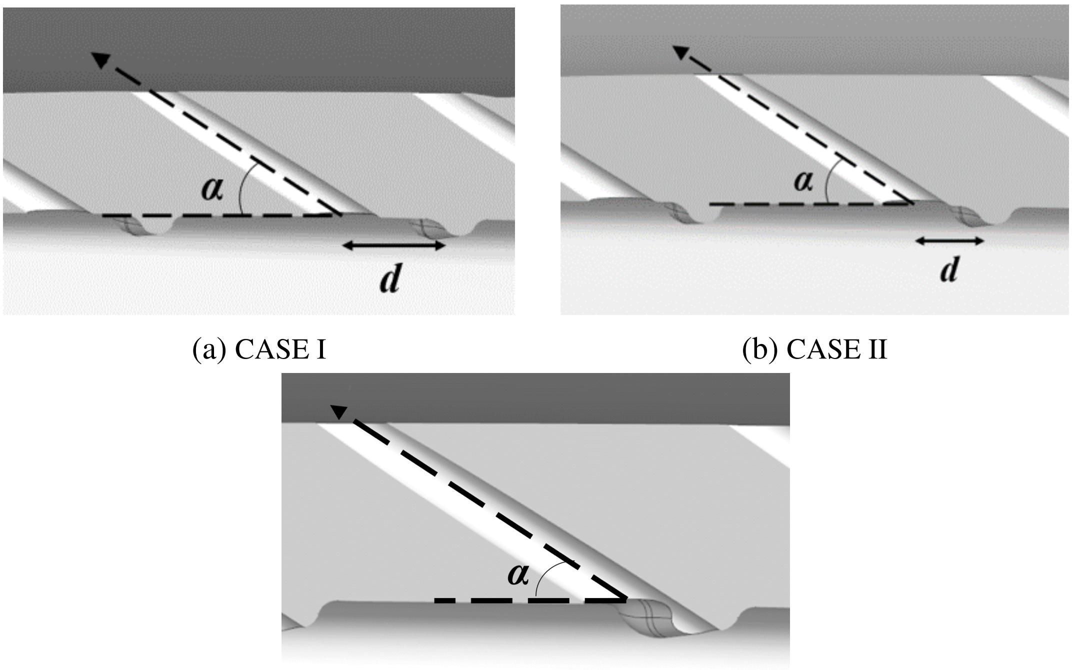

(a) CASE I (b) CASE II

(c) CASE III

Figure 4.12: Comparative overview of different rib position

one rib upstream of hole inlet and the remaining ribs being placed at both beginning and end of the heated path of the channel.

As it can be seen in Figure 4.14a and b, both blowing ratio and discharge coefficient diminish as ribs sit closer to hole inlet (from CI to CIII) for holes 1-5. From hole 5 to hole 6, the trend is the same for all three cases. As the compound angle increases towards the tip, the last 4 holes experience the same behaviour increasing both blowing rate and discharge coefficient. It was observed that the total pressure increased along the channel for each subsequent case (CI to CIII in ascending order), compared to the baseline case. By removing 2 rib turbulators, the pressure losses reduced. At the same time, by the observed trend, the combined effect of placing ribs close to hole inlet seem to account for lower pressure losses. This behaviour combined with the increment of the compound angle from hub to tip, resulted in a reduced efficiency from holes 7 to 11 in all 3 cases. The latter one, showing a slightly improvement at the outlet of hole 7 (Figure 4.13c)

From the FCE comparison (Figure 4.5a-c), it can be observed that the efficiency of the first 6 holes improved from CI to CIII. But, compared to the baseline model, only the latter case provided an enhanced efficiency over the PS surface by 2%. This is mainly because of holes 4 and 5, which in the baseline case very low efficiency values are depicted (Figure 4.5a). At the same time, hole 7 in the baseline case shows good efficiency values downstream of hole injection and for all the cases conducted in this study, lower values were obtained.

Placing the ribs close enough to hole inlet, clearly has an effect on film cooling efficiency, being strongly influenced by geometrical parameters from both holes and rib turbulators. For

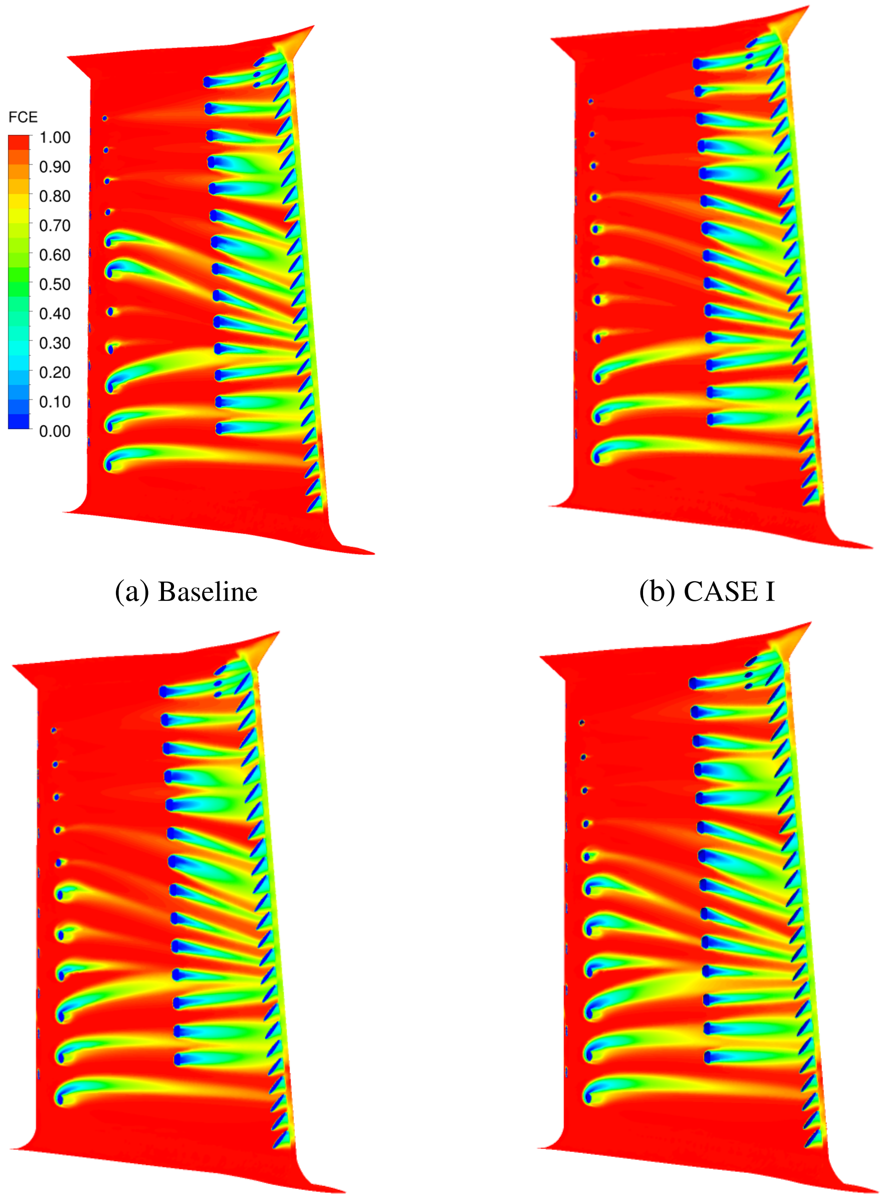

(a) Baseline

(b) CASE I

(c) CASE II

(d) CASE III

Figure 4.13: FCE comparison between three different positions for rib turbulators towards hole inlet in LE PS row

the desired effect in reducing the blowing rates by generating a recirculation region close to hole inlet, the height of the turbulator is dominating. In this study, the height of the rib is not enough to induce a recirculation zone that could cover the entire hole entry at CI and CII. Only CIII is achieving the desire effect, but limited.

The intention of this study was to analyse the effects that rib turbulators could have on the inlet conditions of the flow, enhancing FCE and leading finally to a reduction in blade temperature. Improvement in metal temperature reduction was observed only for the first five holes for the case in which the ribs are positioned right at the hole inlet. Therefore, no further details details

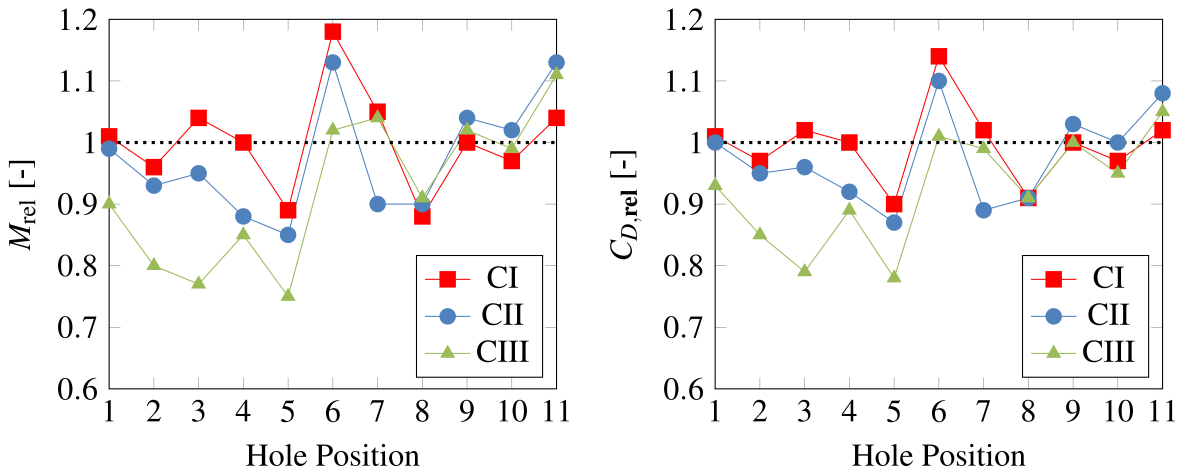

(a) Blowing Ratio (b) Discharge Coefficient

Figure 4.14: Blowing Ratio and Discharge Coefficient values relative to BL for ribs turbulators position study

will be given.

4.3.2 Leading Edge Suction Side and Pressure Side Rows

In this subsection, several geometrical modifications were conducted concerning both LE PS and SS front rows.

Outlet Hole Position Study

In the previous section, it was introduced that the stagnation line is lying closer to the LE SS front row. Therefore, a comparative study between 3 different outlet hole positions was conducted (Figure 4.15a-c), to analyse a new suitable arrangement that could reduce the blade temperature by improving FCE. The inlet hole position, remains the same.

It should be expected that, by displacing the holes out of the high pressure region, the momentum ratio of the jets reduces. Therefore, jets would not detach at hole injection and improve FCE further downstream. The geometrical variations of each case, were done by displacing each hole outlet along a constant cylindrical curve towards the TE. The displacement was done by shifting 1.2mm, 2.4mm and 3.6mm respectively from their original position. These modifications were applied on both LE PS and SS front row, but only the results for the SS front, are depicted.

In Figure 4.16, temperature difference contours for each case, are given. The FCE for CI, showed the worst performance of all 3 cases in appendix (Figure A.1a-c). This is due to a reduction in the length of the holes. By following a constant cylindrical curve along the blade surface, the holes shifted backwards. This resulted not only in shorter holes, but also the inclination angle increased. Hence, jets detach at hole outlet due to an increment in vertical momentum, in the direction normal to the blade surface. At the same time, for a similar inlet

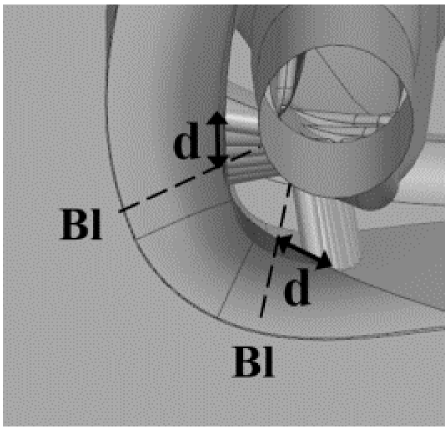

(a) CASE I

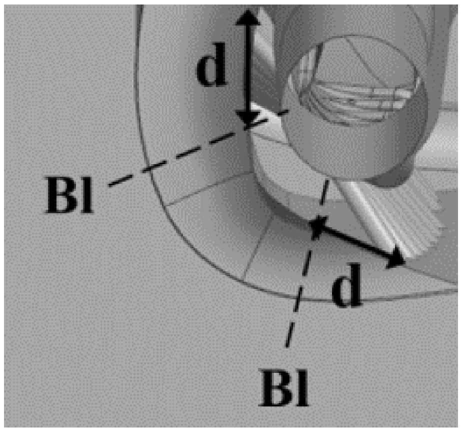

(b) CASE II

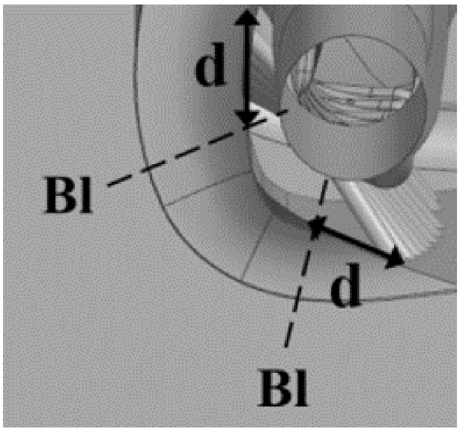

(c) CASE III

Figure 4.15: Comparative overview of outlet hole position

pressure, shifting the outlet hole position to a lower pressure region, resulted in an increased film pressure ratio for a shorter hole. Thus, it can be seen in Figure 4.16b, an increment in the mass flow rates through the holes.

From CI to CII, FCE considerably improved. This is because for CII all the jets except for hole 11, attached at hole outlet. For CII, both length and compound angle increased, augmenting the pressure loss along the holes. For CIII, the highest metal temperature reduction was observed, improving FCE compared to CII, downstream of hole injection. As the the distance from the holes to the LE line progressively increases (CI to CIII) the streamwise angle varies to a more shallow value. It would be reasonable to argue, that this modification (which was not intended from the beginning) is indeed supporting the increment in FCE. This is due to the improved lateral spreading that the flow experiences by moving to a shallow streamwise angle (see Figure 4.10b).

The progressive shifting has a clear impact in momentum flux ratio reduction, in comparison to the baseline case, for all holes in the SS front row (Figure 4.17a). This result was expected, since moving to a lower pressure zone, increased the mainstream hot gas momentum flux. No similar effect can be observed in terms of bleeding rates as, in average, the consumption rate

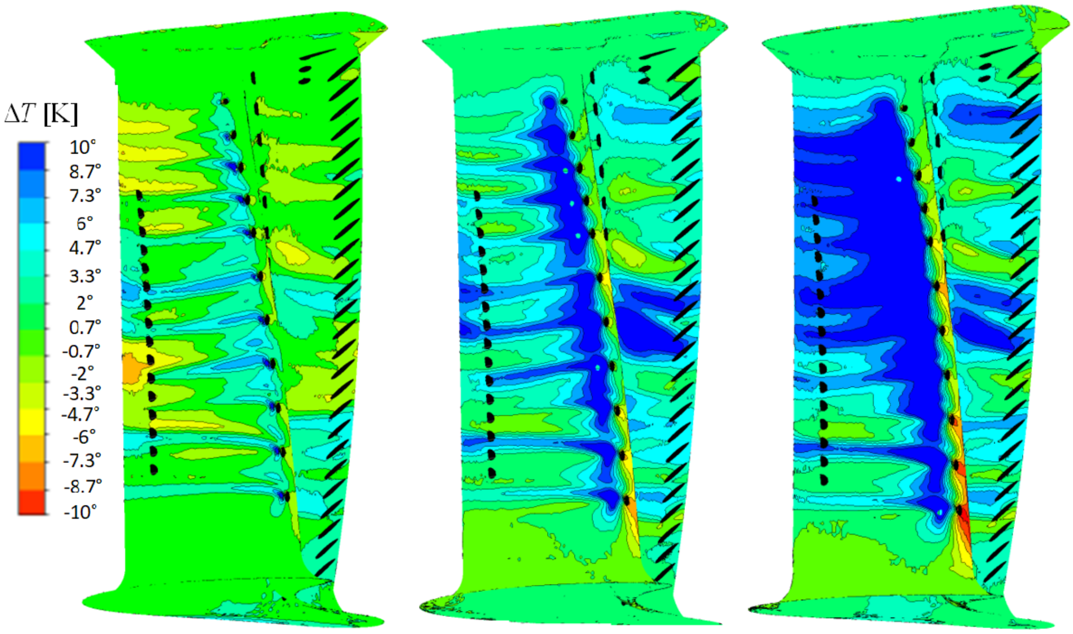

(a) CASE I (b) CASE II (c) CASE III

Figure 4.16: Blade metal temperature difference contour for outlet hole position study

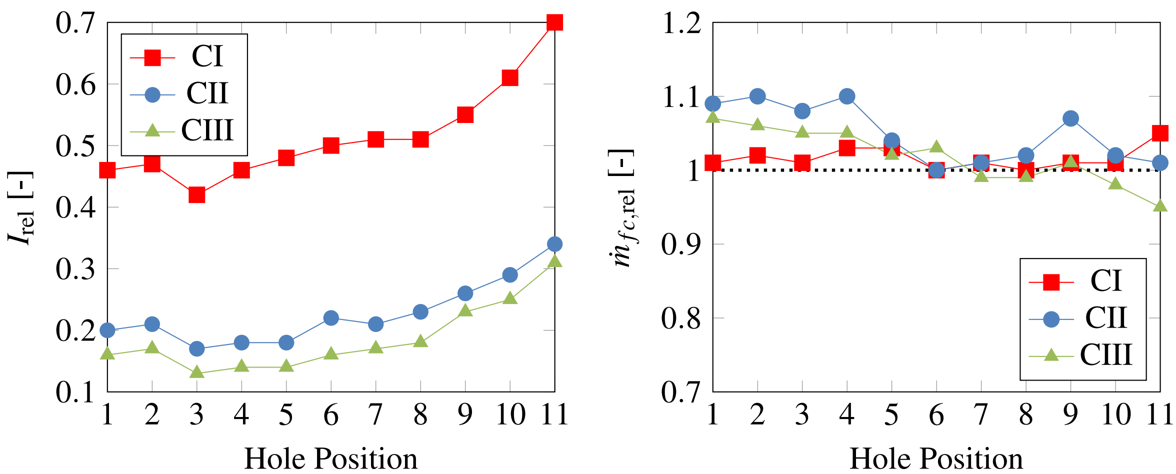

(a) Momentum flux ratio (b) Mass flow rate through holes

Figure 4.17: Momentum flux and mass flow rates for outlet hole position study

remains similar to the baseline case. From Figure 4.16a-c, it can be observed upstream of hole injection, how the temperature increases. This is because, for the baseline case, this region was covered by the hole length through the metal and, after the displacement was conducted, this region is not being cooled as before. Therefore, increasing metal temperature at the LE from CI to CIII. This is an undesirable result, which indeed was expected, since it requires very low oxidation of the material in this region, to then lead to final failure.

It can be concluded that, in order to reach higher FCE values by shifting the holes with the method explained, it requires to move the holes a considerably long distance. This has an impact in the most exposed region due to the high heat fluxes upon the LE surface. None of these modifications will be taken into consideration for a possible new cooling arrangement for blade manufacturing.

Inclination Angle Study

A sensitivity study towards the inclination angle on both LE PS and SS front rows, is introduced. To reduce the blowing rates and account for an improved efficiency, 3 different cases with $\alpha = 25°$, $\alpha = 20°$ and $\alpha = 15°$ were conducted. In Figure 4.18a-c, an overview of the sensitivity study is shown.

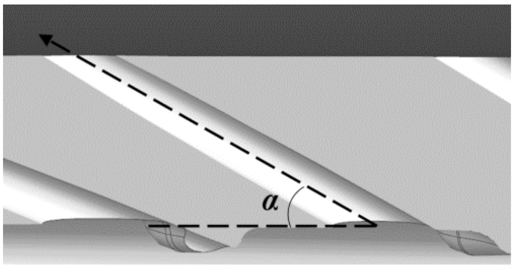

(a) CASE I.

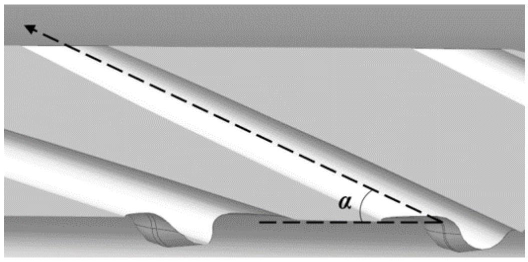

(b) CASE II.

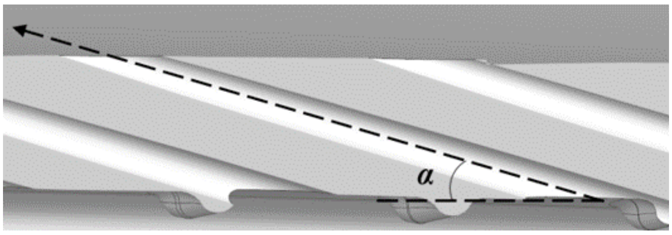

(c) CASE III.

Figure 4.18: Comparative overview of inclination angle variation.

This was performed, by fixing the outlet hole position and moving towards the hub, its inlet position over the core. In Figure 4.19, temperature difference contours over the blade surface are given.

In general, FCE values considerably improved by moving to a more shallow inclination angle (see Figure A.2 and Figure A.3). This is mainly because of the reduction in the vertical momentum normal to blade surface and an increment in the forward momentum. Going from CI to CIII, it can be observed that the spreading of the coolant increases, with a coverage area reduction for the latter one, compared to CII. In general, all blowing rates for the given configuration on PS row, fluctuated around the baseline case (Figure 4.3.2a). For CI and CII, their lowest blowing rate values in hole 5 and 2 respectively, is due to a rib sitting stream of hole inlet. The opposite was observed for the SS front, with lower values compared to the baseline case. The behaviour in the fluctuation of the discharge coefficient (Figure 4.3.2a) is due to the resulting relative position of the hole inlet towards the rib turbulators (see Subsection 4.2.2).

In Figure 4.21, a mass flow split comparison between all 3 cases for both PS and SS front rows, is depicted. All 3 cases for each row, have a lower total mass flow consumption compared to

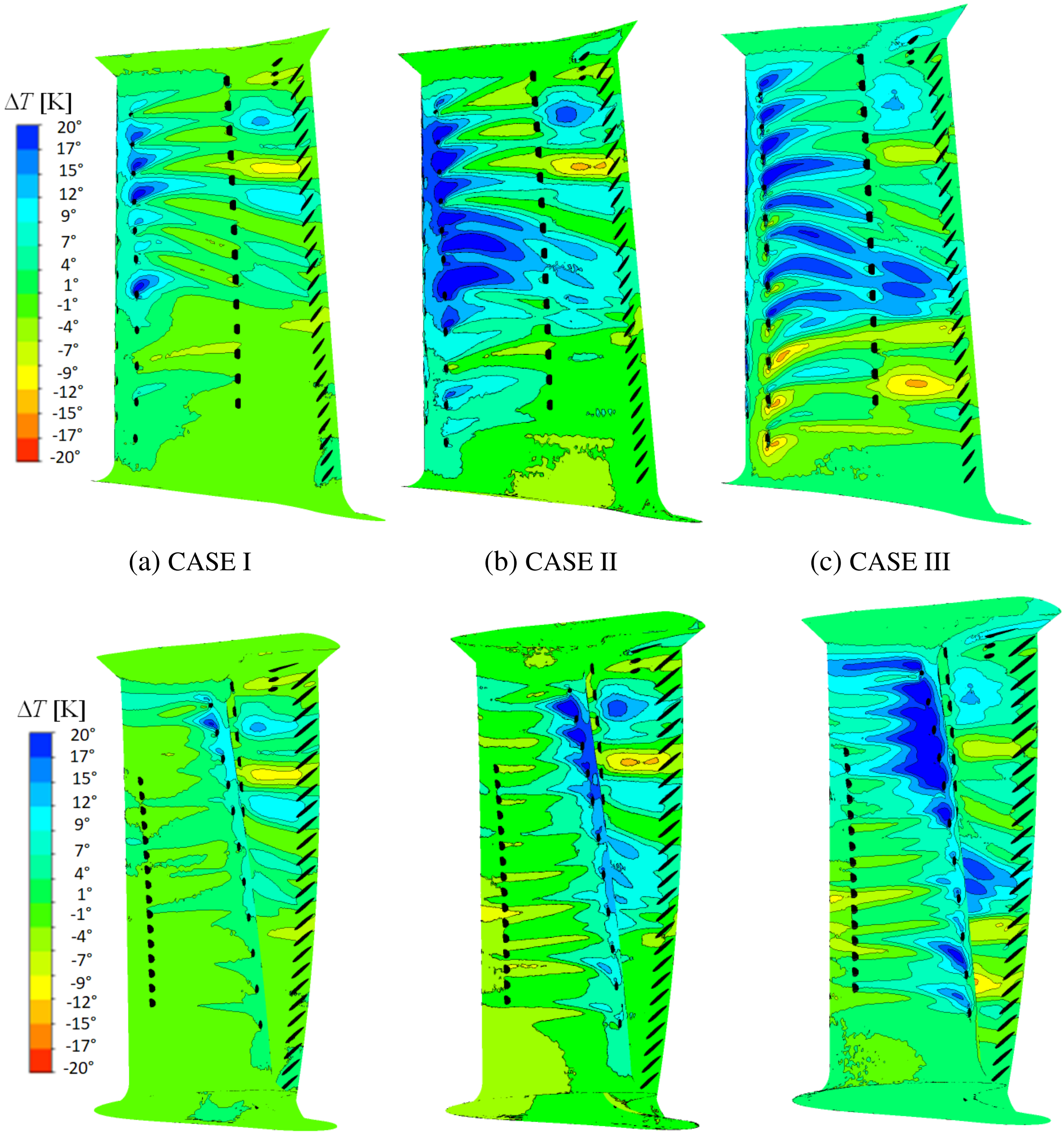

(a) CASE I (b) CASE II (c) CASE III

(d) CASE I (e) CASE II (f) CASE III

Figure 4.19: Metal temperature difference plot on LE PS and SS front for inclination angle study

the baseline case. This is a very interesting result, since with less mass flow rate compared to the BL case, higher FCE and metal temperature reduction values are obtained.

As it can be seen on FCE contours for the given study (see Figure A.2 and Figure A.3), the spreading of the coolant significantly improved for each case compared to the baseline case, with CII showing higher area coverage downstream of holes 5, 6 and 7. The reduction in the area coverage by the coolant from CII to CIII for these holes is due to both enlargement of the mayor radius of the final oval outlet hole shape and the mainstream hot gas direction (see

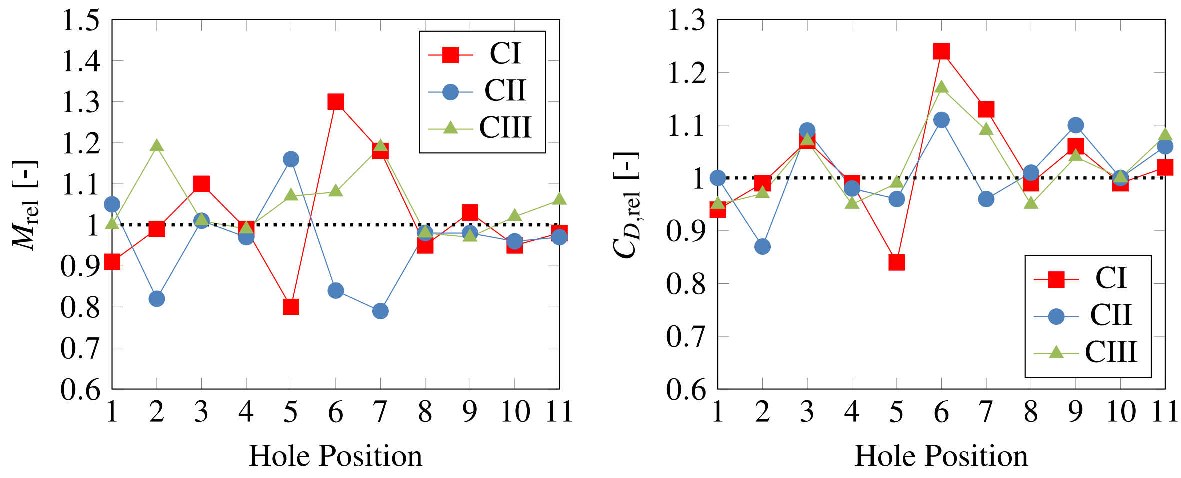

(a) Blowing Ratio

(b) Discharge Coefficient

Figure 4.20: LE PS blowing rates and discharge coefficient values relative to BL case for inclination angle study

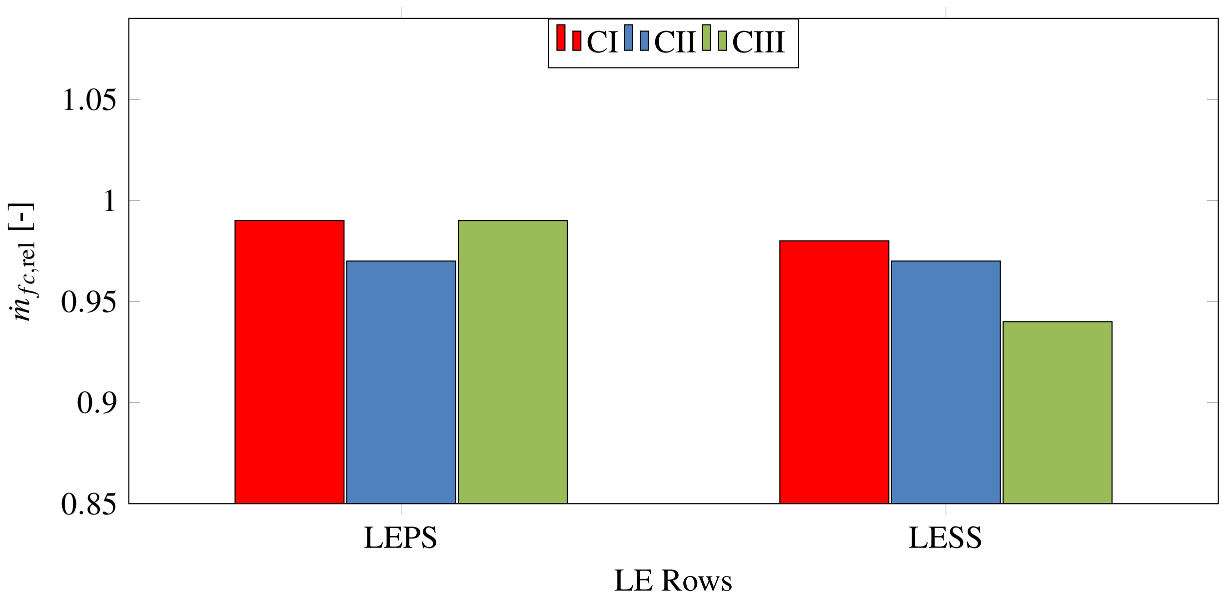

Figure 4.21: Mass flow rates comparison for LE PS and SS for inclination angle study

Figure 4.10b). The forward momentum resulting from CIII is high enough compared to CII and thus, shows a lower deflection towards the hub. Finally, jets downstream of hole injection merge differently between both cases, resulting in CII enhanced area coverage. For the LE SS front row, the best area coverage was observed in CIII, which showed the lowest momentum flux ratios of all 3 cases.

In terms of metal temperature reduction, all cases show a considerable improvement. In the direction of the holes through the metal towards the core, all 3 cases reduced the temperature, compared to the baseline case. This is due to the enlargement of the holes, increasing the area surrounded by the injected coolant and, for higher velocities (from CI to CIII), the heat transfer coefficient increases, hence enhancing convective cooling. For CIII, hot spots below holes 1 to 3 at the PS row, are shown. This is due to the modification in the outer shape of the hole, compared to the baseline case. Also, hot spots downstream of LE PS holes 1, 2 and 3 and PS Mid hole 1, can be observed. This is because of the before mentioned increment in the forward momentum, changing the distribution of the coolant downstream of hole injection compared to the BL case. This can be observed as the colder streaks produced by each jet, lies just above of each hot streak. For the LE SS front, the reduction of metal temperature severely improved for CIII, compared to CI and CII, since it was observed that the momentum flux ratio reduced progressively from CI to CIII, improving jet attachment at hole injection. Also, CIII is covering slightly a higher region towards the hub. Case number 3, in overall, shows higher temperature reductions compared to the baseline case. It was observed, that the total pressure along the normalized length of the core for CIII, was higher compared to CI and CII. This results in higher velocities through the channels, enhancing convective cooling and thus reducing more the blade temperature compared to CI and CII. The reason of this lower pressure loss for CIII is unknown.

It could be stated, that CIII showed a better overall metal temperature reduction, but this arrangement produced more hot spots compared to CI and CII. Case number 2, as observed in FCE contours, improved lateral coverage over the blade. This arrangement seems to be an ideal one between each three. Also, its inclination angle is reasonably a manufacturable one, since CIII contains a ver shallow angle, making it very difficult to implement.

Fanshaped Hole Study

Several cases with different angle fan-shaped hole arrangements were conducted on both LE PS and SS front row. Some of them, will be presented and discussed. The rest, will only be referred to and the main conclusions derived from those studies, will be shared. These geometries are depicted in Figure 4.22, with BOD as the break-out dimension of the hole with the blade surface, L_C as the cylindrical length of the hole, L_T as the transition length and L_D as the diffusive length.

A first attempt in modifying the outlet hole shape and improve FCE compared to the Bl case, was conducted. This hole will be further referred as the Baseline Fan-shape hole. Each subsequent modification of the geometries introduced in this context, were derived from this hole arrangement. The Bl fan-shape hole will be further referred as case one (CI).

The BL Fan-shape hole contains a two sided laid-back angle towards the blade metal and in the normal direction of the blade $\delta = 13.15°$ and only one sided fan-shape angle $\delta = 8.26°$ on each row (from LE to TE along both PS and SS surfaces for each film cooling row). The cylindrical section, has a slightly reduced diameter compared to the Baseline case (1.14mm) and the compound angle is the same as for the Bl model. This holes were placed on both LE PS and SS front row, by fixing the same break-out dimension for all of them (5.4mm). For the LE PS row, this resulted in similar inlet to throat length (L_T) or cylindrical length, for the first 6 holes. As the inclination angle increases, by fixing the same break-out dimension, this length reduced, giving bigger diffuser lengths for the rest of the holes of the row. The blowing ratio and discharge coefficient of CI is depicted in Figure 4.3.2.

The blowing rate increases for the first 5 holes, almost linearly. As mentioned, the compound

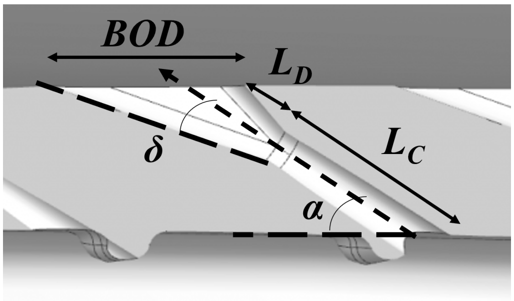

(a) CI

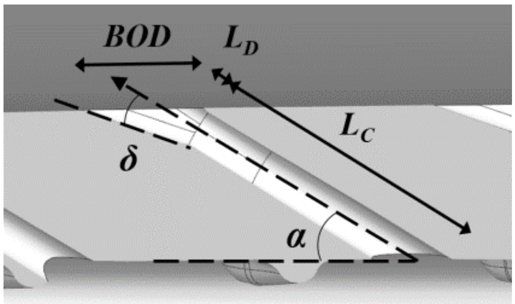

(b) CASE II

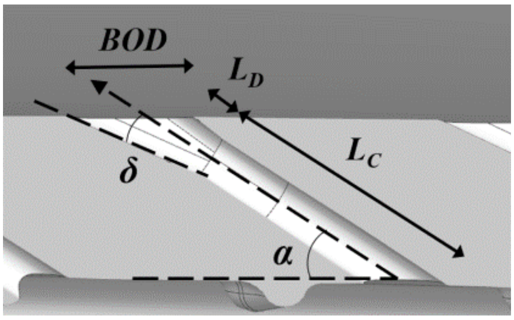

(c) CASE III

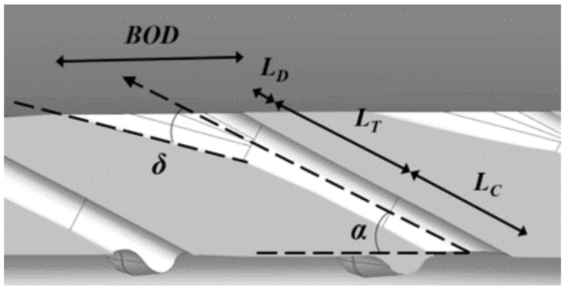

(d) FS-ST

Figure 4.22: Comparative overview of fan-shape geometries

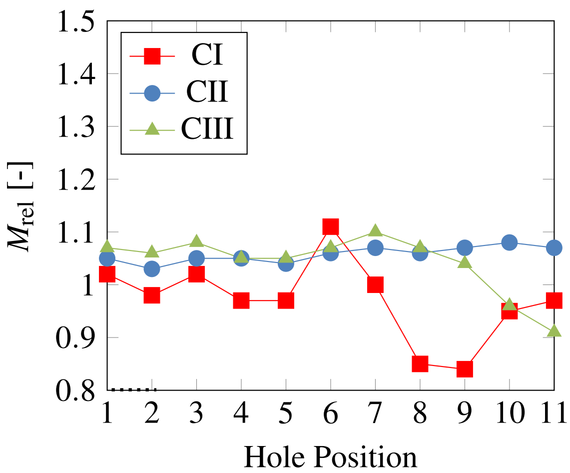

(a) Blowing Ratio

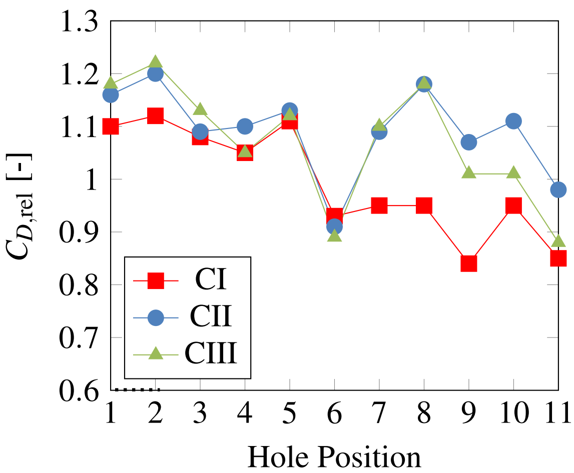

(b) Discharge Coefficient

Figure 4.23: LE PS blowing rates and discharge coefficient values relative to BL case for fanshaped holes study

angle was not modified and hole 6 is sitting right over a rib. For the next 5 holes, the blowing rate diminishes as the diffusive length increases, indicating that bigger diffuser length led to a reduced blowing rate. For the holes, it was observed the the coolant detach immediately downstream of the throat section, leading to a re circulation zone in the lower wall of the hole. At the same time, it was observed that the coolant was "splitting" immediately upstream of the break out dimension. The lower portion of the coolant diffuses towards the lower wall of the hole and, at the same time, the upper portion diffuses towards the upper wall, following the shape of the fan and increasing the vertical vorticity component (Figure 4.24a). Thus enhancing mixing and migrating the mainstream hot gas underneath the jet structure. As these two portions follow separated path, they attached to the surface, leaving a low efficiency area in between the streaks. Even though this situation occurred, the efficiency of the PS surface improved by a 7%.

A second modification from the BL Fan-shape, was done by reducing the laid-back angle and increasing the fan-shape angle ($\delta = 7.75°$, $\delta = 10°$) in order to obtain a reduced break out dimension and diffuse the coolant in the lateral direction, since it was believed that the BL fan-shape angle could have been small. A third attempt was done by shortening the cylindrical length of the before mentioned geometry. This 2 cases are referred as CII and CIII. In all holes from both LE PS and SS front row for CIII ,a jetting effect was observed, with considerably higher recirculation zones for the last 5 holes. The same but attenuated effect was observed for CII, with some cases not showing a jetting effect (LE PS holes 2, 4 and 5). For both cases, this resulted in even higher blowing rates, increasing the FCE by almost 6% and 7% for CII and CIII over PS surface. At the same time, even bigger losses were accounted for these geometries (Figure 4.3.2a and b).

Another sensitivity study was conducted in order to found a trend relative to the opening of the fan-shape angle. Three cases were conducted with each subsequent case increasing the fan-shape angle by 5°. Non of them, led to any good results in both FCE and metal temperature reduction.

With these results, it can be concluded that a big break out dimension will not help the coolant to diffuse as desired, since "splitted" streaks were found downstream of hole injection. At the same time, Very short diffusive lengths could led to a jetting effect, increasing the losses ($C_{\mathbf{D}}$) and blowing rates.

In order to help the flow stay attached inside of the hole, a smooth transition section was applied in between the cylindrical and diffusive path. The inclination angle was modified to a $\alpha = 25°$ and both laid-back and fanshaped angles were reduced to re-create a more ideal (tangential) injection ($\gamma = 7.25°$ and $\delta = 9°$. The breakout dimension was slightly reduced but not as desired for the given angles. This hole will be further referred as smooth transition hole.

This resulted in attached flow immediately downstream of the cylindrical section, improving considerably the FCE downstream of hole injection. Due to designing constrains, the break-out dimension was not considerable reduced. The resulting effect on the outflow structure compared to the BL Fan-shape hole, can be observed in Figure 4.24. The height to the center of rotation of the horseshoe vortex at the right of whole outlet, was considerably reduced. This resulted in enhanced efficiency, downstream of hole injection as the entrainment of the hot gas was highly reduced. At the same time, at the center line of the hole along the chord, the flow stays attached to the surface but further downstream splits, but with an attenuated effect. This leads to the conclusion that the assumption of a big break out dimension and flow detachment right downstream of the cylindrical path, influences this behaviour. On the upper part of the hole, in the forward direction, the flow also stays attached and a portion upstream of the upper part of the hole penetrates deeper in the mainstream hot gas.

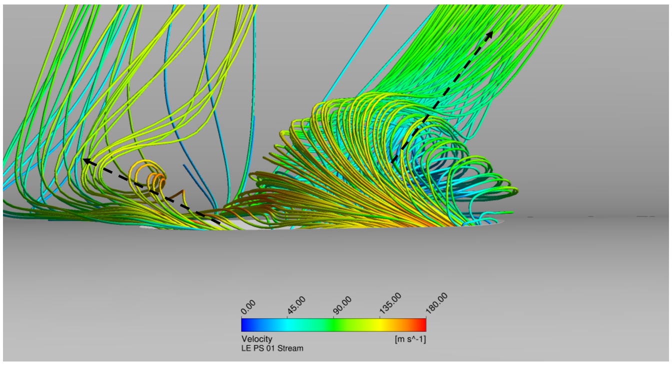

(a) LE PS Hole 1 with BL Fanshape

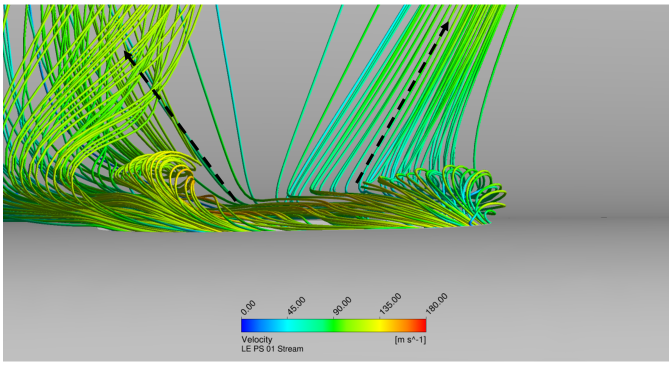

(b) LE PS Hole 1 with Smooth transition hole

Figure 4.24: Coolant flowfield comparison between fanshaped and fanshaped with smooth transition hole

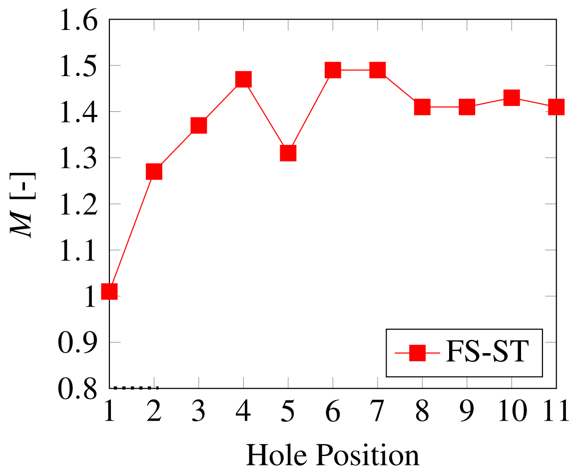

(a) Blowing Ratio

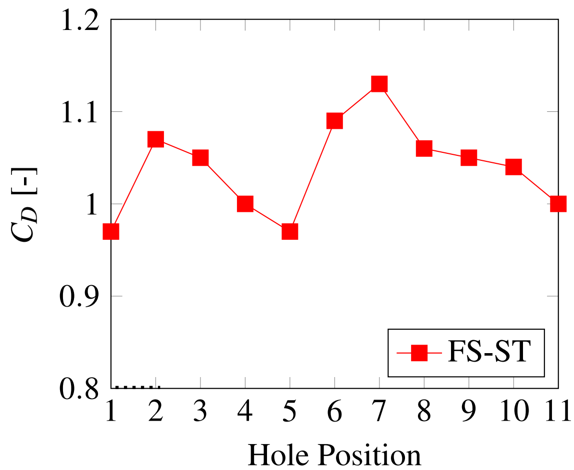

(b) Discharge Coefficient

Figure 4.25: BR and Mass Flow Rates values relative to BL for smooth transition hole

As it can be seen in Figure 4.26, the metal blade temperature reduced in almost it entire surface. The blowing rates for the smooth transition hole are considerably higher compared to the baseline case for the LE PS row and in average the losses are higher (Figure 4.3.2a and b)

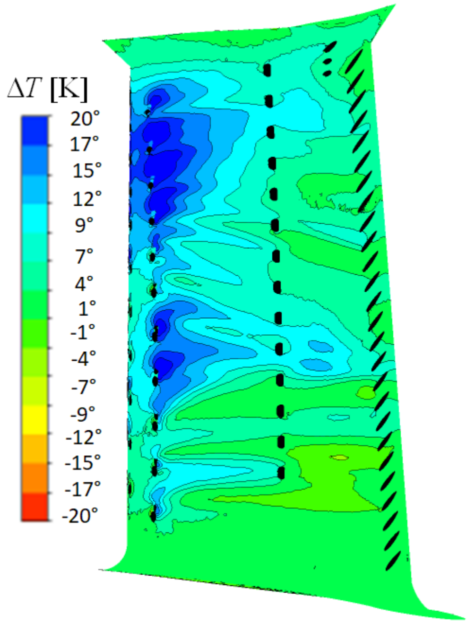

(a) PS view

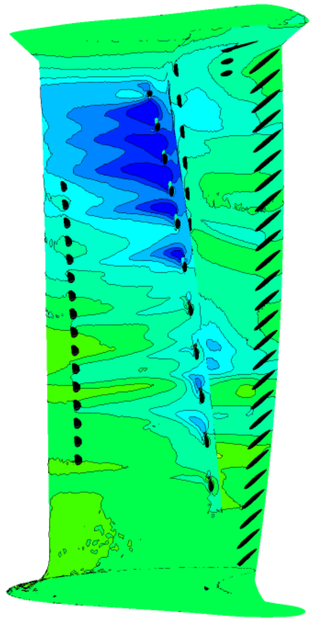

(b) SS front view

Figure 4.26: Metal temperature difference for fanshaped smooth transition hole on LE PS and SS row

This is a very good result, leading to peaks in temperature reduction immediately downstream of hole injection of around 50K.

Mass Flow Comparison

In Figure 4.27, a total mass flow consumption for each film cooling row on the LE for the fan-shaped geometries described in this subsection, are depicted. The fan shape hole with smooth transition is referred as case 4 (CIV).

As it can be seen, the mass flow consumption increases for each of the subsequent cases introduced, with CIV having the highest consumption rate. Apparently, the combined effect of the smooth transition and a relative big break-out dimension, as it was observed that the coolant filled most of the diffusive section compared to CI, CII and CIII. This is a negative point of the fan-shaped smooth transition hole, since it is consuming more mass flow compared to the baseline. It should be intended to reduce the break-out dimension and also, a more shallow angle could help reduce this mass flow consumption.

4.3.3 Leading Edge Suction Side Rear Row

Minor changes were conducted on the LE SS rear row. Three cases with different spanwise separation were conducted. Each of these cases was designed by shifting each hole, from mid span to both hub and tip, ~ 0.6mm each step.

Non of these results led to any reduction in metal temperature, but rather modified the location of the cold spots and increased the size of triangular shaped hot spots in between holes. As a

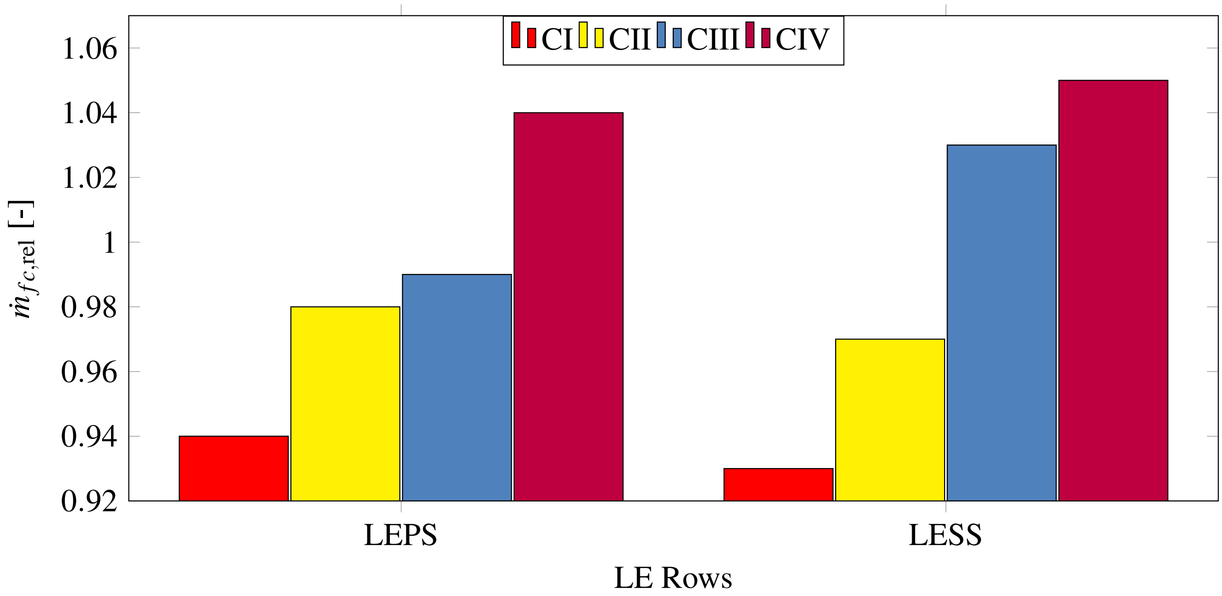

Figure 4.27: Mass flow rates comparison for LE PS and SS for fanshaped holes

result, the interaction between jets changed, leading to the mentioned increment in size of low efficiency regions.

As the spanwise separation increases, the jets downstream of hole injection behave independently, increasing the hot spots in between them and reducing the the FCE. This is due to a thinner boundary layer as the coalescence of the jets disappear (or collision when they did not merge). Most important, for the last 2 cases, a high reduction in FCE over PS surface occurred. This is because at such spanwise separation, the first 2 holes of the LE SS rear row, begun to extract coolant upstream of the LE PS row. This resulted in a reduced mass flow rate for the entire LE PS row, heavily reducing the FCE over PS surface. Therefore, this geometrical modification not only worsened the LE SS rear but also negatively influenced the PS surface.

No further studies were conducted on these row and it is considered that the efficiency from the BL case is considerably good already.

4.3.4 Mid-Pressure Side Row

On the PS Mid row, 4 different modifications were conducted. These involves increasing the fan-shape angle, increasing the laid-back angle, increasing the spanwise separation and reducing the inclination angle. All FCE plots can be seen in Figure A.5. To begin with, the fan-shape angle was increased in 5° ($\gamma = 30°$) from the baseline case geometry. This resulted in increased hot spots at hole injection and immediately downstream, as it can be seen in Figure 4.28a.

By increasing the fan-shape angle, bigger detachment of the jets occurred. Increasing the breakout dimension of the axial fan shaped holes support the jets to penetrate further into the hot gas and increase hot gas entrainment below the coolant. Thus, it can be observed the hot spots downstream of hole injection and close to the edges, as the flow is not diffusing as desired by following the fan-shaped geometry. Increasing this angle, reduced the the mass flow rate through the LE PS row. As it can be seen in Figure 4.28a, hole 6 in the LE PS row, describes a clear hotter streak over the surface, increasing metal temperature compared to the BL model.

A similar behaviour was observed by increasing the laid-back angle in 5°, as it can be seen in Figure 4.28b. The vertical component of the vorticity increased, mixing the coolant with the mainstream gas. From midpsan to hub, no modifications in metal temperature was observed. The worst case is hole number 10 as the right horse shoe vortex increases in height relative to its center point of rotation, enhancing heat transfer

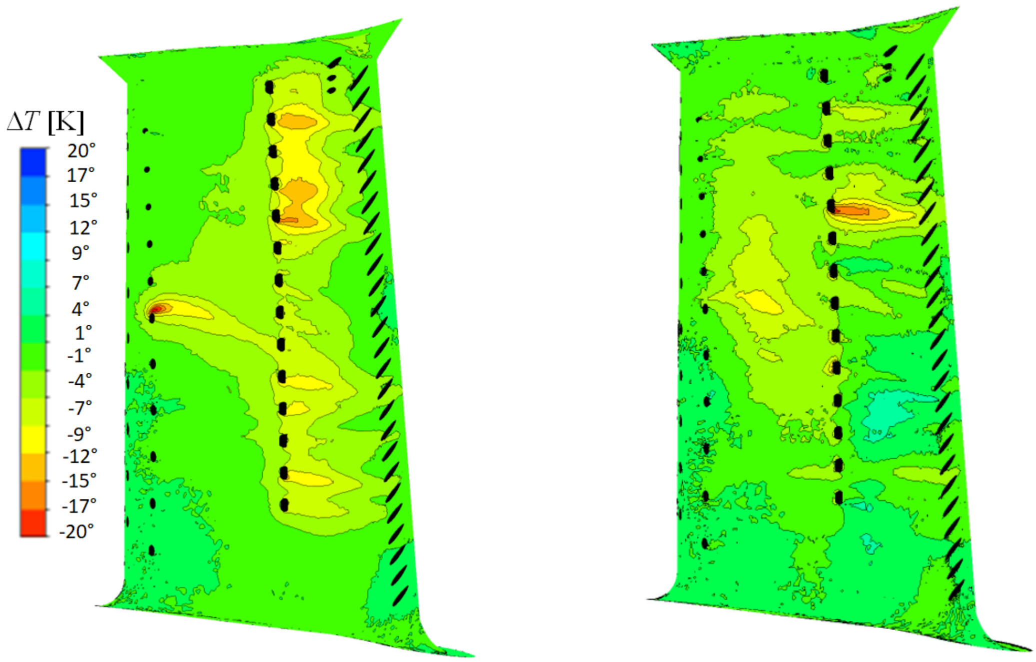

(a) PS view increased laid-back angle

(b) PS front view increased fan-shape angle

Figure 4.28: Temperature difference plots for PS mid with increased fanshape and laid-back angle

A further attempt in modifying the inlet position of the entire row, was intended. The position of the holes was shifted towards the left wall of TP2, at a constant cylindrical section. The outer position of the holes, remains the same. The idea of this modification was based on migrating to a more tangential injection. Again, this modification led to undesired results, as moving the holes closer to the left wall of TP2, positioned the inlet of the holes closer to the region in which, downstream of the u-bend connection merging TP1 and TP2, the flow heavily detaches due to its high acceleration. Thus, modifies the inlet conditions of the holes compared to the baseline case, supporting jet detachment.

A last variation was intended by modifying the spanwise separation, in order to observe the influence this row could have upstream and downstream of the TP channel. Again, this resulted in lower temperature values for the LE PS row. In this case, the reason for this behaviour is unknown. For the holes that ended close to the hub due to the increased spanwise separation, a good efficiency was observed and high reduction in metal temperature was observed. As expected, this is because in the comparison the region closer to the hub was not covered at all in the BL model. This may be a region of interest to place more holes and covered that region.

4.3.5 Trailing Edge Row

For the TE row, minor changes were introduced. A first attempt in modifying the outlet shape of the holes was done, by applying an edge blend of 0.03mm, eliminating any sharp edges to improve hole attachment and reduce mixing. This increased the outer shape of the holes and increased the mass flow rate through this row. A second try out was done by increasing the compound angle by displacing the outlet hole position in 0.6mm. The comparison between these two cases is depicted in Figure 4.29a and b.

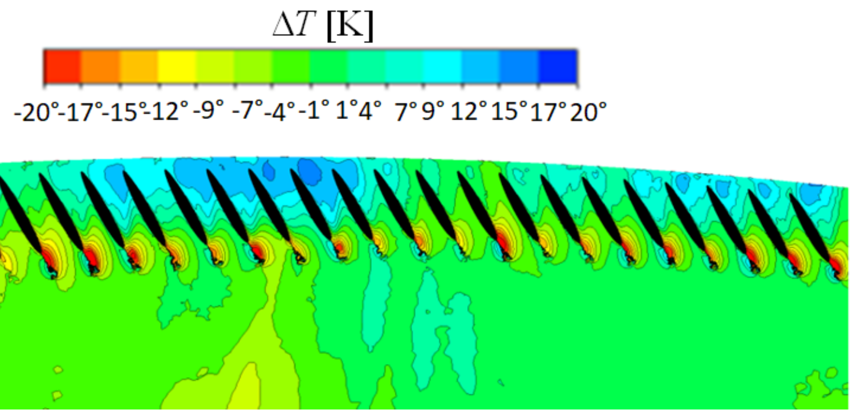

(a) PS view of TE row with edge blend

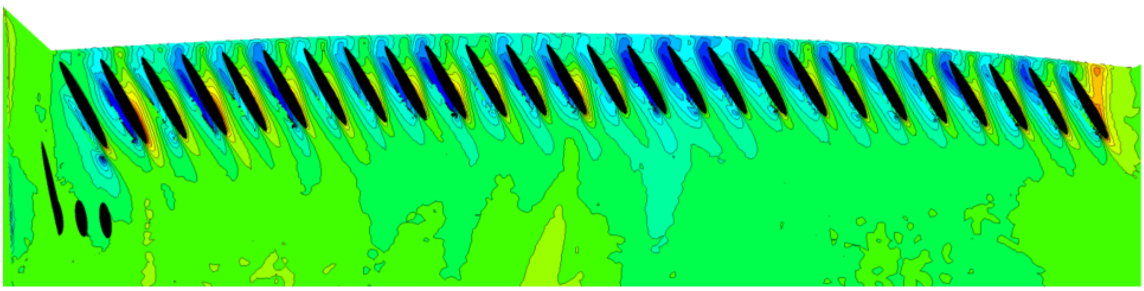

(b) PS view of TE with increased streamwise angle

Figure 4.29: Temperature difference plots for TE edge blend and increased streamwise angle

As it can be seen from the 3D velocity streamlines of the flow leaving the last two holes of the TE row (Figure 4.30a), the flow emerges at a different length of the outer hole circumference, compared to Figure 4.30b. This is due to the smoother outer shape of the holes. This is the reason why in Figure 4.29a hot spots can be seen upstream of hole injection and cold spots were the coolant attaches when emerging, compared to the baseline case. The increased compound angle, on the other hand, is supporting the flow to be transported out of the hole further upstream, compared to Figure 4.30a. Thus, increasing the regions of decreased metal temperature, compared to the baseline case. The hot spots that can be seen below the baseline position in Figure 4.29b, is due to the geometrical modification. It was observed along the TE from the SS surface, reduced metal temperatures with a more uniform distribution for a higher compound angle.

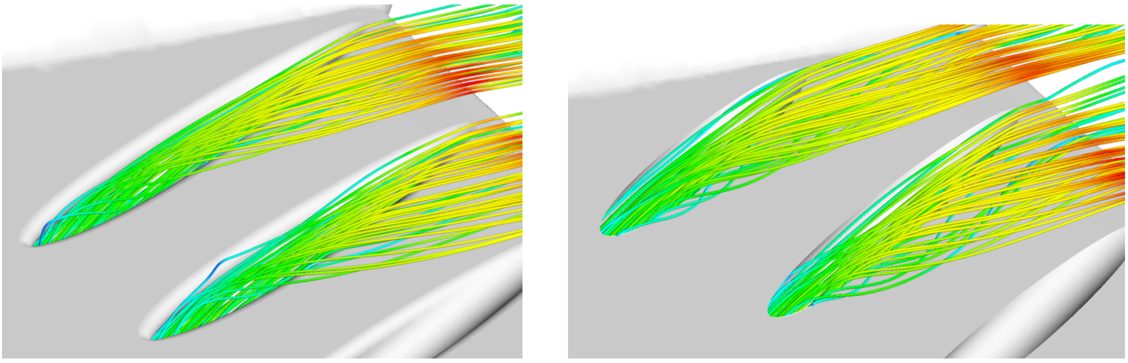

(a) FCE PS view (b) FCE SS front view

Figure 4.30: Flow field overview for TE with edge blend and inclined angle

The last geometrical variation for the TE row, was done by placing fan shaped holes on the entire row. This led to undesired results since the break-out dimension of the holes was too close to the TE fillet. Thus, the coolant severely penetrated into the mainstream, being consumed and barely covering this region. It is interesting to see, the improved performance of the last two holes, from the upper row placed in the surroundings of the tip.

4.4 Most Promising Candidates for Blade Manufacturing

After concluding the sensitivity analysis introduced for each film cooling row, two possible candidates for blade manufacturing are introduced.

Some of the previous presented geometries will remain as they are and others will be slightly modified, following the conclusions and suggestions throughout the entire work. For the first candidate (Cand. I), both LE PS and SS front contain angled fan-shaped holes with smooth transition in between, with an inclination angle $\alpha = 20°$, a laid-back angle $\delta = 8°$ and a fan-shape angle $\gamma = 7°$ in order to reduce the the break out dimension and eliminate any splitting jet at hole outlet. The LE SS rear remains as the baseline case and two additional holes were placed at the bottom of the PS Mid row, to diminish the hot areas uncovered in the baseline case. The TE Rear contains edge blended holes as introduced in the previous subsection and 2 fanshaped holes were added at the bottom of the tip of the blade and 1 more at hub, to eliminate the hot spots due to the very thin fillet over the TE, close to this regions.

For the second candidate (Cand. II) LE PS, LE SS front have the same geometrical arrangement as Cand. I. LE SS rear and PS Mid from Cand. I, were replaced with fanshaped angled holes with a laid-back angle $\delta = 5^\circ$. On the TE, the arrangement is the same as Cand. I, but with an increased compound angle for the rear holes of the row, as introduced in the previous subsection.

In Figure 4.31a-c, temperature difference contours for Cand. I are depicted and in Figure 4.31d-f for Cand. II. It could be fairly stated that given the nature of both configurations, a similar behaviour in both FCE and temperature reduction, was expected. Along the entire sensitivity analysis, the biggest improvements in FCE and in terms of metal temperature reduction were achieved by introducing a smooth transition in between cylindrical length and diffusion length for angle fan-shaped holes. Is for this reason that the same type of hole was introduced in the LE SS rear and PS Mid rows, to compare if the results obtained in the LE rows could be replicated in other regions of the blade.

As suspected, both blades show a similar temperature reduction. Both cases achieved peaks of temperature difference relative to the baseline case in around $\sim 100^\circ$ immediately downstream of hole injection at the LE PS and SS front rows. At the bottom of the PS Mid, the cold areas affected by the two new introduced holes reduce their temperature upstream of hole injection. Also, the fan shaped holes introduced at the TE significantly reduced the blade temperature. Unfortunately, the fanshaped hole placed at the bottom of the TE close to the fillet, is not cooling entirely the region of interest, even though metal temperature reduction is being achieved. This is because the fan shape angles are too shallow to spread the coolant in the spanwise direction for the given position. It may be, that by displacing the hole further downwards towards the hub, the entire region could be covered eliminating the entire hot spot produced due to the very thin fillet. No bigger differences can be observed at the LE SS rear row but rather a small hot spot in between holes 6 and 7. From the FCE contours Figure A.7, the assumption on reducing the break-out dimension and a move to a more shallow angle considerably improved both efficiency and metal temperature reduction. But, unfortunately, there still some portion of the flow, spliting close to the upper part of the hole. At the same time, as seen in the results obtanied from inclination angle study, a more shallow angle improved the spanwise spreading of the coolant. The biggest efficiency in the TE was observed for Cand. I, as the increased area is introducing more coolant and enhanced attachment of the jets as the migrate towards the edge of the hole, reducing coolant consumption with the hot gas. In Figure 4.4 a comparison between the total mass flow consumption of each row, is shown.

The effect of introducing smooth transition holes on the PS Mid row and additionally two holes, increased the mass flow rates of the row itself, but also on the LE PS, as the rates are higher in Cand. II compared to Cand. I. This is the reason why a lower mass flow rate is observed on the LE SS rear for Cand. II, despite smooth transition holes were also placed in that row. It seems that a compensation between the rows for the same share channel is leading to a finally increment in the LE PS row. At the same time, this consumption rate on the PS Mid row is leading to a decreased TE mass flow rate.

In Figure 4.33a-b, a comparison between both candidates for PS Mid hole 13 with tangential vector projection orthogonal to the blade surface, is depicted. It can be observed, that for Cand. I (Figure 4.33a), compared to the Cand. II, the structure of the jet is much flatter. This is because for Cand. II more coolant is flowing through the hole and at the same time, the laid-back angle is supporting jet lift off. For Cand. II, the lift off of the right sided portion of the coolant is

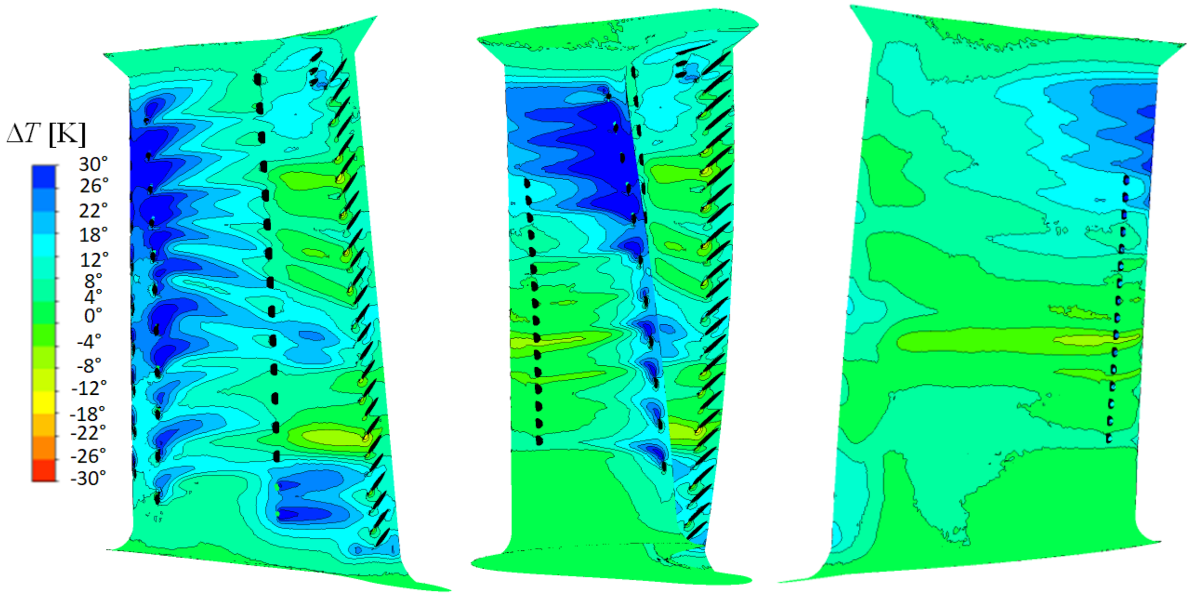

(a) PS view Candidate I (b) SS front view Candidate I (c) SS Rear view candidate I

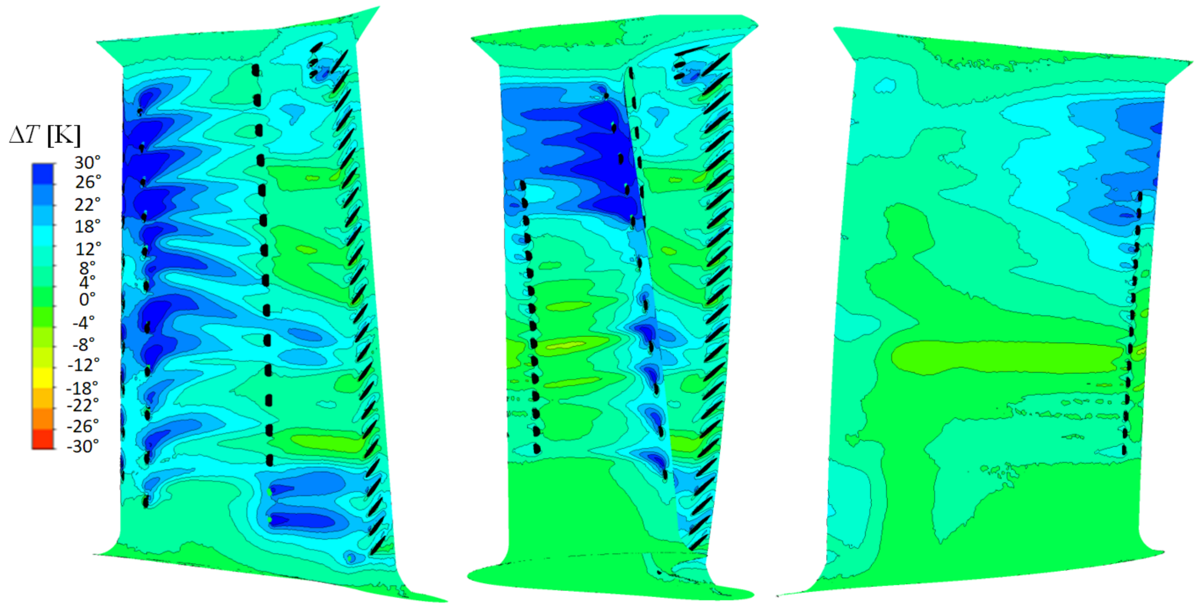

(d) PS view Candidate II (e) SS front view Candidate II (f) SS Rear view candidate II

Figure 4.31: Blade temperature difference comparison between Candidate I and Candidate II

supporting gas entreinment, but not as deep as Cand. I.

It can be concluded that both candidates achieve the desired goal proposed for this thesis. As depicted, a decisive factor could be the mass flow rate consumption, in favour of Cand. I, as mass flow rates are more even in all rows. In terms of blade manufacturing, both models are challenging to build since both contain shallow smooth transition holes and, for Candidate I,

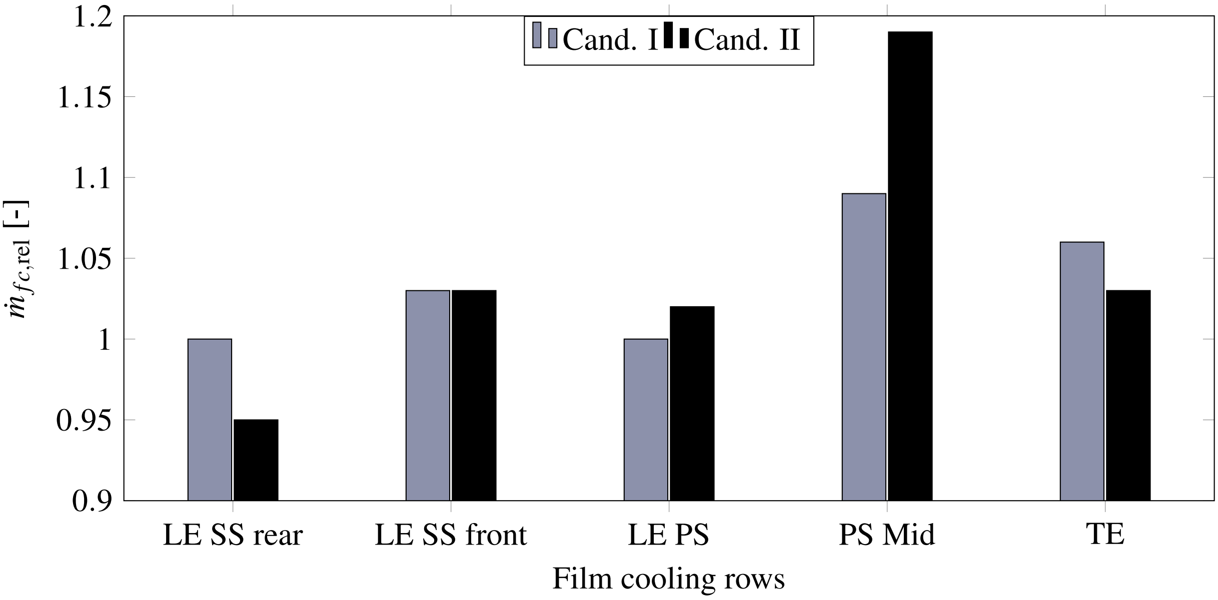

Figure 4.32: Comparison of mass flow split through film cooling rows between Candidate I and Candidate II

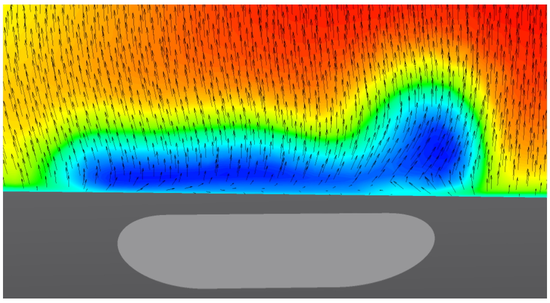

(a) PS Mid Hole 13 - Cand. I

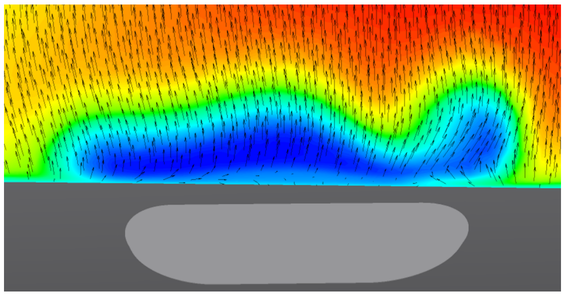

(b) PS Mid Hole 13 - Cand. II

Figure 4.33: Jet structure comparison for PS Mid hole 13 between Candidate I and Candidate II

the TE row with an applied edge blend it is also difficult to achieve.

5 Summary and Outlook

In this section, an overview of the entire work is given. The main conclusions from the sensitivity analysis conducted on a conventional cooling configuration are shared. Afterwards, suggestions for following works will be given.

5.1 Summary of the Work

Due to nowadays requirements, aircraft engines operate a high turbine entry temperatures. This expose the blade to a hostile environment, requiring the use of external and internal cooling. This poses a challenge in the design of optimal cooling configurations. Throughout this work, a sensitivity analysis towards a conventional film cooling configuration, was done. Furthermore, a numerical model was validated showing good overall agreement and notable discrepancies with the experimental conventional cooling concept, due to an incorrect model set-up.

It was shown that the calculations predicted the aerothermal behaviour of the blade. Therefore, a sensitivity analysis was conducted to achieve plausible blade candidates for manufacturing.

An entire description of the baseline case for the film cooling rows captured by the experimental test was discussed. Locating the ribs relatively close to the hole entry improves the film efficiency but only limited for specific holes.

Shifting the hole outlets of cooling holes on the early suction side in downstream direction leads only to benefits if momentum flux ratio decreased enough.

Reducing the inclination angle improves lateral coverage, yielding a good improvement in metal temperature reduction. Manufacturing processes for optimum values can be problematic.

The break-out dimension has a dominating role in the structure of the jets, as the coolant diffuses and emerges to the outer surface. A big break out dimension yields as a result a splitted jet. This structure then describes a two path of jets and a triangular region, with the lowest efficiency values. This dimension is heavily correlated with the fan-shape angle, length to throat, laid back angle and compound angle. Fan-shape holes with big break out dimension have shown this behaviour, increasing also the losses.

Applying a smooth transition in between diffuser and the cylindrical part of the hole, heavily increases film cooling effectiveness and metal temperature reduction. The flow stays attached downstream of the throat and fills most of the diffuser volume. This is leading to an increase in mass flow rates through the holes.

An edge blend on the outer hole of the TE, increased film cooling effectiveness and reduced blade metal temperature. Increasing the inclination angle increases the area covered by the coolant, also reducing good metal temperature.

Increasing the break-out dimension in the PS Mid row, reduces the film cooling effectiveness due to stronger flow detachment. A shallower inclination angle also leads to reduced film cooling effectiveness.

Increasing the spanwise separation of the holes on the suction side rear surface, reduced the effectiveness as the jets separate and expose the metal surface to the hot gas.

Both of the candidates presented in this work considerably reduced blade metal temperature. The effect of fan shape holes with smooth transition increased the mass flow rate affecting the cooling rows upstream of the triple-passage channel. Furthermore, for the case of the leading channel, a different bleeding rate through all 3 rows occurs. Introducing a laid-back angle in the pressure side mid row increases the vertical momentum component, supporting hot gas penetration underneath the jets.

5.2 Outlook

As described in the previous section, deviations between the CFD and the experimental set up are mainly due to the steps and flanges that were excluded in the model. This is of crucial importance, since this flow phenomena and the merge of the channels, define the mass flow split upstream of the core outlets.

Different cascade inlet velocity angles should be conducted in the CFD model in order to achieve a proper alignment of the stagnation line with the blade leading edge. The lowest effectiveness values were found in the early suction side surface since the reduced external velocity won't deflect the jets toward the surface, thus consuming the coolant into the hot gas.

Together with the before mentioned conclusions derived from the sensitivity analysis, geometrical modifications should be conducted to extend the potential of conventional cooling. The method utilized throughout this work provided good understanding for the local implications of the modified variables. But, in order to generate an improved overview, not only several cases for each variable should be introduced but rather focus on the major implications one variable has on the entire geometry. This was not the case for this work and many of the general influences of a single parameter correlated to the entire geometry, remain unknown. Introducing more physical or geometrical variables under study could be misleading, since the amount of data not only increases but also strong correlation between each variable is most likely to happen.

Some of the vastly studied geometrical parameters, were left aside throughout this work. These parameters, together with the sensitivity analysis conducted in this work, should be analysed to reach a better overview of the hole set up. Some of these variables are streamwise angle, cross flow condition, shape and size of rib turbulators, slots or branched holes. Furthermore, these parameters should not be only analysed from an isolated overview, but then rather combined different set ups and discuss the final results.

Bibliography

Aga, V. (2011): *Influence of flow structure on compound angled film cooling effectiveness and heat transfer*. ASME Journal of Turbomachinery, vol. 133, pp. 031029.

Ahn, J., Jung, I. S. and Lee, J. S. (2003): *Film cooling from two rows of holes with opposite orientation angles: injectant behavior and adiabatic film cooling effectiveness*. International Journal of Heat and Fluid Flow, vol. 24, pp. 91–99.

Alizadeh, M., Izadi, A. and Fathi, A. (2014): *Sensitivity Analysis on Turbine Blade Temperature Distribution Using Conjugate Heat Transfer Simulation*. ASME Journal of Turbomachinery, vol. 136, pp. 13.

Aunapu, N.V., Volino, R.J., Flack, K. and Stoddard, R.M. (2000): *Secondary flow measurements in a turbine passage with endawll flow modification*. Journal of turbomachinery, vol. 122, pp. 651–658.

Baldauf, S. and Scheurlen, M. (1996): *CFD based sensitivity study of flow parameters for engine like film cooling conditions*. ASME 1996 International Gas Turbine and Aeroengine Congress and Exhibition, p. V004T09A037–V004T09A037. American Society of Mechanical Engineers.

Baldauf, S., Schulz, A. and Wittig, S. (2001): *High resolution measurements of local effectiveness from discrete hole film cooling*. ASME Journal of Turbomachinery, vol. 113, pp. 758–765.

Bashir, M. H., Shiau, C.-C. and Han, J.-C. (2017): *Film cooling effectiveness for three-row compound angle hole design on flat plate using PSP technique*. International Journal of Heat and Mass Transfer, vol. 115, pp. 918–929.

Bernardini, M., Larsson, J., Pirozzoli, S. and Grasso, F. (2016): *Heat transfer and wall temperature effects in shock wave turbulent boundary layer interactions*. Universita di Roma ‘La Sapienza’ - Dept. of Mechanical Engineering.

Bräunling, Willy J.G. (2015): *Flugzeugtriebwerke Grundlagen, Aero-Thermodynamik, ideale und reale Kreisprozesse, Thermische Turbomaschinen, Komponenten, Emissionen und Systeme*. Springer Verlag, Berlin. ISBN 978-3-642-34539-5.

Bunker, S. R. (2005): *A Review of Shaped Hole Turbine Film Cooling Technology*. Journal of Heat Transfer, vol. 127, pp. 441–453.

CentaurSoft (2022): *CentaurSoft User’s Manual v14.5*. CentaurSoft Documentation.

Dückershoff, R., Rabe, G., Prinzler, M. and Berg, H.P. (2017): *Filmkühlung bei verzögerter Hauptströmung*. Deutscher Luft- und Raumfahrtkongress 2000, vol. 3. ISSN 0070-4083.

Ekkad, S. V., Zapata, D. and Han, J. C. (1997): *Film effectiveness over a flat surface with air and CO2 injection through compound angle holes using a transient liquid crystal image method*. Journal of Turbomachinery, vol. 119, pp. 587–593.

Elfner, M., Schulz, A., Bauer, H.-J. and Lehmann, K. (2019): *A Novel Test Rig for Assessing Advanced Rotor Blade Cooling Concepts, Measurement Technique and First Results Extinction Technique in Optically Accessed Research Engines*. ASME Turbo Expo 2017: Turbomachinery Technical Conference and Exposition, vol. 30, pp. V05AT16A015–V05AT16A015.

Gao, Z., P.Narzay, D. and Han, Je-Chin (1997): *Film cooling on a gas turbine blade pressure side or suction side with axial shaped holes*. ASME Journal of Turbomachinery, vol. 119, pp. 587–593.

Goldstein, R. J. and Eriksen, V. L. (1974): *Heat transfer and film cooling following injection through inclined circular holes*. ASME Journal of Heat Transfer, vol. 96, pp. p.239–245.

Goldstein, R. J. and Spores, R. A. (1988): *Turbulent Transport on the Endwall in the Region Between Adjacent Turbine Blades*. Journal of Heat Transfer, vol. 110, pp. 862–866.

Goldstein, R. J., Irvine, T. F. and Harntett, J. P. (1971): *Film Cooling*. Elsevier, vol. 7, pp. 321–379. ISSN 0065-2717.

Goldstein, R. J., Wang, H. P. and Jabbari, M. (1994): *The Influence of Secondary Flows Near the Endwall and Boundary Layer Disturbance on Convective Transport From a Turbine Blade*. ASME 1994 International Gas Turbine and Aeroengine Congress and Exposition. DOI:10.1115/94-GT-165.

Han, Je-Chin (2004): *Recent Studies in Turbine Blade Cooling*. International Journal of Rotating Machinery, vol. 10, pp. p. 443–457. ISSN 1064–2285.

Han, Je-Chin, Dutta, Sandip and Ekkad, Srinath (2013): *Gas Turbine Heat Transfer and Cooling Technology*. CRC Press, Boca Raton. ISBN 978-1-4665-6490-9.

Hawthorne (1955): *The growth of secondary circulation in frictionless flow*. Mathematical Proceedings of the Cambridge Philosophical Society, vol. 51, pp. 737–743.

Huoxing, L. (2012): *Experimental study on agressive inter-turbine duct with strut fairings*. Beijing: Beihang University.

Klein, A. (1966): *Untersuchungen über den Einfluß der Zuströmgrenzschicht auf die Sekundärströmungen in den Beschaufelungen von Axialturbinen*. Forschung im Ingenieurwesen A, vol. 32, pp. 175–178.

Krishnaswamy, K. and Salyan, S. (1994): *External and Internal Cooling Techniques in a Gas Turbine Blade - An Overview*. International Journal of Engineering Research and Technology (IJERT). ISSN 2278-0181.

Ligrani, P. M. and Lee, J . S. (1996): *Film cooling from a single row of compound angle holes at high blowing ratios*. International Journal of Turbomachinery, vol. 2, pp. 259–267.

Martinez-Bota, R. and Yuen, C. H. N. (2005): *Film cooling characteristics of rows of round holes at various streamwise angles in a crossflow: Part I. effectiveness*. International Journey of Heat and Mass Transfer, vol. 48, pp. 4995 – 5016.

Moon, Young J. and Koh, Sung-Ryong (2000): *Counter-rotating streamwise vortex formation in a turbine cascade with endwall fence*. Computers and Fluids, vol. 30, pp. 473–490.

Sharma and Butler (1987): *Predictions of Endwall Losses and Secondary Flows in Axial Flow Turbine Cascades*. ASME Turbo Expo 2017: Turbomachinery Technical Conference and Exposition, vol. 109, pp. 229–236.

Siw, Sin Chien (2007): *Eexperimental Investigation of Internal Cooling Passages of Gas Turbine Blade With Pin-Fins and Rib-Turbulators*. Dissertation, University of Pittsburgh.

Stichling, Katharina (2018): *Simulation and Analysis of the Conjugate Heat Transfer in a Rotor Blade and Comparison with Experimental Data*. Master thesis, Karlsruhe Institut für Technologie.

Wang, H. P., Olson, S. J., Goldstein, R. and Eckert, E. R. G (1997): *Flow Visualization in a Linear Turbine Cascade of High Performance Turbine Blades*. Journal of Turbomachinery, vol. 119.

Zou, Z., Liu, S. Wang H. and Zhang, W. (2018): *Axial Turbine Aerodynamics for Aeroengines, Flow Analysis and Aerodynamics Design*. Springer, China. ISBN 978-981-10-5750-2.

Öngören, A. (1981): *Heat transfer on the endwall of a turbine cascade with film cooling*. Project Report, Von Karman Institure for Fluid Dynamics, vol. 19.

Appendix

A.1 Appendix 1

Table A.1: Geometrical parameters of LE PS and SS rows

Type	L [mm]	D [mm]	L/D [-]	$\alpha[°]$
Cylindrical	8.86	1.2	7.4	30

A.2 Appendix 2

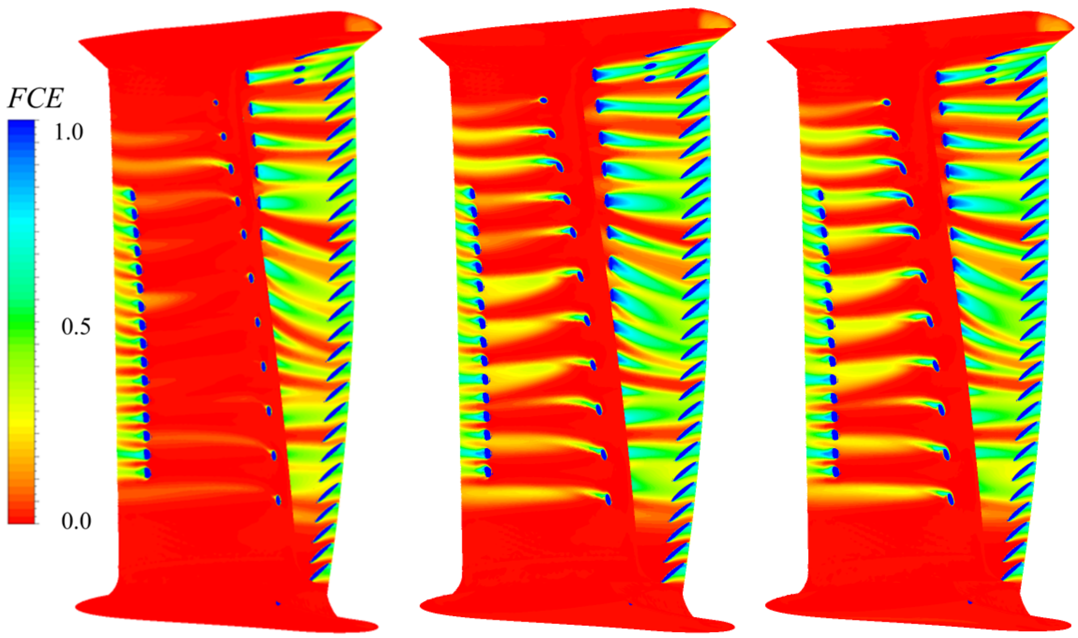

(a) CASE I (b) CASE II (c) CASE III

Figure A.1: FCE comparison for outlet hole position study on LE SS front row

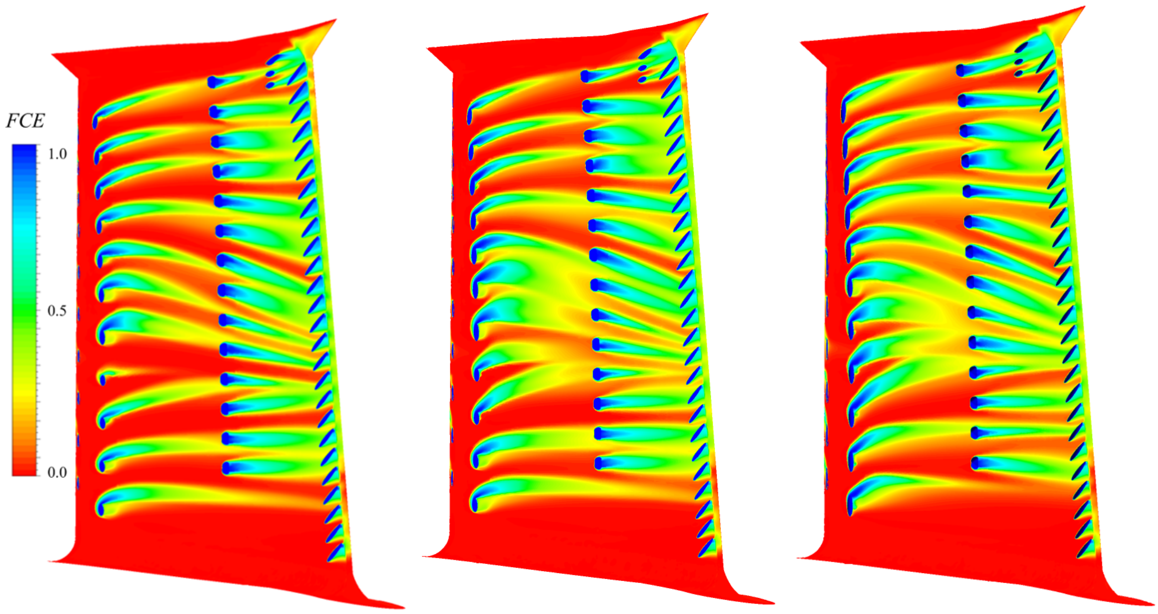

(a) CASE I (b) CASE II (c) CASE III

Figure A.2: FCE comparison between inclination angle variations on LE PS row

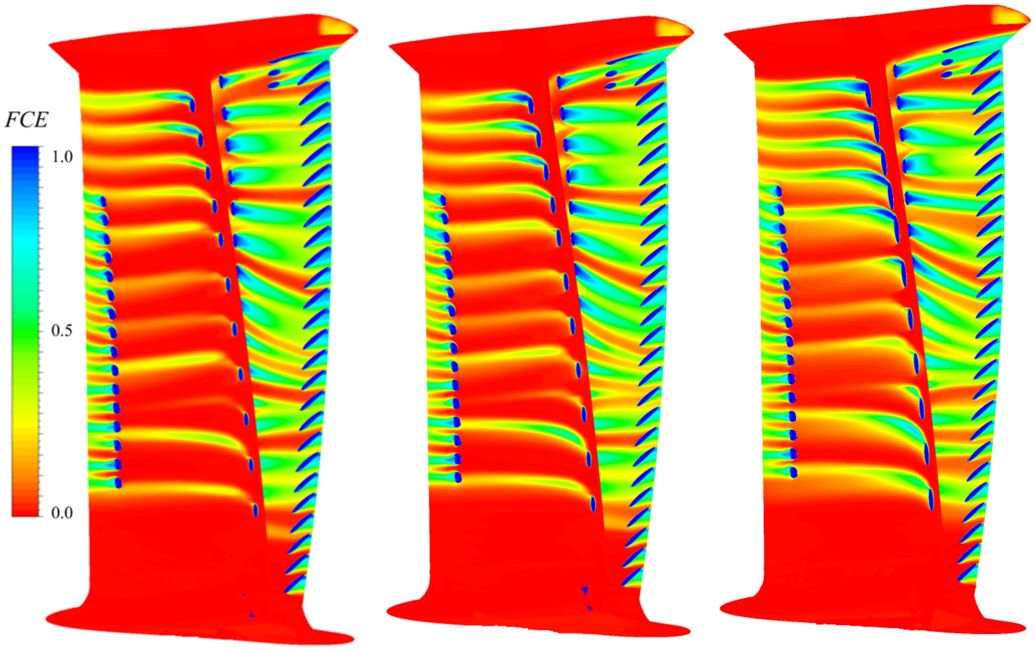

(a) CASE I (b) CASE II (c) CASE III

Figure A.3: FCE comparison between inclination angle variations on LE SS row

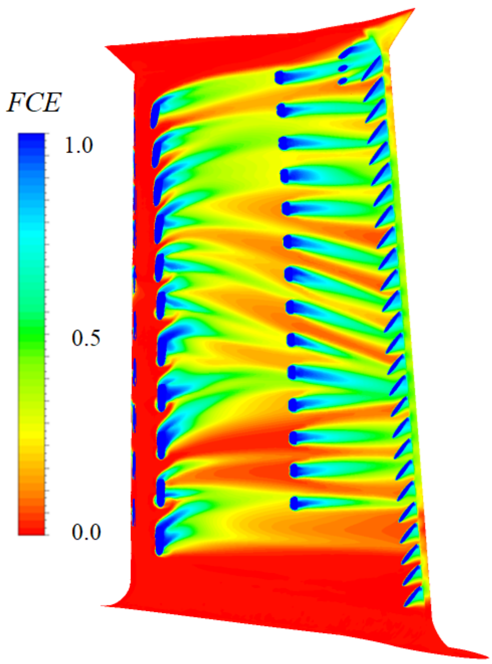

(a) FCE PS view

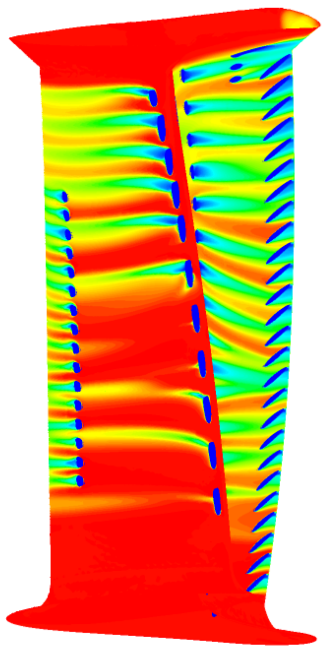

(b) FCE SS front view

Figure A.4: FCE plots of LE PS and SS rows with smooth transition holes

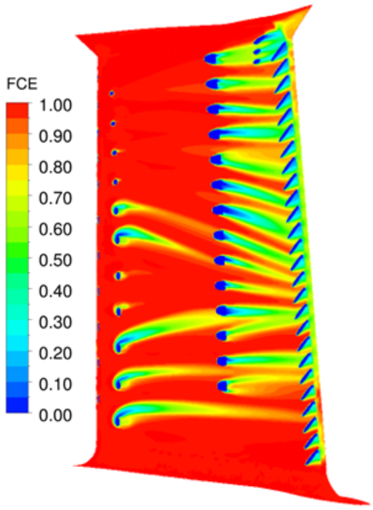

(a) Increased Radial Angle

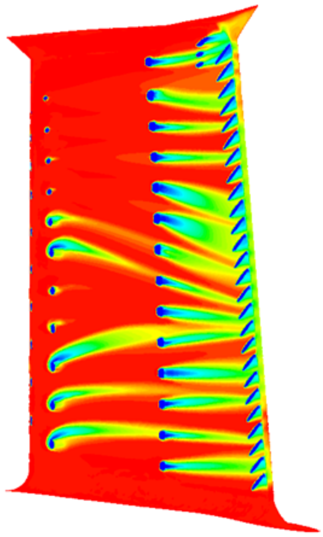

(b) Increased Spanwise Separation

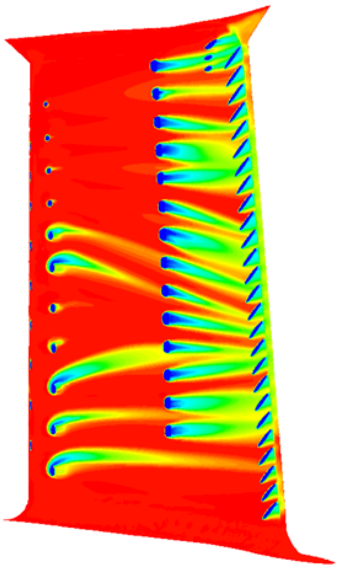

(c) Increased Fan-shape

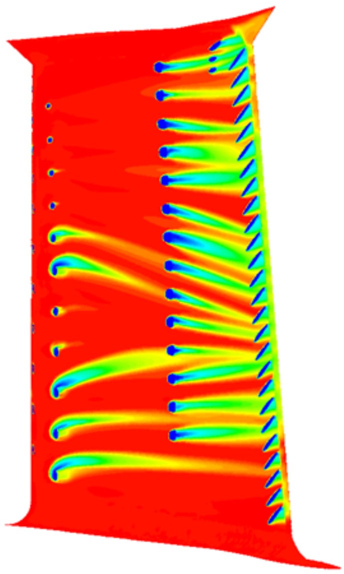

(d) Increased Laid-back angle

Figure A.5: FCE comparison between PS Mid row geometries

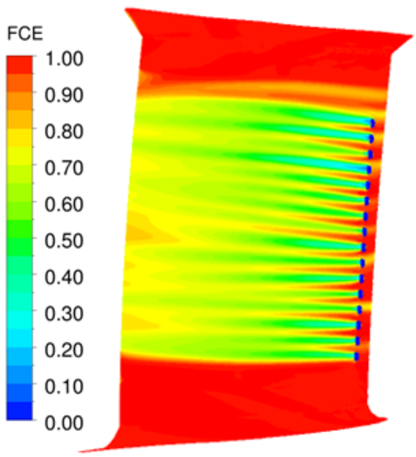

(a) SS Rear Spanwise I

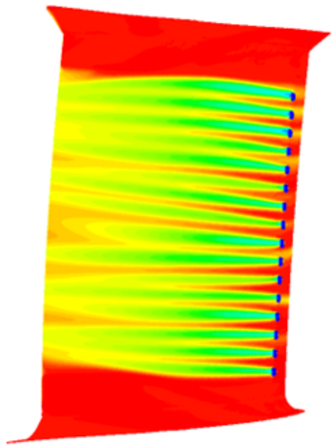

(b) SS Rear Spanwise II

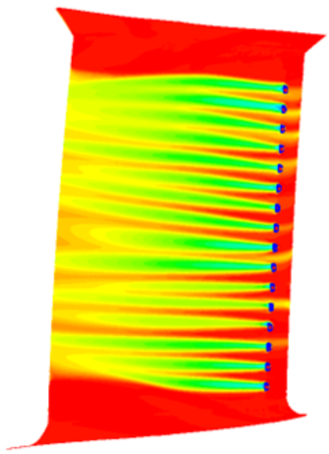

(c) SS Rear Spanwise III

Figure A.6: FCE plots of LE SS Rear Spanwise separation study

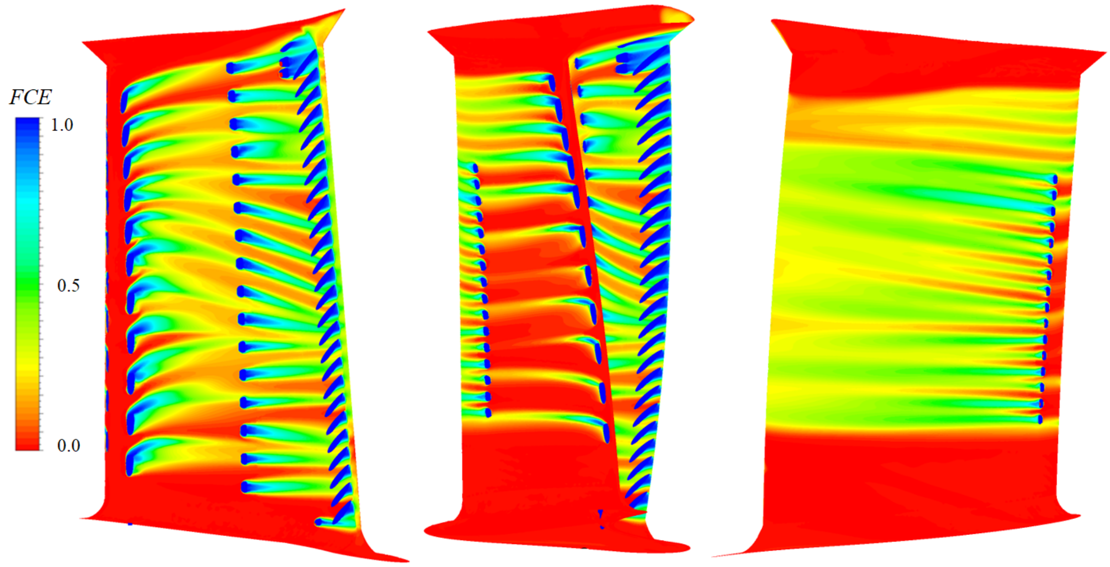

(a) PS view Candidate I (b) SS front view Candidate I (c) SS Rear view candidate I

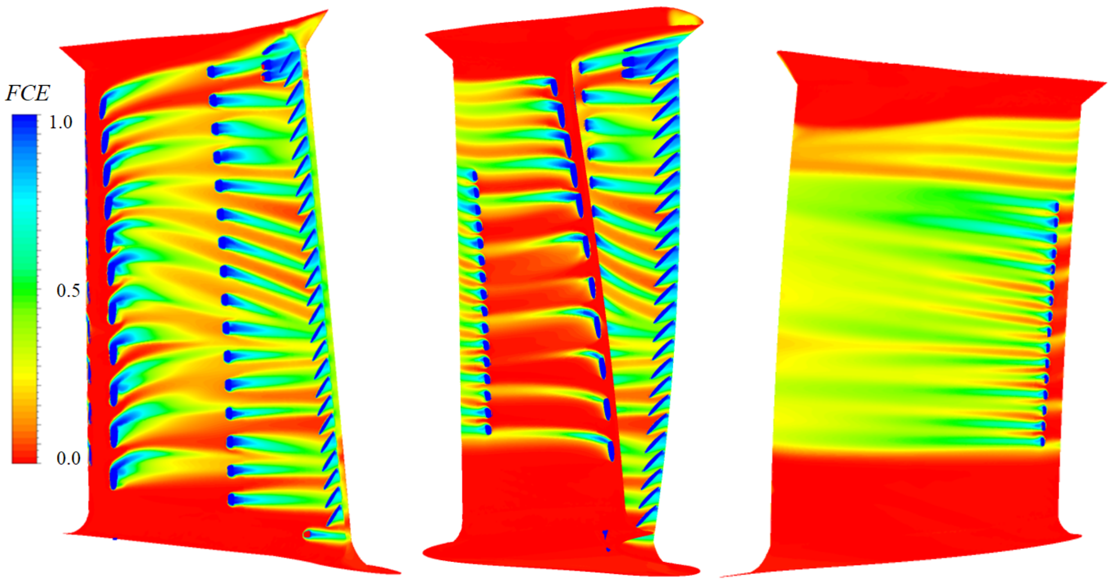

(d) PS view Candidate II (e) SS front view Candidate II (f) SS Rear view candidate II

Figure A.7: FCE comparison between Candidate I and Candidate II

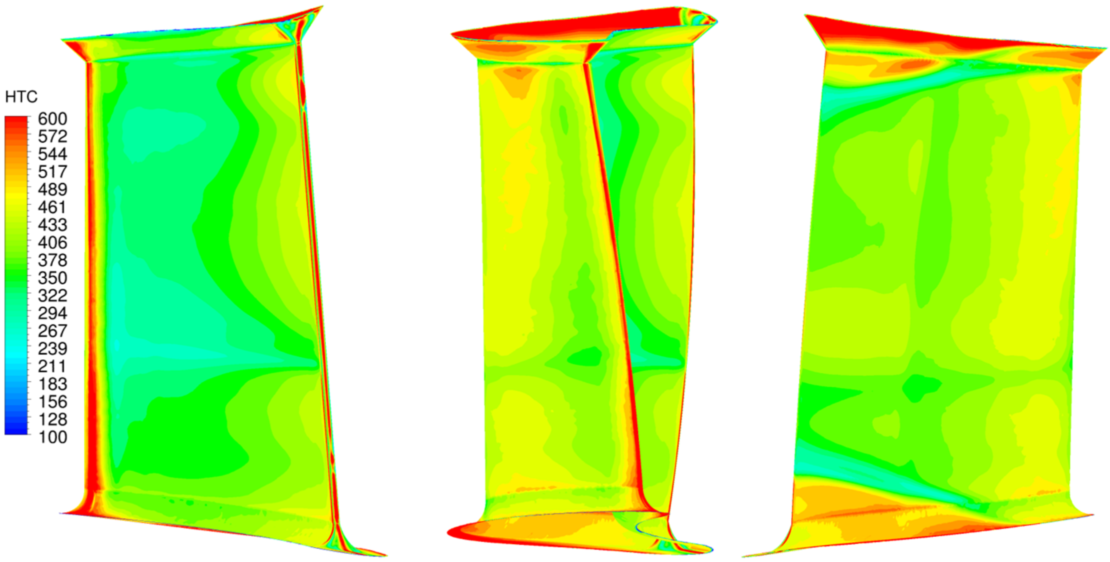

(a) PS view (b) SS front view (c) SS Rear view

Figure A.8: HTC overview for uncooled blade

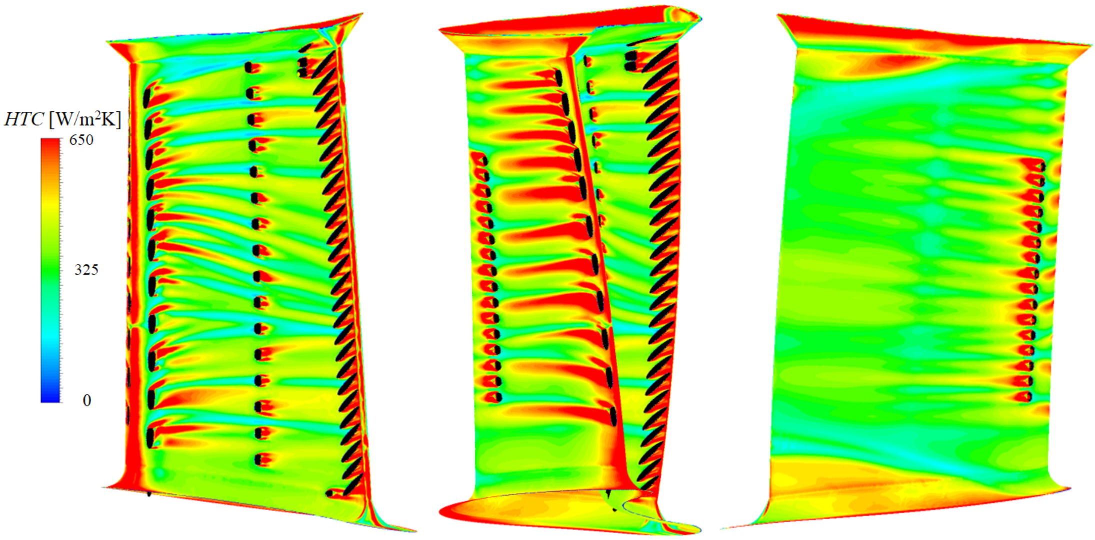

(a) PS view Candidate I (b) SS front view Candidate I (c) SS Rear view candidate I

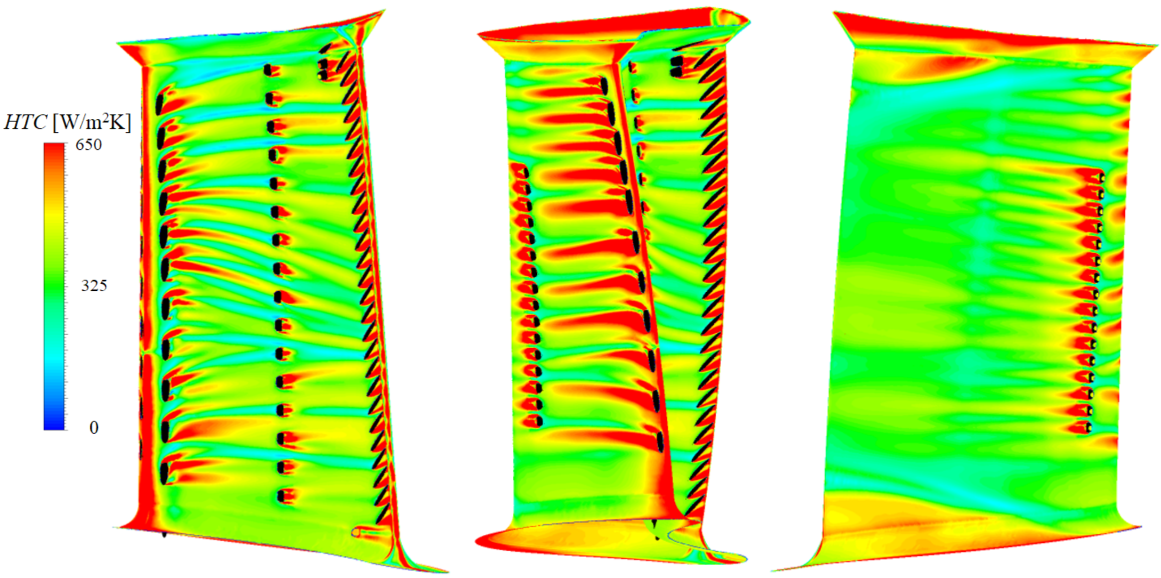

(d) PS view Candidate II (e) SS front view Candidate II (f) SS Rear view candidate II

Figure A.9: HTC comparison between Candidate I and Candidate II